UNIVERSIDAD DE GRANADA

PROGRAMA DE DOCTORADO EN FÍSICA Y CIENCIAS DEL ESPACIO

TESIS DOCTORAL:

ESTUDIO DEL RUIDO Y ANÁLISIS DE LA INCERTIDUMBRE EN DOSIMETRÍA CON PELÍCULA RADIOCRÓMICA

Juan Antonio Vera Sánchez

Granada 2018

Editor: Universidad de Granada. Tesis Doctorales
Autor: Juan Antonio Vera Sánchez
ISBN: 978-84-9163-853-7
URI: http://hdl.handle.net/10481/51161

Dedicado a mi mujer,
por tantas cosas que aquí no caben;
y a mi madre y a mi hermana,
por estar ahí cuando no queda nadie

El doctorando, Juan Antonio Vera Sánchez, autor de la presente tesis doctoral, titulada "*Estudio del ruido y análisis de la incertidumbre en dosimetría con película radiocrómica*", y el director de la misma, Antonio González López, garantizamos, que el trabajo ha sido realizado por el doctorando bajo la dirección del director de tesis y hasta donde nuestro conocimiento alcanza, en la realización del trabajo, se han respetado los derechos de otros autores a ser citados, cuando se han utilizado sus resultados o publicaciones.

Granada, a 1 de abril de 2018.

El director de la tesis	El doctorando
Fdo. Antonio González López	Fdo. Juan Antonio Vera Sánchez

Agradecimientos

Esta tesis doctoral no hubiera sido posible sin el apoyo del director Antonio González, el cual tiene la virtud (rara en estos días) de aparecer cuando sólo se vislumbra oscuridad y estar donde hay que estar. Por eso aparecerá alguna vez más también en esta página.

Me gustaría empezar por agradecer a todos los que coincidimos en unos años de crisis y problemas en un hospital dedicado a una antigua patrona, y, pese a todo eso y más, fuimos personas y cuajamos una sana amistad: Carmen, Antonio y Pedro, y Ros y Jorge. Y a Mariaje, que con bastante asiduidad nos soporta a tres de este grupo.

No podría olvidarme de mis compañeros de Reus: Manel, Pilar, Enric, Manu, Jesús y Natalia que me hacen la vida muy fácil desde hace casi cinco años y me acogieron muy bien, incluidos Maru y Miguel, que ya no están en Reus y se les echa de menos. Josep y Albert llegaron más tarde, pero también me ayudan mucho. Especial agradecimientos merecen Víctor, Rubén y Katrine que me soportan a la hora del café, cuando no me soporto ni yo. Y a Víctor tengo que agradecerle que me picara con el tema del TG, que tantas alegrías nos ha dado (ya no me acuerdo del trabajo), y tantos buenos consejos sobre investigación.

No podría dejar fuera de esta mención a amigos que se preocupan de las cosas importantes de la vida y me llaman para tomar algo y hablar de precisamente eso, la vida. Juan Pedro y Paquita, son amigos de esos y Pilar ¡es una niña guapísima!. Bruno y Mar, Jesús y Elena, y Manolo también son amigos de esos. Y este documento me ha robado muchas horas y ratos de ellos, espero que sepan perdonarme.

Y no podría terminar sin agradecer a mi mujer toda su ayuda, además, mientras escribo estas líneas, ella revisa el documento. A mi hermana que me llama y me dice que quiere felicitarme cuando termine esto. Y a mi madre, ya que sin ella ni yo estaría aquí ni este documento se imprimiría. Mis suegros y mi cuñada también merecen una mención, no sólo me tratan genial en Jaén, sino que, además, me dan ánimos con este y otros proyectos.

Índice general

Resumen

La película radiocrómica es un dosímetro de uso común en los departamentos y servicios de Física Médica de todo el mundo, que se emplea para, entre otras aplicaciones, la medida distribuciones de dosis absorbida bidimensionales con una alta resolución espacial y la estimación de dosis en condiciones fuera de referencia donde la elección de un dosímetro fiable no es una tarea simple.

La exposición de la película radiocrómica a la radiación ionizante tiene como consecuencia su oscurecimiento debido a la polimerización de las fibras que componen el material de la capa activa. Este oscurecimiento es dependiente de la dosis absorbida y permite emplear la película radiocrómica para la medida de dicha dosis.

La dosimetría con película radiocrómica se realiza empleando un dispositivo de lectura que permite obtener una imagen digital de la película irradiada y cuantificar la transmisión de la luz a través de la misma. Los dispositivos más ampliamente usados y aceptados en el campo de la Física Médica son los escáneres de color de sobremesa que, debido a su poco impacto económico y a su versatilidad, constituyen una solución robusta y eficaz para el propósito de la dosimetría con película radiocrómica.

La manipulación de la película radiocrómica se debe realizar tomando una serie de precauciones que incluyen, entre otras, el correcto almacenaje de las películas para evitar el impacto de las condiciones ambientales, el uso de guantes para evitar impresionar huellas dactilares en las películas y el control del intervalo de tiempo transcurrido entre la irradiación de la película y su lectura para evitar inexactitudes en la estimación de la dosis.

Antes del uso de la película radiocrómica como dosímetro, se debe realizar una calibración del lote de películas para obtener las curvas sensitométricas que relacionan las lecturas de la película con las dosis de irradiación. Posteriormente, la dosimetría con película radiocrómica es un proceso que

involucra tres pasos: la irradiación de la película; su lectura, que da como resultado una matriz de datos que puede visualizarse como una imagen digital, y la conversión a dosis de los valores leídos en la película, para la que se emplean las curvas de calibración del lote y alguno de los varios algoritmos de conversión en uso. Estos algoritmos se dividen fundamentalmente en dos tipos: los que emplean solo uno de los canales de color del escáner (algoritmos monocanal), y los que combinan la respuesta de dos o tres de estos canales para el cálculo de la dosis (algoritmos multicanal).

Esta tesis doctoral, presentada bajo el formato de compendio de publicaciones, se ha dedicado al estudio y descripción de las fuentes de ruido presentes en la dosimetría con película radiocrómica, así como, al análisis y cálculo con técnicas Monte-Carlo de la incertidumbre presente en este tipo de dosimetría.

En las investigaciones llevadas a cabo, como es habitual en este campo, se parte del análisis de las respuestas leídas en escáneres digitales de películas radiocrómicas irradiadas. Por otro lado, se propone y prueba la validez de nuevos métodos matemáticos y enfoques que, hasta donde nuestro conocimiento alcanza, no han sido previamente aplicados en este campo, como son la descomposición multirresolución mediante procesado wavelet, el análisis de incertidumbre mediante métodos Monte-Carlo y la aplicación de la metodología para medida del ruido descrita en la norma ISO-15739.

Además, durante el desarrollo de esta tesis se ha hecho especial hincapié en las aplicaciones prácticas de la dosimetría con película radiocrómica. Así pues, se proponen mejoras en las verificaciones de los planes de tratamiento de Oncología Radioterápica y se presentan nuevas pruebas destinadas al comisionamiento y medida de las características dosimétricas de los colimadores multiláminas de los aceleradores lineales.

El primer capítulo de esta tesis está dedicado a la dosimetría con película radiocrómica y sus fundamentos. En la introducción se describen las características y ventajas de esta película como dosímetro, así como sus múltiples ámbitos de aplicación en el campo de la Física Médica y otras particularidades de índole práctico que deben tenerse en cuenta a la hora de su empleo como dosímetro. A continuación, se hace un repaso de los fundamentos de dosimetría con película radiocrómica, incidiendo en los procesos físicos que gobiernan e influyen en su oscurecimiento y su lectura con el escáner; describiendo la metodología general seguida para la lectura, manipulación, irradiación y calibración, y, finalmente, detallando los algortimos comúnmente empleados para la conversión de la imagen digital leída a mapa de dosis. Por

último, se detallan los objetivos de esta tesis doctoral.

El análisis de la incertidumbre se lleva a cabo en su mayor parte en los dos siguientes capítulos. En particular, en el segundo capítulo se presentan las investigaciones sobre la caracterización estadística de las respuestas leídas con escáneres digitales de películas radiocrómicas irradiadas y el efecto de esta caracterización en la simplificación de los algoritmos multicanal. Posteriormente, en el tercer capítulo se presenta un nuevo modelo multi-etapa para el cálculo Monte-Carlo de incertidumbres en dosimetría con película radiocrómica con algoritmos mono y multicanal. Este nuevo enfoque de cálculo de incertidumbres hace uso extensivo de la caracterización estadística del capítulo anterior, es más, las dependencias estadísticas entre las diferentes respuestas de los canales de lectura explican algunos de los resultados más importantes del análisis de incertidumbre.

El estudio del ruido se lleva a cabo principalmente en los capítulos cuarto y quinto. En concreto, en el capítulo cuarto se presentan las fuentes del ruido en dosimetría con película radiocrómica y se estudia la propagación del ruido presente en la imagen digital a los mapas de dosis a través del uso de diferentes tipos de algoritmos. Además, se muestra la influencia de este ruido en la incertidumbre de las estimaciones dosimétricas. En el capítulo quinto se muestra una aplicación de la mitigación del ruido temporal del digitalizador a la dosimetría con película radiocrómica y su impacto en la verificación de planes de tratamiento.

En el sexto capítulo se emplea la película radiocrómica para la caracterización dosimétrica de los colimadores multilámina y micro-multilámina. Así pues, se describen pruebas para medir y comisionar el efecto *tongue and groove* tanto con película radiocrómica como con cámara de ionización. Además, gracias a la alta resolución de la película radiocrómica y a los resultados de los capítulos previos sobre el ruido en la dosimetría con película radiocrómica, se diseñaron pruebas que permitieron apreciar detalles milimétricos de la deposición de dosis espacial.

Finalmente, en el séptimo capítulo se muestran las conclusiones de las investigaciones realizadas y se detallan las nuevas investigaciones en curso relacionadas con las líneas de investigación de esta tesis doctoral.

Capítulo 1

La dosimetría con película radiocrómica

1.1. Introducción

La película radiocrómica es un dosímetro usado para la medida de la radiación ionizante en diversos ámbitos de la industria y la sanidad [1, 2]. Tal y como se detalla en los trabajos de Devic [3] y Devic y col. [4], la película radiocrómica presenta características notables para su uso en la práctica clínica, tales como la equivalencia a agua, independencia de la respuesta con la tasa de dosis y débil dependencia con el espectro de la radiación. Además, proporciona mapas de dosis bidimensionales con una alta resolución espacial. Todas estas características la convierten en uno de los dosímetros más adecuados para la dosimetría de la radiación en condiciones fuera de referencia. Otras características de la película radiocrómica, que favorecen su implantación y extensión como dosímetro, son su insensibilidad a la luz natural, su facilidad de manejo, la posibilidad de ser dividida en varios trozos que pueden sumergirse en agua y su facilidad de lectura, que puede llevarse a cabo con un escáner de sobremesa.

En el campo de la Física Médica, la película radiocrómica se usa en multitud de aplicaciones, algunas de las cuales son difíciles de llevar a cabo por las condiciones en las que se deben realizar: pérdida de equilibrio electrónico, importantes variaciones en el espectro energético de los haces, tasas de dosis muy elevadas o muy bajas, altos gradientes de dosis, etc. Así por ejemplo, se ha demostrado la utilidad de la película radiocrómica en la caracterización y verificación de los campos pequeños [5, 6] suministrados por los aceleradores lineales, frente a otros detectores limitados por el efecto volumen [7, 8]. También se utiliza en la verificación de tratamientos con campos pequeños y/o alta modulación, como son los planes de radiocirugía [9] y radioterapia esteretáctica corporal con arcoterapia volumétrica modulada [10]. Incluso, se utiliza en el comisionamiento de la arcoterapia volumétrica modulada [11] y en la verificación pre-tratamiento de planes de intensidad modulada y arcoterapia volumétrica modulada [12]. La medida de distribuciones de dosis en braquiterapia es otra de las aplicaciones recomendadas de la película radiocrómica, tal y como describen Khan y Gibbons [13], y Palmer y col. [14]. Además, se ha estudiado su viabilidad para la verificación de distribuciones de dosis de aplicadores oftálmicos, como se detalla en el trabajo de Hermida-López y Brualla [15]. Gracias a su poca atenuación y a su débil dependencia del espectro de la radiación, las medidas de dosis recibida en piel durante los tratamientos de radioterapia se pueden llevar a cabo también con película radiocrómica, como se describe en los trabajos de Devic y col. [16], Palmer y col. [17], y Bufacchi y col. [18]. Más allá de la verificación de tratamientos y medidas *in vivo*, se ha propuesto el uso de este dosímetro para la mejora de

las medidas de penumbra de los haces de aceleradores clínicos [19] y para la realización de medidas dosimétricas en presencia de materiales de alta densidad [20]. En el área de la Radiología, también se ha empleado la película en dosimetría de tomógrafos dentales [21] y en la medida de dosis de entrada en cardiología intervencionista [22], entre otros usos.

Comercialmente, se pueden encontrar diversos modelos de películas radiocrómicas de la marca Gafchromic^{TM}. Estos modelos se diferencian en el ámbito de aplicación, el rango de dosis de exposición recomendada y en el espectro de la radiación ionizante recomendada para su irradiación. En el campo de la Radiología, se encuentran los modelos XR-CT2, XR-M2 y XR-QA, recomendados para la medida del espesor de corte en los tomógrafos de radiodiagnóstico, el control de calidad de los mamógrafos y el control de calidad de los equipos de radiología digital respectivamente; así como el modelo XR-RV3, recomendado para las medidas de dosis de entrada en procedimientos de radiología intervencionista guiados con fluoroscopia. Por otro lado, en el ámbito de la Radioterapia, el modelo RT-QA2 se emplea para el control de calidad de los aceleradores, con un rango de dosis recomendado que va desde los 0,02 hasta los $8Gy$, mientras que los modelos de película EBT3, EBT-XD, MD-V3 y HD-V2 están destinados a la dosimetría física y presentan rangos de dosis de exposición recomendados que van desde los 0,1 a $10Gy$ del primer modelo, hasta un rango de 10 a $1000Gy$ del último modelo. El modelo de películas EBT3, con el que se desarrolla la presente tesis doctoral, es el más ampliamente usado en la actualidad para dosimetría en el ámbito de la Radioterapia. Además, se pueden encontrar en diversas presentaciones con diferentes tamaños, diferentes marcas de orientación o diferentes formas para encajar en maniquíes específicos destinados al control de calidad y la dosimetría. En la figura 1.1 se muestra la presentación de una caja de películas EBT3 y el aspecto visual de una película de este modelo.

La exposición de la película radiocrómica a la radiación ionizante tiene como consecuencia su ennegrecimiento. Además, este oscurecimiento es dependiente de la dosis recibida en cada punto, proporcionando de esta manera una representación espacial de la deposición de dosis en la propia película que puede convertirse a mapa de dosis. Para ello, además de la película radiocrómica, para completar el equipo dosimétrico, se necesita un dispositivo capaz de medir el cambio de sus propiedades ópticas. Así pues, la práctica habitual en este tipo de dosimetría es el empleo de escáneres de sobremesa, como se describe en los trabajos de Ferreira y col. [23], Devic y col. [24], Devic y col. [25], y Lynch y col. [26]. De esta manera, el conjunto película-escáner constituye un sistema dosimétrico económico, simple, fácil de usar,

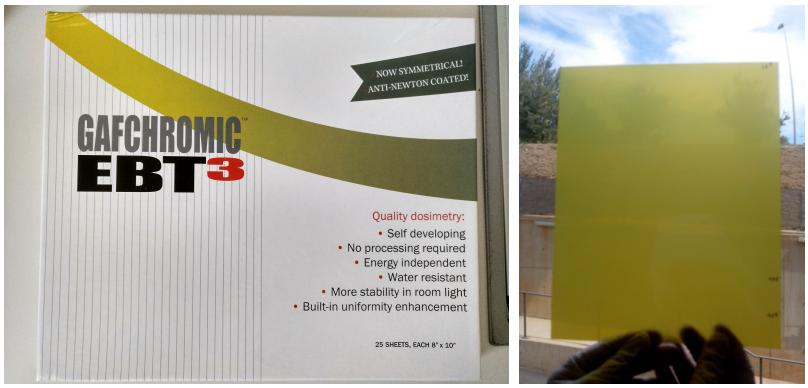

(a) Caja de EBT3 (b) Una película EBT3

***Figura* 1.1:** Las películas Gafchromic^{TM} EBT3.

robusto, versátil y capaz de proporcionar estimaciones dosimétricas en una amplia gama de situaciones de la Física Médica.

Para obtener valores de dosis absoluta a partir de los cambios en las propiedades ópticas de la película radiocrómica, se debe realizar una calibración del lote de películas recibidas. En este sentido, el ennegrecimiento de la película radiocrómica leído en un escáner no se puede relacionar directamente con la dosis absorbida por la película a través de un factor de calibración obtenido de un certificado, debido a diversos factores como la variabilidad del espectro luminoso de las lámparas de los escáneres de sobremesa y las diferencias que se pueden encontrar en la composición y espesor del material activo de diferentes lotes [3]. Por tanto, cada vez que se recibe una caja de películas, se realiza la calibración del lote en el mismo escáner que se va a emplear para la lectura del resto de películas de la caja y, preferiblemente, en un haz de calidad similar al que se va a emplear. Esta calibración suele realizarse exponiendo trozos de una misma película a dosis conocidas, posteriormente, estos trozos son leídos en el escáner y, finalmente, las respuestas leídas en los trozos de película junto con las dosis de exposición de los trozos se utilizan para el ajuste de una función o relación matemática que se usará como función de calibración, también conocida como curva sensitométrica.

Una vez calibrado el lote de películas radiocrómicas, se pueden emplear el resto de películas del lote para medir distribuciones dosimétricas desconocidas. El análisis de cada una de las películas, en general, está compuesto de tres pasos: la exposición de la película a la distribución de dosis desconocida, la lectura de la película en el escáner y la conversión a dosis de la imagen digital obtenida con el escáner. En este paso, el algoritmo escogido empleará las

curvas de calibración del lote para la obtención del mapa de dosis. Además, si la película ha sido expuesta a una distribución bidimensional de dosis que se quiere verificar, por ejemplo un plan de tratamiento, se añadirá un paso adicional, que se ocupa de la comparación de la distribución planificada y la medida con película. En la figura 1.2 se muestra la obtención de un mapa de dosis de un plan de tratamiento de cáncer de pulmón a partir de la irradiación de un trozo de película en un maniquí de material equivalente a agua, con un tamaño similar a un paciente promedio.

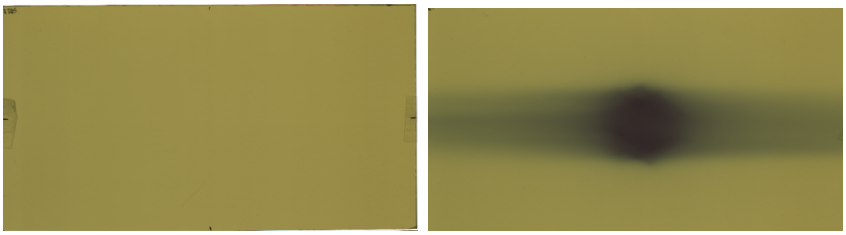

(a) (b)

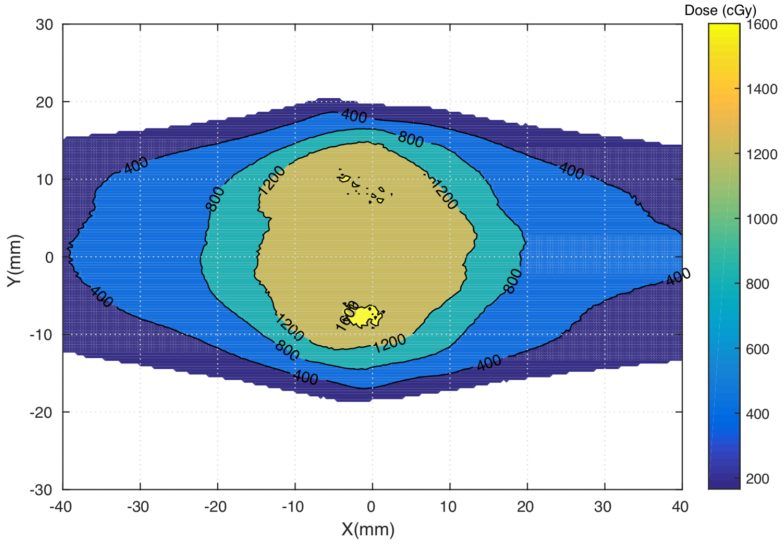

(c)

***Figura* 1.2:** Ejemplo de dosimetría con película radiocrómica: a) Trozo de película EBT3 sin irradiar leído en el escáner, b) trozo de película irradiado con plan de tratamiento y c) Mapa de dosis final.

1.2. Las películas radiocrómicas EBT3

En el desarrollo de esta tesis se han empleado películas del modelo EBT3. En particular, se ha trabajado con películas de tamaño $203 \times 254 mm^2$ sin ninguna referencia externa impresa. Además, cada caja de películas EBT3 recibida contenía un sobre negro con veinticinco películas u hojas individuales del mismo lote y un indicador que registra el historial de temperatura de las películas, permitiendo así un rápido chequeo de las condiciones de almacenaje y validación para el uso de las películas. Además, las cajas de película traen una fecha de caducidad más allá de la cual el fabricante desaconseja su uso.

Las películas EBT3 están formadas por una capa activa de unos $26-28\mu m$ de espesor emparedada entre dos capas de poliéster mate de unos $125\mu m$ de grosor, que protegen a la capa activa de daños físico-químicos y/o mecánicos. Según el fabricante, la capa activa contiene los cristales monoméricos de diacetilo, LiPCDA, así como un tinte marcador y otros compuestos que ayudan a que la respuesta de la película sea independiente del espectro energético de la radiación. Tal y como se describe en los trabajos de Devic y col. [4] y Schoenfeld y col. [27], estos cristales tienen forma de varilla, con unas dimensiones de $2\mu m$ de ancho y $15\mu m$ de largo y se distribuyen parcialmente ordenados, orientados paralelamente al lado más corto de la película. Además, según el estudio espectroscópico de Callens y col. [28], la exposición de la película EBT3 a la radiación produce dos conformaciones diferentes de polímeros de polidiacetileno con diferentes propiedades de absorción luminosa. Así pues, los cambios en la configuración electrónica del compuesto activo dan lugar a una absorción de la luz dependiente de la dosis, que es el efecto medible con un dispositivo de lectura, ya sea un densitómetro o un escáner de sobremesa.

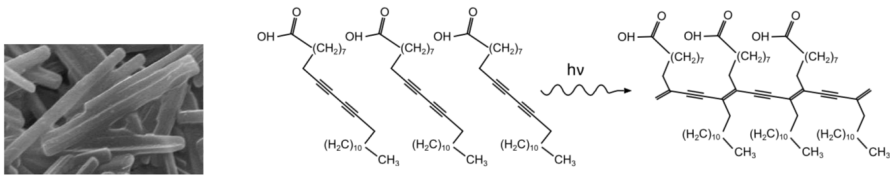

(a) (b)

***Figura* 1.3:** La estructura de la película radiocrómica EBT3: a) cristales de monómero, tomado de Devic y col. [4], b) Reacción de polimerización inducida por la radiación, tomado de Callens y col. [28]

La absorbancia es la magnitud encargada de proporcionar una medida de la atenuación de luz de una determinada longitud de onda debida a los fenómenos de absorción y difusión. Tal y como se describe en el trabajo de

Callens y col. [29], en el caso de la película EBT3, la absorción es debida al tinte marcardor y a las moléculas de polidiacetileno; mientras que las partículas de sílice en la capa de poliéster, los monómeros de cristal y las moléculas de polidiacetileno en la capa activa son las que contribuyen a la dispersión de la luz. Además, como puede verse en la figura 1.4, en el rango de 0 a $10Gy$, la mayor absorción de la luz que atraviesa la película se encuentra en el rango de los 500 hasta los $750nm$ de longitud de onda (color rojo), debido a la existencia de dos picos en el espectro de absorción, situados en 585 y $635nm$. Por tanto, cuando se emplea luz en este rango de longitud de onda para la lectura de la película irradiada, la absorbancia se incrementa con la dosis como resultado de la concentración de moléculas de polidiacetileno. A dosis de irradiación superiores a los $10Gy$, se incrementa la absorbancia neta a otras longitudes de onda (color verde) fuera del intervalo anteriormente comentado; mientras que para irradiaciones superiores a los $20Gy$, la alta absorbancia dificulta la detección de la poca cantidad de luz de la zona roja que atraviesa la película.

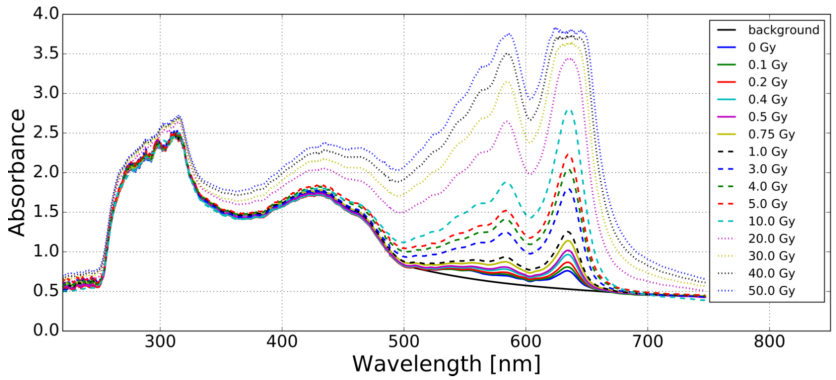

***Figura* 1.4:** Absorbancia de la película radiocrómica en función de la dosis de exposición y de la longitud de onda de la luz que la atraviesa, tomada de Callens y col. [29]

La ley de Beer y Lambert [30], que propone una relación lineal entre la absorbancia y la concentración del compuesto responsable de la atenuación de la luz, se cumple sólo bajo estrictas condiciones [29] que no incluyen, por ejemplo, la dispersión de la luz. En el campo de la dosimetría con película radiocrómica existen múltiples factores, como son la formación de dos polímeros distintos con diferentes propiedades de absorción, la dispersión de la luz y la relación entre dosis de irradiación y concentración de monómeros, que pueden alejarnos del cumplimento de esta ley.

Recientemente, el fabricante ha presentado el nuevo modelo de películas EBT-XD, con la misma estructura de las películas EBT3, aunque, con un

espesor nominal de la capa activa de $25\mu m$, ligeramente inferior al del modelo anterior. Además, tal y como se detalla en los trabajos de Schoenfeld y col. [31] y Devic y col. [4], los monómeros de cristal activo de este modelo tienen un menor tamaño y hay una menor ordenación en la orientación de los cristales. Estas propiedades se traducen en una disminución de la luz dispersada y una menor atenuación en la lectura de la película EBT-XD para una dosis dada respecto al modelo EBT3. Por tanto, una las principales consecuencias de los cambios introducidos en la composición del modelo EBT-XD es la ampliación del rango de medida de dosis para esta película, pues la saturación de la lectura se alcanzará a dosis mayores.

Finalmente, se debe mencionar que una de las características de las propiedades ópticas de los materiales radiocrómicos, y, por ende, de todos los modelos de película radiocrómica, es la variación de la absorbancia con el tiempo post-irradiación [32, 33]. Es decir, la irradiación de las películas radiocrómicas produce cambios visibles instantáneamente, a pesar de que el proceso de polimerización desencadenado se extiende en el tiempo, siendo la variación de las propiedades ópticas importante en las primeras horas posteriores a la irradiación y haciéndose prácticamente despreciable a partir de las 48 o $72h$.

1.3. Dispositivos de lectura: escáneres de sobremesa

Un densitómetro es un instrumento que mide la atenuación de la luz a través de un material semitransparente. Por tanto, los densitómetros suelen llevar acoplada una fuente de luz, normalmente de espectro estrecho, para medir la intensidad absoluta o relativa de la luz de una longitud de onda conocida que atraviesa el material. Se pueden encontrar ejemplos de utilización de este tipo de dispositivos para la dosimetría de película radicrómica, como es el caso del dispositivo descrito en Lee y col. [34], usado para la medida de mapas de dosis de radiocirugía con película radiocrómica en Lee y col. [9]. Así pues, en este densitómetro, la longitud de onda de la fuente de luz se ajusta externamente para hacerla coincidir con uno de los picos de absorción de la película. Además, la luz que atraviesa la película se focaliza con un microscopio sobre un dispositivo acoplado por carga, CCD (Charged Couple Detectors, por sus siglas en inglés), que proporciona una señal digital a partir de la luz recibida. Finalmente, el dispositivo cuenta con un soporte motorizado para ir desplazando la película y conseguir un mapeo bidimensional de

la distribución de dosis absorbida presente en la misma.

En el campo de la dosimetría con película radiocrómica, la práctica más extendida [23-26, 35] es el empleo de escáneres de sobremesa. Estos dispositivos, a diferencia del densitómetro previamente descrito, trabajan con una fuente de luz de espectro ancho, que emite en todo el espectro visible (o gran parte del mismo). Normalmente, la mayoría de modelos pueden funcionar en modo reflexión, esto es, midiendo la luz que se refleja en la película radiocrómica como se ha estudiado en Méndez y col. [36]. No obstante, el modo de funcionamiento más habitualmente empleado y recomendado para la dosimetría con película radiocrómica es el modo transmisión, en el cual se mide la luz que ha atravesado la película. Históricamente, se han empleado varios modelos y marcas de escáneres, aunque, actualmente, los escáneres EPSON™ en general, y el modelo 10000XL en particular, son los más ampliamente referenciados y empleados para realizar dosimetría con película.

A continuación, describiremos en detalle el funcionamiento general de los escáneres EPSON, si bien, el funcionamiento general de escáneres de otros fabricantes suele ser similar. Los escáneres se operan a través de un software, que permite seleccionar los parámetros del escaneo, tales como resolución, ajustes de color, filtros de imagen, manipulación del histograma, etc., instalado en un ordenador donde se almacenan las imágenes digitales adquiridas. Tal y como se aprecia en la figura 5, estos escáneres tienen una cama de cristal transparente sobre la que se sitúa la película y una tapa que se cierra sobre la cama para evitar que entre luz ambiente. Antes de empezar a operar, el escáner hace una imagen con baja calidad, *preview*, que permite seleccionar el área de escaneo, es decir, el tamaño de la imagen que se va a obtener.

Una vez dada la orden de escanear, previamente al escáneo en sí, el escáner realiza una autocalibración de los detectores midiendo la luz de la fuente luminosa que atraviesa el aréa de autocalibración, ver figura 1.5. Después, la fuente luminosa lineal se mueve por debajo de la cama del escáner, perpendicularmente a su dimensión lineal para mapear el campo de escaneo seleccionado. Durante este movimiento, la fuente emite luz que, tras atravesar la película radiocrómica y un colimador lineal, es recogida y dirigida mediante un sistema óptico formado por algunos espejos y lentes hasta una línea o líneas de detectores CCD, como se describe en el trabajo de Schoenfeld y col. [37]. En el modo reflexión, el funcionamiento es análogo, salvo que se recoge la luz reflejada que sigue un camino óptico diferente hasta llegar a los detectores.

Para poder proporcionar una imagen en color RGB (rojo, verde y azul por

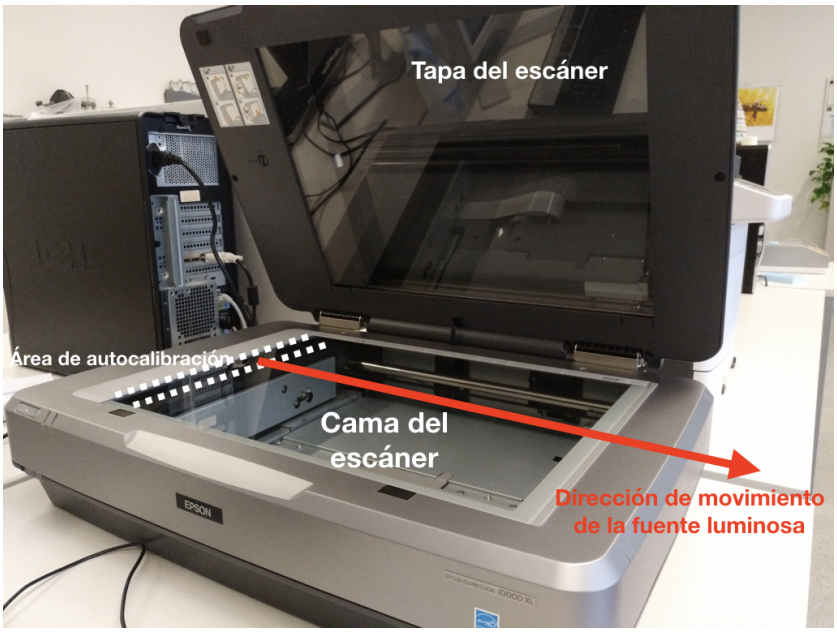

***Figura* 1.5:** Partes de un escáner EPSON

sus siglas en inglés: Red, Green, Blue), los escáneres trabajan con varias líneas de detectores CCD, con filtros superimpuestos de colores rojo, verde y azul. Así pues, la conversión de la luz a señal digital se realiza en la célula CCD de cada píxel, formada por el filtro de color y un fotodiodo. Estos detectores tienen forma cuadrada y presentan una mayor sensibilidad en el centro del detector que en los bordes. Por este motivo, el fabricante añade micro-lentes encargadas de focalizar la luz en el centro del detector CCD, aumentando la sensibilidad y la relación señal ruido de la señal eléctrica obtenida, como se esquematiza en la figura 1.7(a). El fabricante también ha desarrollado una nueva tecnología, denominada *EPSON DOUBLE CCD TECHNOLOGY*^{TM}, consistente en una matriz de seis líneas de detectores, dos por canal. Así pues, en realidad, hay dos líneas de detectores dedicadas a medir cada canal, como se muestra en la figura 1.7(b). Cada línea de cada canal de color está desplazada la longitud de medio detector respecto a la otra y cada píxel se muestrea doblemente, una vez en cada línea, para evitar que la pérdida de sensibilidad en el centro de los detectores CCD se traduzca en un aumento de ruido.

En esta tesis se ha investigado la influencia en la dosimetría del modelo EPSON EXPRESSION 10000XL y del EPSON PERFECTION V800 Photo, modelo más moderno. Ambos escáneres comparten el modo de funcionamiento previamente descrito, aunque, existen algunas diferencias entre

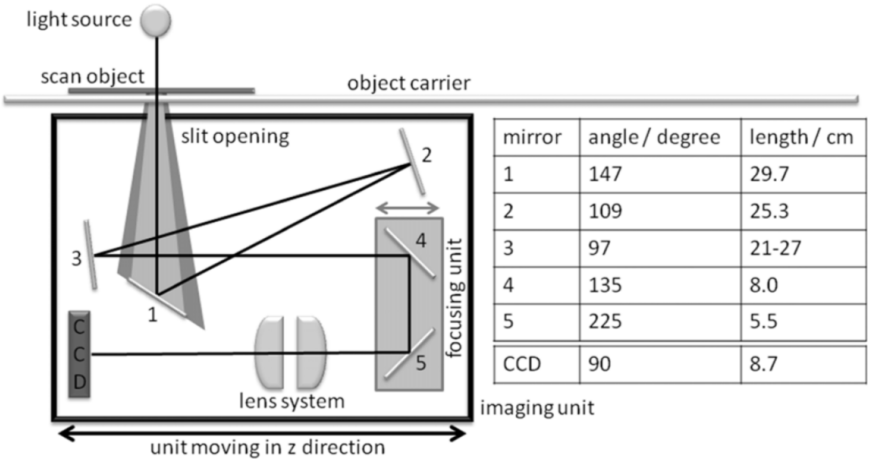

mirror	angle / degree	length / cm
1	147	29.7
2	109	25.3
3	97	21-27
4	135	8.0
5	225	5.5
CCD	90	8.7

***Figura* 1.6:** El proceso de lectura en modo transmisión, tomada de Schoenfeld y col. [37]

ellos. En primer lugar, el primer modelo tiene un tamaño máximo de escaneo de $310 \times 437mm^2$, mientras que el segundo tiene un campo máximo de $216 \times 297mm^2$. En segundo lugar, el primer modelo emplea una lámpara fluorescente de cátodo frío con gas Xenón, mientras que el segundo utiliza una fuente de LED blanco e infrarrojos. En tercer lugar, la máxima resolución del primer modelo es de $2400ppp$ (píxeles por pulgada), mientras que la máxima resolución del segundo modelo es de $4800ppp$.

En general, los escáneres de sobremesa trabajando en modo transmisión no miden la intensidad de luz transmitida para una determinada longitud de onda. Más bien, proporcionan una medida de la intensidad de luz transmitida a lo largo de todas las longitudes de onda [3] emitidas por la fuente. Si denominamos $E(\lambda)$ a la emisividad espectral de la lámpara del escáner, $A(\lambda)$ al espectro de absorción (función que describe la fracción de la radiación incidente absorbida por un material en un rango de frecuencias) y $S_C(\lambda)$ a la sensibilidad del detector del canal empleado (rojo, verde o azul), encontramos para la intensidad detectada la ecuación 1.1,

$$I_C = \int_0^{inf} E(\lambda)A(\lambda)S_C(\lambda)\, d\lambda C \qquad = R, G, B, \tag{1.1}$$

Sin embargo, los valores de píxel en un canal de la imagen digital no se corresponden con las intensidades descritas en la ecuación 1.1. En su lugar, esta intensidad medida por el detector está cuantizada y digitalizada según la profundidad de bits empleada para la lectura. Por tanto, los valores de píxel son números enteros debido a este proceso de medida, cuantización y

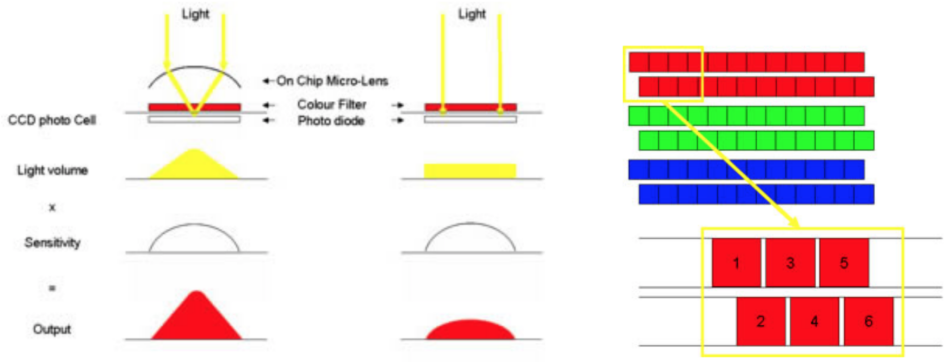

(a) (b)

***Figura* 1.7:** Formación de la imagen en los detectores CCD: a) efecto de los microlentes y b) *DOUBLE CCD TECHNOLOGY*^{TM} de EPSON. Imágenes tomadas de http://content.epson.it/maco/technology/scanners/ccd.htm

digitalización. Así por ejemplo, para la profundidad de color comúnmente utilizada en dosimetría con película radiocrómica de 16 bits por canal, la máxima intensidad transmitida corresponde a un valor de píxel de $65535 = 2^{16} - 1$, si la mínima corresponde a un valor de 0; o a un valor de $65536 = 2^{16}$, si la mínima corresponde a un valor de 1. Por tanto, para cada canal de color, el valor de píxel en modo transmisión se relaciona directamente con la transmitancia de la luz policromática de la fuente al atravesar la película radiocrómica y ser leída con el detector correspondiente al canal de color. En el caso de los escáneres EPSON, antes de cada lectura se realiza una autocalibración de los detectores CCD, ver figura 1.5, para compensar las posibles variaciones de la fuente de iluminación. Así pues, en estos casos, el valor de píxel es una medida de la transmitancia relativa respecto al estado y la emisividad de la fuente luminosa.

Los escáneres de sobremesa proporcionan una distribución espacial de la intensidad transmitida, ya que, los píxeles de la imagen se distribuyen regularmente sobre el campo de escaneo definido y con la resolución previamente elegida. Es decir, los escáneres proporcionan un muestreo espacial, en una cuadrícula regular, de la distribución de transmitancias. Por tanto, los valores del mismo píxel en cada canal de color se asocian a la transmisión de la luz del mismo punto de la película leída con tres detectores diferentes. Matemáticamente, la imagen digital de color de la película se corresponde con tres matrices, una por canal de color, que almacenan los valores de las transmitancias cuantizadas y digitalizadas, como se esquematiza en la figura 1.8.

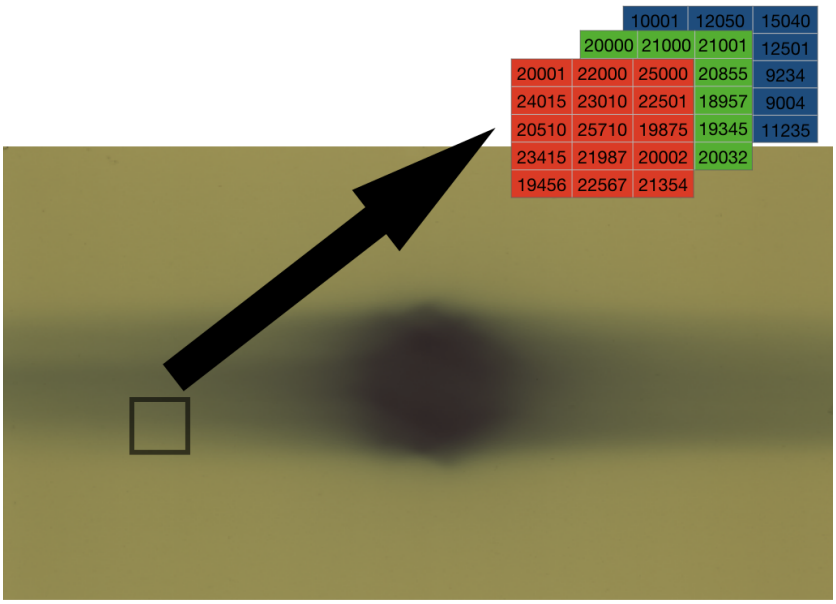

***Figura* 1.8:** Imagen digitalizada de un trozo de película irradiado, con detalle de valores de píxel en los tres canales, rojo, verde y azul.

1.3.1. Efectos de los escáneres en la dosimetría con película

La dosimetría con película radiocrómica y escáner se debe realizar teniendo en cuenta ciertos aspectos prácticos que eviten la introducción de errores. Además, es conveniente conocer las limitaciones que el proceso de lectura con el escáner introduce en la dosimetría.

En primer lugar, el escáner se debe encender una media hora antes de su uso y, posteriormente, se deben realizar unos siete escaneos [23] de todo el campo disponible de escaneo, para calentar correctamente la lámpara y la electrónica. También se debe dejar transcurrir un tiempo de dos minutos [38] entre escaneos consecutivos . Este intervalo de tiempo minimiza el aumento de la temperatura en la cama del escáner, que se traduce en una variación de la respuesta leída, no relacionada con la dosis absorbida en la película, y que da lugar a un error en la estimación de dosis como se muestra en el trabajo de Lynch y col. [26].

En segundo lugar, la película se debe situar siempre en la misma orientación en la cama del escáner. En la orientación vertical, el lado más largo de la película es paralelo al lado más largo de la cama del escáner; mientras

que, en la orientación horizontal, el lado más corto de la película es paralelo al lado más largo de la cama del escáner, ver figura 1.9. Inclulo si la película se recorta, se debe conservar la orientación de los trozos para su lectura[4]. La orientación de las fibras activas de la película polariza parcialmente la luz transmitida a través de la misma, lo que produce en una diferencia en las respuestas leídas entre la orientación horizontal y la vertical que puede llegar al 5 %, y que, por supuesto, no es debida a la dosis absorbida sino a un protocolo de lectura de película incorrecto.

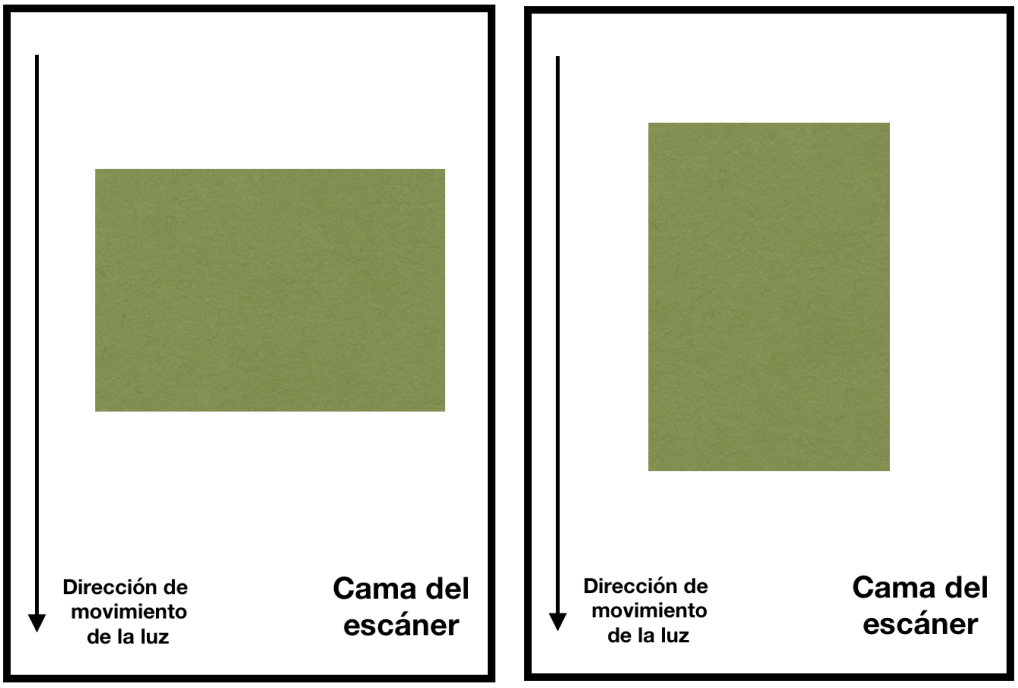

(a) (b)

***Figura* 1.9:** Colocación de la película en la cama del escáner: a) Orientación horizontal y b) Orientación vertical

En tercer lugar, a la hora de escanear la película, esta se debe fijar a la cama del escáner, evitando que se curve y que aparezcan diferencias de espesor en la capa de aire entre la cama del escáner y la propia película. Cuando no se corrigen estos defectos de posicionamiento de la película, tal y como se describe en Lewis y Devic [38], las lecturas así obtenidas dan lugar a estimaciones de dosis erróneas. El método recomendado para evitar estos defectos es el empleo de una lámina de cristal superimpuesta a la película, que cubra toda la cama del escáner (incluyendo la zona de autocalibración).

En cuarto lugar, hay que tener presente que la lectura de la película en el escáner introduce ruido en la imagen digital. Concretamente, el uso de los detectores CCD [39, 40] es responsable de introducir parte del ruido presente en la dosimetría. Además, la cantidad de ruido de la lectura de la película depende del modelo de escáner y de la resolución espacial empleada, cumpliéndose que al aumentar la resolución, aumenta la cantidad de ruido presente en la lectura.

En último lugar, aparece el denominado efecto o artefacto lateral, introducido al leer la película en el escáner [23, 26] y caracterizado por la diferencia de respuesta (valores de píxel) entre el eje del escáner coincidente con la dirección de movimiento de la lámpara y puntos situados a una distancia cualquiera en la dirección perpendicular a dicho eje. En la zona central del escáner, es decir una zona de unos $2,5cm$ de anchura aproximadamente alrededor del eje mencionado, no hay efecto lateral [41] o es muy pequeño. Este artefacto suele tener forma de parábola, como muestran los trabajos de Menegotti y col. [42], Poppinga y col. [41] y Lewis y Chan [43], que también proponen algoritmos para su mitigación.

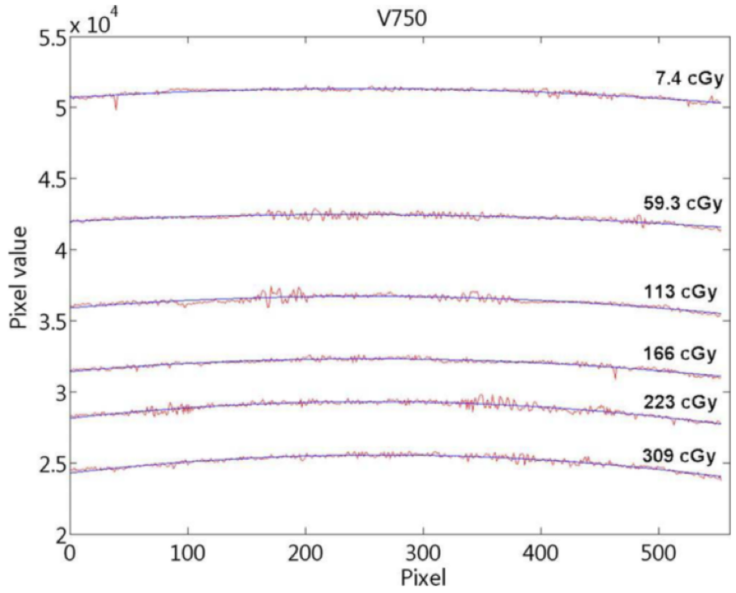

***Figura* 1.10:** Detalle del efecto lateral, tomado de Menegotti y col. [42]

El origen del artefacto lateral se encuentra en la polarización de la luz del escáner cuando atraviesa la película, como se demuestra en los trabajos de Schoenfeld y col. [37], y Schoenfeld y col. [27]. Este artefacto depende del

escáner, de la dosis, del modelo de película empleado y de la orientación de la película en la cama del escáner. Así pues, las películas EBT-XD, debido al tamaño y disposición de los monómeros en la capa activa, presentan menor afectación [31, 44, 45] por este artefacto con respecto a las EBT3, cuando ambas películas se irradian con la misma dosis. Además, el impacto de este efecto es menor cuando ambos modelos de películas se orientan verticalmente en la cama del escáner que cuando lo hace horizontalmente.

Por otra parte, en la dirección del movimiento de la lámpara no se han reportado artefactos significativos, y suele asumirse como una zona de respuesta homogénea. Aunque, esta característica puede variar entre distintos aparatos incluso del mismo modelo, por lo que se recomienda verificar la estabilidad de la respuesta en esta dirección, a la par que se comisiona, mide o verifica el efecto lateral. Los escáneres que se emplean para dosimetría física deben de ser considerados como un instrumento de medida más del servicio o departamento y deben de ser sometidos a revisiones periódicas de control de calidad.

1.4. Metodología de manipulación, irradiación, lectura y calibración de las películas radiocrómicas

En esta sección se presentan las recomendaciones tradicionales para la manipulación de las películas radiocrómicas, así como la metodología general seguida a lo largo de las investigaciones de esta tesis. Si bien, se debe de entender que, en los artículos que componen el documento de tesis, pueden existir desviaciones respecto a esta metodología para estudiar algún fin concreto. En cualquier caso, dichas desviaciones estarán explicitadas en la sección de metodología del artículo correspondiente.

Las recomendaciones más ampliamente seguidas para la manipulación de las películas radiocrómicas se presentan en el trabajo de Niroomand-Rad y col. [46]. A pesar de su baja sensibilidad a la radiación visible, se deben almacenar en envoltorios opacos en un ambiente fresco y seco para evitar cambios en las propiedades químicas de las mismas. Además, se deben manejar con guantes para evitar imprimir huellas digitales en las mismas y se deben recortar empleando una guillotina, con una antelación de al menos $24h$ previas a su irradiación, minimizando así el impacto en la dosimetría de las tensiones mecánicas que aparecen en los bordes de los trozos recortados.

La irradiación de las películas se realiza, normalmente, en maniquíes de materiales plásticos [47] equivalentes a agua, como el RW3. En concreto, en los trabajos que componen esta tesis, para la irradiación de planes de tratamiento se utilizaron, sobre todo, los maniquíes EASYCUBE^{TM}y MULTICUBE^{TM}(IBA Dosimetry GmbH, Alemania). Para los casos en los que se precisaba irradiar en un medio homogéneo equivalente a agua con una geometría controlada, se empleó un maniquí formado por láminas cuadradas de RW3, con una superficie de $30 \times 30\, cm^2$ y $1cm$ de espesor. En concreto, las calibraciones de los diferentes lotes de películas radiocrómicas estudiados se llevaron a cabo con este maniquí de láminas de material plástico equivalente a agua.

Debido al cambio de las propiedades ópticas de la película con el tiempo post-exposición, una vez irradiados todos los trozos de una película y transcurrido el intervalo de tiempo fijado entre irradiación y lectura, se realiza la digitalización. Para obtener estimaciones de dosis correctas, o bien el intervalo de tiempo entre irradiación y lectura se mantiene fijo para todas las películas del lote, incluyendo a la de calibración, como se discute en Martišíková y col. [48]; o bien se utilizan protocolos de compensación de variabilidades como los descritos en Lewis y col. [49], y Ruiz-Morales y col. [50]. Normalmente, se trabajó con un intervalo de tiempo entre la irradiación y la lectura de la película de 4 o $6h$, aunque, en algunas ocasiones, se trabajó con intervalos de $24h$ o superiores, ya que las investigaciones así lo requerían.

La lectura de cada película se realiza con la película situada en disposición vertical en la cama del escáner para minimizar el efecto lateral y centrada respecto al eje definido por la dirección de movimiento de la lámpara. Para obtener las imágenes, se desactivan todas las correcciones de color y se realizan escaneos con resoluciones de $72ppp$ o $150ppp$ normalmente, si bien, para algunos estudios se consideraron otras resoluciones. Las imágenes se almacenan en formato TIFF (de las siglas en inglés, Tagged Image File Format) para su posterior análisis con programas propios desarrollados bajo la plataforma de cálculo científico MATLAB^{TM}y su lenguaje propio de programación.

La calibración se realiza irradiando trozos de una misma película, la película de calibración, a dosis conocidas. Esta película se recortó, normalmente, en $N = 8$ tiras horizontales de $25{,}4 \times 254 mm^2$ que se irradiaron con fotones de $6MV$ de energía nominal en aceleradores lineales VARIAN^{TM}. Además, se emplearon haces de irradiación con un tamaño nominal $200 \times 200 mm^2$ en el isocentro. Así mismo, las tiras de película, situadas en el isocentro, se colocaron en el interior del maniquí formado con veinte láminas de RW3 (con una profundidad total de $200mm$) a una profundidad de $100mm$

para asegurar el equilibrio electrónico en el punto de medida. Las dosis de irradiación de los trozos de calibración se distribuyeron uniformemente desde $0Gy$, es decir, siempre se dejó un trozo de película sin irradiar, hasta la dosis máxima de calibración que, normalmente, fue de 11 o $12Gy$ para cubrir el rango de dosis recomendado de las películas EBT3. Antes de la irradiación de los trozos, se determinó la dosis en el punto de medida con la película, con una cámara cilíndrica y un electrómetro, empleando la misma geometría y el mismo maniquí, haciendo coincidir el punto efectivo de la cámara con el punto donde se situó el centro de las tiras de película.

Las curvas de calibración se obtienen relacionando la lectura de la película de calibración con las dosis de irradiación de los trozos de dicha película. En particular, la respuesta a una dosis de irradiación se caracteriza analizando la lectura en un ROI (región de interés, por sus siglas en inglés, Region Of Interest) de $20 \times 20mm^2$ de la tira expuesta a dicha dosis. Así pues, los ROIs de las tiras de calibración se escogen, por un lado, centrados en el interior de cada tira, evitando así los efectos en el perímetro de las tiras debido al recorte de la película; y, por el otro lado, simétricos respecto al eje definido por la dirección de movimiento de la lámpara, evitando ahora el efecto lateral del escáner. Así pues, para cada canal de color, se pueden obtener N pares de puntos de la forma $[D_i, I_{i,C}] \quad i = 1, .., N \quad C = R, G, B$, donde D_i e $I_{i,C}$ son las dosis de exposición y las respuestas en el canal de color C, respectivamente. Finalmente, para cada canal de color, se pueden obtener la curva de calibración y sus parámetros a partir de un ajuste no lineal de la ecuación de la curva a los puntos experimentales.

1.5. Algoritmos empleados en dosimetría con película radiocrómica

En esta sección, presentamos los algoritmos empleados para la conversión a dosis de las lecturas de las películas, usando las curvas de calibración del lote. A diferencia del proceso de calibración, ahora no estamos interesados en analizar los valores promedios obtenidos en un ROI. En este caso, normalmente, estamos interesados en estimar la dosis de cada uno de los píxeles de la imagen digital, para explotar la alta resolución espacial del dosímetro y obtener mapas de dosis. Ahora bien, si lo que se desea es una estimación de dosis, y la película o el trozo en cuestión ha estado uniformemente irradiado, también pueden hacerse promedios de los valores de píxel o de las estimaciones de dosis en un ROI, mitigando así los efectos del ruido.

A partir de las propiedades ópticas de una película irradiada, descritas en la sección 1.2, se infiere la conveniencia de usar las lecturas del canal rojo, debido a la mayor absorción dependiente de la dosis en este canal. Además, tal y como se comprueba en las curvas de calibración, este canal presenta el mayor rango dinámico para dosis bajas, especialmente, las comprendidas en el intervalo de 0 a 4 o $6Gy$. Esto justifica el uso de los algoritmos monocanal y, concretamete, de la dosimetría monocanal con el canal rojo.

No obstante, para aumentar el rango dosimétrico de uso de la película radiocrómica y optimizar su aprovechamiento, es conveniente emplear el canal que presente mayor sensibilidad a la exposición a la radiación según el intervalo de dosis de trabajo, tal y como se describe en Devic y col. [51]. Por tanto, se abre la puerta a la dosimetría monocanal con otros canales diferentes del rojo, especialmente el verde. En el caso de los algoritmos multicanal considerados en esta tesis, independientemente del rango de dosis de la estimación, se emplean los tres canales simultáneamente para obtener una única estimación de dosis.

Finalmente, se debe destacar que, en la dosimetría con película radiocrómica, se evita la realización de extrapolaciones con las curvas de calibración del lote, independientemente del tipo de algortimo elegido, mono o multicanal.

1.5.1. Algoritmos monocanal

Los algoritmos monocanal trabajan con un canal de color de la imagen digital de la película y con la curva de calibración del lote para dicho canal de color. Por tanto, podemos encontrar tantas modificaciones de estos algortimos como curvas sensitométricas han sido propuestas. Además, cabe resaltar que, si bien el escáner proporciona valores de píxel, muchos de estos algoritmos proponen utilizar como respuesta otras magnitudes calculadas a partir de los valores de píxel, como son la densidad óptica o la densidad óptica neta. Aunque, la consideración de estas otras magnitudes no implica en ningún caso linealidad entre las respuestas en la película y las dosis absorbidas.

En algunos trabajos [52], se ha reportado la posibilidad de trabajar sin la corrección del efecto lateral con este tipo de algoritmos. Aunque esta decisión no es frecuente, es más, la mayoría de los autores y referencias [23, 26, 41-43] abogan por la corrección de dicho efecto. Por tanto, previamente a la conversión de las respuesta de la película a dosis, los valores de la respuesta en la película deben de corregirse para eliminar el efecto de parábola o lateral.

Dentro de este tipo de protocolos, podemos encontrar algunos que emplean los valores de píxel [49, 50] y una curva sensitométrica como la descrita en la ecuación 1.2,

$$PV_C = \alpha_C + \frac{\beta_C}{D - \gamma_C} \quad C = R, G, B, \tag{1.2}$$

donde PV_C son los valores de píxel del canal de color $C = R, G, B$, empleado para la dosimetría. Mientras que α_C, β_C y γ_C son los coeficientes de la curva de calibración para el canal seleccionado y D es la dosis estimada. Como puede verse en esta ecuación 1.2, la relación entre los valores de píxel y la dosis es fácilmente invertible.

Otra opción es considerar las respuestas en la película como valores de densidad óptica OD_C obtenidos a partir de los valores de píxel según la relación $OD_C = log(\frac{65535}{PV_C})$, donde el valor 65535 corresponde al máximo valor que pueden tomar los valores de píxel cuando se trabaja con 16 bits de profundidas por canal. Por tanto, la densidad óptica es el logaritmo decimal de la relación entre el máximo valor de píxel capaz de leer el escáner y el valor de píxel de la película. En el trabajo de Chung y col. [53] se elige una curva sensitométrica polinomial para relacionar las densidades ópticas con las dosis absorbidas, según la ecuación:

$$D = \alpha_C + \beta_C \cdot OD_C + \gamma_C \cdot OD_C^2 + \delta_C \cdot OD_C^3 \quad C = R, G, B, \tag{1.3}$$

Finalmente, otro de los protocolos que se pueden encontrar en la bibliografía [4] propone usar la densidad óptica neta NOD_C para evaluar la respuesta a la radiación ionizante en la película radiocrómica. Así pues, deben realizarse dos lecturas de la película, una previa y otra posterior a la irradiación; a continuación, se deben de registrar ambas imágenes y, finalmente, se puede calcular la densidad óptica neta como el cambio de densidad óptica de la película debido a la irradiación: $NOD = OD_{post} - OD_{pre} = log(\frac{PV_{pre}}{PV_{post}})$. Como en el caso de la densidad óptica y los valores de píxel, se obtienen valores de densidad óptica neta para cada canal, aunque, omitimos los subíndices por claridad. Para este protocolo, la curva que relaciona dosis de exposición y respuestas en la película es de tipo potencial, como se observa en la siguiente ecuación:

$$D = \alpha \cdot NOD + \beta \cdot NOD^{\gamma} \tag{1.4}$$

1.5.2. Algoritmos multicanal

Los algoritmos multicanal emplean las respuestas de la película en varios canales para obtener las estimaciones de dosis. Como ya se sabe, las respuestas más sensibles a la exposición a dosis de la película radiocrómica, se encuentran en el canal rojo en el rango de 0 a $10Gy$. A partir de este valor de dosis, este canal empieza a saturar y su respuesta presenta menor rango dinámico, no obstante, el canal verde presenta en esta región un rango dinámico aceptable. Por otra parte, las respuestas leídas en el canal azul son las más insensibles a las exposiciones a dosis de hasta $20Gy$, presentando un rango dinámico pobre que desaconseja su uso para dosimetría monocanal. Aunque, según el fabricante, las lecturas en este canal contienen información de la heterogeneidad espacial de la película.

Históricamente, el primer intento de dosimetría multicanal aparece para paliar la falta de homogeneidad espacial, descrita en los trabajos de Kairn y col. [54], y Hartmann y col. [55], que se encontró al pasar del modelo de películas EBT al modelo EBT2. El primer modelo de película EBT presentaba una gran homogeneidad espacial en su repuesta. Sin embargo, según el propio fabricante y como consecuencia del proceso de manufactura, la capa activa del modelo sucesor EBT2 no presentaba el mismo grado de homogeneidad espacial. En este contexto, en su documento International Specialty Products [56], el propio fabricante propone emplear la relación entre las respuestas de los canales rojo y azul para, por un lado aprovechar el rango dinámico del canal rojo para estimar la dosis y, por otro usar la información contenida en el canal azul para corregir la falta de heterogeneidad.

Posteriormente, se propone un nuevo algoritmo, descrito en el trabajo de Micke y col. [57], que trabaja simultáneamente con las respuestas de los tres canales para obtener las estimaciones de dosis. Este algoritmo es capaz de mitigar tanto las faltas de homogeneidad de la película como el efecto lateral. Finalmente, en el trabajo de Mayer y col. [58], se detallan completamente las ecuaciones del algoritmo anterior, a la vez que se propone un nuevo algoritmo multicanal. Además, también se comprueba en este trabajo que ambos algoritmos, a pesar de las diferencias en sus ecuaciones, conducen a resultados prácticamente idénticos.

Los modelos EBT y EBT2 están actualmente descatalogados y no se han reportado problemas en la homogeneidad del modelo EBT3. Sin embargo, las ideas y los algoritmos inicialmente propuestos en los desarrollos de Micke y col. [57], y Mayer y col. [58] se han convertido en los métodos más utilizados para la realización de la dosimetría con película radiocrómica. Además de la

mitigación del efecto de las heterogeneidades y de la corrección del efecto lateral, otro de los beneficios de estos algoritmos, según Mayer y col. [58], es la disminución de ruido en la dosimetría con película radiocrómica.

Finalmente, en la bibliografía se encuentran nuevos desarrollos de algoritmos multicanal, como los descritos en Méndez y col. [59], y Pérez Azorín y col. [60]. Los nuevos desarrollos multicanal tienen planteamientos similares, a partir de la respuestas leídas en los tres canales y las curvas de calibración de estos canales, se optimiza una función de coste para obtener el mapa de dosis. Sus diferencias residen en la consideración e hipótesis sobre la naturaleza del término que tiene en cuenta la perturbación.

1.5.2.1. Los algoritmos multicanal de Micke y cols y de Mayer y cols.

Las ecuaciones de estos algoritmos multicanal utilizan las curvas de calibración en cada canal, que relacionan las respuestas leídas en cada canal $I_C,\ C = R, G, B$ con la dosis de exposición D. Además, dichas curvas se pueden invertir, si es preciso, para obtener una relación de la siguiente forma: $D_C = f_C(I_C)$. Los parámetros de ajuste del canal considerado aparecen en estas relaciones. Si bien, ni estos parámetros, ni la dependencia funcional exacta descrita por f_C influyen en el desarrollo posterior, por tanto, se omiten por simplicidad y claridad.

A continuación, siguiendo el desarrollo de Mayer y col. [58], asumimos que, en cada píxel caracterizado por las coordenadas espaciales (i, j), existe una perturbación independiente del canal, $\Delta(i, j)$, relacionada con variaciones de espesor de la capa activa y de iluminación en ese punto. La presencia de esta perturbación afecta a la dosis obtenida para cada píxel en cada canal. Así pues, si llamamos $a_C = \frac{\partial f_C}{\partial I_C}$ siguiendo un desarrollo de Taylor de primer orden, obtenemos

$$D_C(i, j) + a_C(i, j) \cdot \Delta(i, j) \tag{1.5}$$

En este momento es preciso señalar que, según el desarrollo de Micke y col. [57], esta perturbación no afecta al proceso de calibración debido a que se promedia la respuesta de la película en un ROI, es decir, se promedia un número de píxeles suficientemente grande. Así pues, en el proceso de calibración, se considera un valor promedio de las respuestas de película en un ROI y, por tanto, se obtiene un promedio de la perturbación $\overline{\Delta}$ sobre todos los píxeles del ROI. Ahora bien, si por definición se considera que $\Delta(i, j)$ tiene en cuenta las pequeñas variaciones espaciales de espesor de la capa

activa y de iluminación, respecto a la situación ideal de espesor e iluminación uniforme, parece lógico asumir que, al promediar en un ROI, estas variaciones se compensarán, dando lugar a una curva de calibración libre del efecto de estas variaciones. Por otro lado, cabe recordar que, para puntos alejados del centro del eje del escáner, el efecto lateral es función de la distancia al eje del escáner, la dosis de exposición del punto y el canal de lectura, lo que se sale del ámbito de definición de la perturbación $\Delta(i,j)$. Por tanto, el efecto lateral se mitigará sólo parcialmente con estos algoritmos.

Volviendo al desarrollo de Mayer y col. [58], si denominamos $D(i,j)$ a la dosis desconocida en el píxel de coordenadas (i,j), podemos plantearnos un funcional que tenga en cuenta la suma de las diferencias cuadráticas entre la dosis obtenida en cada canal y la dosis a la que se irradió dicho píxel. Así pues, para cada píxel se obtiene un funcional $\Phi(\Delta(i,j), D(i,j))$, con la siguiente expresión:

$$\Phi(\Delta(i,j), D(i,j)) = \sum_C (D_C(i,j) + a_C \cdot \Delta(i,j) - D(i,j))^2 \quad C = R, G, B, \tag{1.6}$$

Y ahora, se buscan valores, tanto de la perturbación como de la dosis para minimizar este funcional. Es decir, se calculan la perturbación y la dosis en cada punto a partir de la resolución simultánea de las siguientes ecuaciones:

$$\frac{\partial \Phi}{\partial \Delta}(\Delta(i,j), D(i,j)) = 0 \tag{1.7}$$

$$\frac{\partial \Phi}{\partial D}(\Delta(i,j), D(i,j)) = 0 \tag{1.8}$$

Llegamos así a las soluciones de Mayer y col. [58] tanto para la dosis como para la perturbación de cada píxel:

$$D(i,j) = \frac{D_{ave}(i,j) - wt(i,j)\dfrac{\sum_C D_C(i,j) \cdot a_C(i,j)}{\sum_C a_C(i,j)}}{1 - wt(i,j)}, \tag{1.9}$$

$$\Delta(i,j) = \frac{\sum_C (D(i,j) - D_C(i,j)) \cdot a_C(i,j)}{\sum_C a_C^2(i,j)}, \tag{1.10}$$

En las que se ha tenido en cuenta las siguientes abreviaturas:

$$D_{ave}(i,j) = \frac{1}{3}\sum_{C} D_C(i,j), \tag{1.11}$$

$$wt(i,j) = \frac{1}{3}\frac{(\sum_{C} a_C(i,j))^2}{\sum_{C} a_C^2(i,j)}, \tag{1.12}$$

En el caso del algoritmo de Micke y cols, tal y como se detalla también en el trabajo de Mayer y col. [58], la diferencia está en el funcional escogido que ahora minimiza las diferencias cuadráticas entre las dosis de los diferentes canales. Por tanto, si llamamosΩ ($\Delta(i,j)$) a este funcional, obtenemos:

$$\Omega(\Delta(i,j)) = \sum_{C\neq L}(D_C(i,j) + a_C(i,j)\cdot\Delta(i,j) - (D_L(i,j) + a_L(i,j)\cdot\Delta(i,j)))^2 \quad C,L = R,G,B \tag{1.13}$$

Y, ahora, la condición de que dicho funcional sea mínimo, $\frac{d\Omega}{d\Delta}(i,j) = 0$, nos permite obtener la perturbación en cada punto:

$$\Delta(i,j) = -\frac{\sum_{C\neq L}(D_C(i,j) - (D_L(i,j)) - \cdot(a_C(i,j) - a_L(i,j))}{\sum_{C\neq L}(a_C(i,j) - a_L(i,j))^2} \quad C,L = R,G,B \tag{1.14}$$

Según el trabajo de Mayer y col. [58] que estamos siguiendo, ahora la dosis multicanal se obtiene como la media ponderada de la dosis en los tres canales con la expresión de la perturbación obtenida anteriormente:

$$D(i,j) = \frac{\sum_{C}(D_C(i,j) + a_C\cdot\Delta(i,j))}{3} \tag{1.15}$$

Una vez obtenidas las ecuaciones de ambos algoritmos multicanal, cabe destacar que ambos métodos son comparados en el propio trabajo de Mayer y col. [58] y, según se reporta, dan lugar a estimaciones de dosis prácticamente iguales. Además, a pesar de obtener valores de la corrección y de la dosis multicanal para cada píxel, estas ecuaciones, correctamente implementadas, permiten calcular mapas de dosis en tiempos inferiores al segundo.

1.6. Objetivos de esta tesis

Esta tesis doctoral se dedica a la mejora de la dosimetría con película radiocrómica mediante el estudio del ruido presente en la misma y el análisis de la incertidumbre de las estimaciones de dosis obtenidas con este tipo de dosimetría.

El primer objetivo de esta tesis, desarrollado en el capítulo 2, es el estudio de las dependencias estadísticas entre las respuestas de los diferentes canales de color y su repercusión en la dosimetría multicanal. Por un lado, de cada píxel de la imagen se obtienen tres estimaciones diferentes correspondientes a las lecturas en los tres canales de color. Por otro lado, las lecturas de cada detector CCD están afectadas por ruido [39, 40], es decir, variaciones aleatorias de la señal. El estudio de la dependencia entre canales también se lleva a cabo con el ruido. Para este propósito, el ruido en cada canal se obtiene a partir de una descomposición *wavelet*, como la banda de más alta frecuencia de la descomposición. Así pues, comprobamos que la señal de los distintos canales está altamente correlacionada, mientras que el ruido presenta una correlación débil y discutimos la implicación de esta relación estadística en la dosimetría con algoritmos multicanal.

El segundo objetivo de la tesis, desarrollado en el capítulo 3 es proporcionar un modelo para el cálculo de incertidumbres en película radiocrómica. En el campo de la dosimetría con película radiocrómica, se han realizado estimaciones de incertidumbre aplicando la ley de propagación de la incertidumbre a estimaciones de dosis con algoritmos monocanal [23, 35, 48, 61]. Sin embargo, el cálculo de incertidumbres con algoritmos multicanal no se había abordado hasta ahora. Entre otros factores, el empleo simultaneo de las calibraciones de los tres canales, las propias ecuaciones para estimar la dosis de los algoritmos multicanal y la relación estadística entre las respuestas de los tres canales plantean un escenario difícil para la aplicación de la ley de propagación de las incertidumbres, descrita en Joint Committe for Guides in Metrology [62]. Por este motivo, proponemos un modelo multietapa para el cálculo de incertidumbre con técnicas Monte-Carlo, que utiliza los resultados de la caracterización estadística de las lecturas de película para poder modelizar las funciones de densidad de probabilidad conjunta de las respuestas de los tres canales.

El tercer objetivo, desarrollado en el capítulo 4, es la cuantificación de las fuentes de ruido en la incertidumbre con película radiocrómica. El ruido está presente en el todo el proceso dosimétrico con película radiocrómica. Desde

la propia deposición de la dosis en la película [61], hasta la generación de la señal eléctrica a partir de la luz incidente en los detectores CCD [40], pasando por la dispersión de la luz del escáner en el proceso de lectura [27]. Así pues, aplicamos a la dosimetría con película radiocrómica un procedimiento empleado en el análisis del ruido de cámaras digitales y escáneres de sobremesa para separar las fuentes del ruido presentes en las lecturas de las películas radiocrómicas. Además, estudiamos la propagación del ruido presente en la imagen digital a los mapas de dosis obtenidos con diferentes algoritmos, es decir, investigamos como los diferentes tipos de algoritmos pueden amplificar o disminuir el ruido presente. Finalmente, aplicamos esta metodología a dos modelos diferentes de escáneres empleados en la dosimetría con película radiocrómica y comprobamos las diferentes cantidades de ruido que añaden estos modelos.

Nuestro cuarto objetivo, desarrollado en el capítulo 5, es la mitigación del ruido temporal introducido en el proceso de lectura de la dosimetría con película radiocrómica, que para el modelo de escáner EPSON 10000XL tiene un valor alto. Este tipo de ruido se puede mitigar mediante el promediado de varias imágenes obtenidas con idénticas condiciones de lectura, aunque, en el campo de la dosimetría con película radiocrómica, se recomienda [26, 38] minimizar el número de escaneos consecutivos, debido al aumento de la temperatura de la cama del escáner y de la película radiocrómica sobre ella, que se traduce en errores de la estimación de dosis final. Para alcanzar el objetivo, demostramos que el protocolo eficiente de Lewis y col., inicialmente propuesto para compensar las variabilidades que afectan a la dosimetría con película mediante el empleo de un único escaneo, puede extenderse sin pérdida de exactitud al uso de imágenes promediadas, mitigando el ruido temporal presente en la dosimetría. Además, mostramos como la mitigación de este ruido permite mejorar la tarea de verificación de los tratamientos y aumentar la resolución de trabajo.

Nuestro último objetivo, desarrollado en el capítulo 6, es la caracterización dosimétrica de los colimadores multilámina comúnmente empleados en la práctica clínica. Estos colimadores están formados por múltiples láminas u hojas, que pueden moverse independientemente para conformar la forma irregular del campo de tratamiento [63]. La transmisión de radiación cuando este colimador está cerrado presenta picos de transmisión coincidentes con las zonas de separación entre láminas adyacentes[64]. Para minimizar esta transmisión de radiación entre láminas adyacentes, los fabricantes suelen emplear el diseño de lengua y surco [65] o, como se conoce por su nombre en inglés, *tongue and groove*. Este diseño da lugar a diferencias en la deposición

de dosis según el tipo de láminas empleadas y puede tener influencia en la dosis administrada con multiláminas dinámicos. Así pues, proponemos nuevas pruebas para la caracterización dosimétrica de este efecto y mostramos las discrepancias que existen entre las dosis calculadas por los planificadores y las medidas tanto con cámara como con película radiocrómica.

Bibliografía del capítulo 1

[1] W. L. McLaughlin, J. C. Humphreys, D. Hocken y W. J. Chappas. «Radiochromic dosimetry for validation and commissioning of industrial radiation processes». En: *Radiation Physics and Chemistry* 31 (1988), pp. 505-514.

[2] International Atomic Energy Agency. *Product quality control, irradiation and shipping procedures for mass-reared tephritid fruit flies for sterile insect release programmes (INIS-XA–426)*. Inf. téc. Vienna, 1999.

[3] S. Devic. «Radiochromic film dosimetry: Past, present, and future». En: *Physica Medica* 27 (2011), pp. 122-134.

[4] S. Devic, N. Tomic y D. Lewis. «Reference radiochromic film dosimetry: Review of technical aspects». En: *Physica Medica* 32 (2016), pp. 541-556.

[5] A. González-López, J. A. Vera-Sánchez y J. D. Lago-Martín. «Small fields measurements with radiochromic films». En: *Journal of Medical Physics* 40.2 (2015), pp. 61-67.

[6] J. E. Morales, M. Butson, S. B. Crowe, R. Hill y J. V. Trapp. «An experimental extrapolation technique using the Gafchromic EBT3 film for relative output factor measurements in small x-ray fields». En: *Medical Physics* 43.8 (2016), pp. 4687-4692.

[7] D. A. Low, P. Parikh, J. F. Dempsey, S. Wahab y S. Huq. «Ionization chamber volume averaging effects in dynamic intensity modulated radiation therapy beams». En: *Medical Physics* 30.7 (2003), pp. 1706-1711.

[8] W. U. Laub y T. Wong. «The volume effect of detectors in the dosimetry of small fields used in IMRT». En: *Medical Physics* 30.3 (2003), pp. 341-347.

[9] K. Y. Lee, K. K. L. Fung y C. S. Kwok. «Application of high-resolution radiochromic film dosimetry in verifying a small-field stereotactic radiosurgery plan». En: *Applied Radiation and isotopes* 64 (2006), pp. 934-939.

[10] Y. H. Lin y col. «Split-VMAT technique to control the expiratory breath-hold time in liver stereotactic body radiation therapy». En: *Physica Medica* 40 (2017), pp. 17-23.

[11] C. C. Ling, P. Zhang, Y. Archambault, J. Bocanek, G. Tang y T. LoSasso. «Commissioning and quality assurance of Rapidarc Radiotherapy delyvery system». En: *International Journal of Radiation Oncology Biology Physics* 72.2 (2008), pp. 575-581.

[12] L. Marrazzo, M. Zani, S. Pallotta, C. Arilli, M. Casati, A. Compagnucci, C. Talamonti y M. Bucciolini. «GafChromic® EBT3 films for patient specific IMRT QA using a multichannel approach». En: *Physica Medica* 31 (2015), pp. 1035-1042.

[13] F. M. Khan y J. P. Gibbons. *Khan's the physics of radiation therapy.* 5.ª ed. Wolters Kluwer, 2014.

[14] A. L. Palmer, A. Nisbet y D. Bradley. «Verification of high dose rate brachytherapy dose distributions with EBT3 Gafchromic film quality control techniques». En: *Physics in medicine & biology* 58.3 (2013), pp. 497-511.

[15] M. Hermida-López y L. Brualla. «Absorbed dose distributions from ophthalmic 106Ru/106Rh plaques measured in water with radiochromic film». En: *Medical Physics* (2018).

[16] S. Devic, J. Seuntjens, W. Abdel-Rahman, M. Evans, M. Olivares, E. B. Podgorsak, T. Vuong y C. G. Soares. «Accurate skin dose measurements using radiochromic film in clinical applications». En: *Medical Physics* 33.4 (2006), pp. 1116-1124.

[17] A. L. Palmer, S. M. Jafari, I. Mone y S. Muscat. «Evaluation and clinical implementation of in vivo dosimetry for kV radiotherapy using radiochromic film and micro-silica bead thermoluminescent detectors». En: *Physica Medica* 42 (2017), pp. 47-54.

[18] A. Bufacchi y col. «In vivo EBT radiochromic film dosimetry of electron beam for Total Skin Electron Therapy (TSET)». En: *Physica Medica* 23 (2007), pp. 67-72.

[19] T. Cheung, M. J. Butson y P. K. N. Yu. «Measurement of high energy x-ray beam penumbra with Gafchromic^{TM} EBT radiochromic film». En: *Medical Physics* 33.8 (2006), pp. 2912-2914.

[20] S. Spirydovich, L. Papiez, M. Langer, G. Sandison y V. Thai. «High density dental materials and radiotherapy planning: Comparison of the dose predictions using superposition algorithm and fluence map Monte Carlo method with radiochromic film measurements». En: *Radiotherapy and Oncology* 81.3 (2006), pp. 309-314.

[21] O. Rampado, S. D. Bianchi, A. Peruzzo Cornetto, V. Rossetti y R. Ropolo. «Radiochromic films for dental CT dosimetry: A feasibility study». En: *Physica Medica* 30 (2014), pp. 18-24.

[22] J. Greffier y col. «Assessment of peak skin dose in interventional cardiology: A comparison between Gafchromic film and dosimetric software em.dose». En: *Physica Medica* 38 (2017), pp. 16-22.

[23] B. C. Ferreira, M. C. Lopes y M. Capela. «Evaluation of an Epson flatbed scanner to read Gafchromic EBT films for radiation dosimetry». En: *Physics in Medicine & Biology* 54.4 (2009), pp. 1073-1085.

[24] S. Devic, J. Seuntjens, E. Sham, E. B. Podgorsak, C. R. Schmidtlein, A. S. Kirov y C. G. Soares. «Precise radiochromic film dosimetry using a flat-bed document scanner». En: *Medical Physics* 32.7 (2005), pp. 2245-2253.

[25] S. Devic, J. Seuntjens, G. H., E. B. Podgorsak, C. G. Soares, A. S. Kirov, I. Ali, J. F. Williamson y A. Elizondo. «Dosimetric properties of improved GafChromic films for seven different digitizers». En: *Medical Physics* 31.9 (2004), pp. 2392-2401.

[26] B. D. Lynch, J. Kozelka, M. K. Ranade, J. G. Li, W. E. Simon y J. F. Dempsey. «Important considerations for radiochromic film dosimetry with flatbed CCD scanners and EBT GAFCHROMIC® film». En: *Medical Physics* 33.12 (2006), pp. 4551-4556.

[27] A. A. Schoenfeld, D. Poppinga, D. Harder, K.-J. Doerner y B. Poppe. «The artefacts of radiochromic film dosimetry with flatbed scanners and their causation by light scattering from radiation-induced polymers». En: *Physics in Medicine & Biology* 59.13 (2014), p. 3575.

[28] M. Callens y col. «A spectroscopic study of the chromatic properties of Gafchromic^{TM} EBT3 films». En: *Medical Physics* 43.3 (2016), pp. 1156-1166.

[29] M. B. Callens, W. Crijns, T. Depuydt, K. Haustermans, F. Maes, E. D'Agsotino, M. Wevers, H. Pfeiffer y K. Van Den Abeele. «Modelling the dose dependence of the vis-absorption spectrum of EBT3 Gafchromic^{TM} films». En: *Medical Physics* 44.6 (2017), pp. 2532-2443.

[30] D. F. Swinehart. «The Beer-Lambert Law». En: *Journal of Chemical Education* 39.7 (1962), pp. 333-335.

[31] A. A. Schoenfeld, S. Wieker, D. Harder y B. Poppe. «Changes of the optical characteristics of radiochromic films in the transition from EBT3 to EBT-XD films». En: *Physics in Medicine & Biology* 61.14 (2016), p. 5426.

[32] T. Cheung, M. J. Butson y P. K. N. Yu. «Post-irradiation colouration of Gafchromic EBT radiochromic film». En: *Physics in Medicine & Biology* 50.20 (2005), N281.

[33] V. Casanova, M. Pasquino, G. Russo, P. Grosso, D. Cante, P. Sciacero, G. Girelli, M. R. La Porta y S. Tofani. «Dosimetric characterization and use of GAFCHROMIC EBT3 film for IMRT dose verification». En: *Journal of Applied Clinical Medical Physics* 14.2 (2013), pp. 158-171.

[34] K. Y. Lee, K. L. Fung y C. S. Kwok. «Development and initial evaluation of a spectral microdensitometer for analysing radiochromic films». En: *Physics in Medicine & Biology* 49.22 (2004), p. 5171.

[35] S. Saur y J. Frengen. «GafChromic EBT film dosimetry with flatbed CCD scanner: A novel background correction method and full dose uncertainty analysis». En: *Medical Physics* 35.7 (2008), pp. 3094-3101.

[36] I. Méndez, V. Hartman, R. Hudej, A. Strojnik y B. Casar. «Gafchromic EBT2 film dosimetry in reflection mode with a novel plan-based calibration method». En: *Medical Physics* 40.1 (2013), p. 011720.

[37] A. A. Schoenfeld, S. Wieker, D. Harder y B. Poppe. «The origin of the flatbed scanner artifacts in radiochromic film dosimetry—key experiments and theoretical descriptions». En: *Physics in Medicine & Biology* 61.21 (2016), p. 7704.

[38] D. Lewis y S. Devic. «Correcting scan-to-scan response variability for a radiochromic film-based reference dosimetry system». En: *Medical Physics* 42.10 (2015), pp. 5692-5701.

[39] A. González-López. «Useful optical density range in film dosimetry: limitations due to noise and saturation». En: *Physics in Medicine & Biology* 52.15 (2007), N321.

[40] N. J. Hangiandreou, T. J. O'Connor y J. P. Felmlee. «An evaluation of the signal and noise characteristics of four CCD-based film digitizers». En: *Medical Physics* 25.10 (1998), pp. 2020-2026.

[41] D. Poppinga, A. A. Schoenfeld, K. J. Doerner, O. Blanck, D. Harder y B. Poppe. «A new correction method serving to eliminate the parabola effect of flatbed scanners used in radiochromic film dosimetry». En: *Medical Physics* 41.2 (2014), p. 021707.

[42] L. Menegotti, A. Delana y A. Martignano. «Radiochromic film dosimetry with flatbed scanners: A fast and accurate method for dose calibration and uniformity correction with single film exposure». En: *Medical Physics* 35.7 (2008), pp. 3078-3085.

[43] D. F. Lewis y M. F. Chan. «Correcting lateral response artifacts from flatbed scanners for radiochormic film dosimetry». En: *Medical Physics* 42.1 (2016), pp. 416-429.

[44] M. P. Grams, J. M. Gustafson, M. L. Kenneth y L. E. Fong de los Santos. «Technical Note: Initial characterization of the new EBT-XD Gafchromic film». En: *Medical Physics* 42.10 (2015), pp. 5782-5786.

[45] D. F. Lewis y M. F. Chan. «Technical Note: On GAFChromic EBT-XD film and the lateral response artifact». En: *Medical Physics* 43.2 (2016), pp. 643-649.

[46] A. Niroomand-Rad y col. «Radiochromic film dosimetry: Recommendations of AAPM Radiation Therapy Committee Task Group 55». En: *Medical Physics* 25.11 (1998), pp. 2093-2115.

[47] G. Christ. «White polystyrene as a substitute for water in high energy photon dosimetry». En: *Medical Physics* 22.12 (1995), pp. 2097-2100.

[48] M. Martišíková, B. Ackermann y O. Jäkel. «Analysis of uncertainties in Gafchromic® EBT film dosimetry of photon beams». En: *Physics in Medicine & Biology* 53.24 (2008), pp. 7013-7027.

[49] D. Lewis, A. Micke, X. Yu y M. F. Chan. «An efficient protocol for radiochromic film dosimetry combining calibration and measurement in a single scan». En: *Medical Physics* 39.10 (2012), pp. 6339-6350.

[50] C. Ruiz-Morales, J. A. Vera-Sánchez y A. González-López. «On the recalibration process in radiochromic film dosimetry». En: *Physica Medica* 42 (2017), pp. 67-75.

[51] S. Devic, N. Tomic, C. G. Soares y E. B. Podgorsak. «Optimizing the dynamic range extension of a radiochromic film dosimetry system». En: *Medical Physics* 36.2 (2009), pp. 429-437.

[52] H. Chung, B. Lynch y S. Samant. «High-precission GAFCHROMIC EBT film-based absolute clinical dosimetry using a standard flatbed scanner without the use of a scanner non-uniformity correction». En: *Journal of applied clinical medical physics* 11.2 (2010), pp. 101-115.

[53] J. P. Chung, S. W. Oh, Y. M. Seong, K. J. Chun y H.-T. Chung. «An effective calibration technique for radiochromic films using a single-shot dose distribution in Gamma Knife®». En: *Physica Medica* 32 (2016), pp. 368-378.

[54] T. Kairn, T. Aland y J. Kenny. «Local heterogeneities in early batches of EBT2 film: a suggested solution». En: *Physics in Medicine & Biology* 55.15 (2010), p. L37.

[55] B. Hartmann, M. Martišíková y O. Jäkel. «Technical Note: Homogeneity of Gafchromic® EBT2 film». En: *Medical Physics* 37.4 (2010), pp. 1753-1756.

[56] International Specialty Products. «Gafchromic EBT2 self-developing film for radiotherapy». En: *ISP White Paper* (2010).

[57] A. Micke, D. F. Lewis y X. Yu. «Multichannel film dosimetry with nonuniformity correction». En: *Medical Physics* 38.5 (2011), pp. 2523-2534.

[58] R. R. Mayer, F. Ma, Y. Chen, R. I. Miller, A. Belard, J. McDonough y J. J. O'Connell. «Enhanced dosimetry procedures and assessment for EBT2 radiochromic film». En: *Medical Physics* 39.4 (2012), pp. 2147-2155.

[59] I. Méndez, P. Peterlin, R. Hudej, A. Strojnik y B. Casar. «On multichannel film dosimetry with channel-independent perturbations». En: *Medical Physics* 41.1 (2014), 011705-n/a.

[60] J. F. Pérez Azorín, L. I. Ramos García y J. M. Martí-Climent. «A method for multichannel dosimetry with EBT3 radiochromic films». En: *Medical Physics* 41.6 (2014), 062101-n/a.

[61] H. Bouchard, F. Lacroix, G. Beaudoin, J. F. Carrier y I. Kawrakow. «On the characterization and uncertainty analysis of radiochromic film dosimetry». En: *Medical Physics* 36.6 (2009), pp. 1931-1946.

[62] Joint Committe for Guides in Metrology. *Evaluation of measurement data – Guide to the expression of uncertainty in measurement (GUM 1995 with minor corrections)*. Inf. téc. 2008.

[63] T. LoSasso, C. Chui y C. Ling. «Physical and dosimetric aspects of a multileaf collimation system used in the dynamic mode for implementing intensity modulated radiotherapy.» En: *Medical Physics* 25.10 (1998), pp. 1919-1927.

[64] F. Lorenz, A. Nalichowski, F. Rosca, J. Kung, F. Wenz y P. Zygmanski. «Spatial dependence of MLC transmission in IMRT delivery.» En: *Physics in Medicine and Biology* 52.19 (2007), pp. 5985-99.

[65] J. Deng, T. Pawlicki, Y. Chen, J. Li, S. B. Jiang y C. M. Ma. «The MLC tongue-and-groove effect on IMRT dose distributions.» En: *Physics in Medicine & Biology* 46.4 (2001), pp. 1039-60.

Capítulo 2

Technical Note: Statistical dependences between channels in radiochromic film readings. Implications in multichannel dosimetry

Med Phys. 2016 May;43(5):2194

Technical Note: Statistical dependences between channels in radiochromic films readings. Implications in multichannel dosimetry

Antonio González López[1], Juan Antonio Vera Sánchez[2], Carmen Ruiz Morales[3]

[1] *Hospital Clínico Universitario Virgen de la Arrixaca, Ctra Madrid-Cartagena, El Palmar, Murcia 30120, Spain*
[2] *Servicio de Protección Radiológica y Física Médica, Hospital Universitari Sant Joan de Reus, Av. del Dr. Josep Laporte, Reus, Tarragona 43204, Spain*
[3] *Hospital IMED Elche, Max Planck No. 3, Elche, Alicante, 03203, Spain*

Purpose: This note studies the statistical relationships between color channels in radiochromic films readings with flatbed scanners. The same relationships are studied for noise. Finally, their implications for multichannel film dosimetry are discussed.

Methods: Radiochromic films exposed to wedged fields of $6MV$ energy were read in a flatbed scanner. The joint histograms of pairs of color channels were used to obtain the joint and conditional probability density functions between channels. Then, the conditional expectations and variances of one channel given another channel were obtained. Noise was extracted from film readings by means of a multiresolution analysis. Two different dose ranges were analyzed, the first one ranging from 112 cGy to 473 cGy and the second one from 52 cGy to 1290 cGy.

Results: For the smallest dose range, the conditional expectations of one channel given another channel can be approximated by linear functions, while the conditional variances are fairly constant. The slopes of the linear relationships between channels can be used to simplify the expression that estimates the dose by means of the multichannel method. The slopes of the linear relationships between each channel and the red one can also be interpreted as weights in the final contribution to dose estimation. However, for the largest dose range, the conditional expectations of one channel given another channel are no longer linear functions. Finally, noises in different channels were found to correlate weakly.

Conclusion: Signals present in different channels of radiochromic film readings show a strong statistical dependence. By contrast, noise correlates weakly between channels. For the smallest dose range analyzed, the linear behavior between the conditional expectation of one channel given another channel can be used to simplify calculations in multichannel film dosimetry.

2.1. Introduction

Use of radiochromic (RC) film has increased in radiation therapy and diagnostic imaging applications due to the ever increasing range of films available. Using color scanners provides a representation of the information that is redundant. In radiotherapy, multichannel dosimetry takes advantage of the triple output of color flatbed scanners and provides a more accurate and less noisy estimation of the radiation doses in an exposed film when compared to single channel dosimetry [1-3].

The spectral absorption of different RC films has been studied [4-6] and shows an increasing absorption along the whole wavelength range as dose increases. Also, the curve of spectral absorption has a complex shape, including several peaks. EBT films show two main peaks in absorption at 636 nm and 585 nm [5]. The range of wavelength response for EBT films was longer than for previous MD-55-2 Gafchromic films, which produces a lesser effect with wavelength peaks at 676 nm and 618 nm [7].

When using a CCD-based color scanner, different sensor elements (MOS capatitors) are used to create each pixel in a digitized image. A different color filter is interposed between film and each sensor element, giving rise to three different outputs or channels per pixel: red-green-blue (RGB). These sensor elements are affected by noise, and the statistical nature of noise makes it difficult to study the dependence of signal between channels.

In this study, the statistical dependences between channels in radiochromic film (RCF) readings by means of flatbed scanners are studied. Joint and conditional probability density functions (PDFs) are obtained empirically. The conditional expectation and variance between channels are then calculated. The statistical dependences between noise in different channels are also studied. Finally, their implications for multichannel film dosimetry are discussed, and the relationships found between channels are used to simplify the equations in multichannel film dosimetry.

2.2. Materials and methods

Five EBT2 films and five EBT3 films (Ashland Inc., Wayne, NJ) were irradiated in an Elekta Precise linac (Elekta Oncology Systems Ltd., Crawley, West Sussex, UK) with 6 MV x-ray beams. Source to film distance was set to 100 cm and films were placed at a depth of 2 cm in a PMMA phantom

of dimensions $30 \times 30 \times 15$ cm^3. The irradiation field size was set to 20×16 cm^2 at the isocenter and 800 Monitor Units of a wedged field were delivered. One monitor unit delivers a dose of 1 cGy at d_{max}, a SSD of 100 cm and an open field of size 10×10 cm^2. Dose in each exposed film ranged from 112 cGy to 473 cGy.

Twenty hours after irradiation films were read. The digitizer was an Epson 10000 XL (Epson America Inc., Long Beach, CA, USA), the spatial resolution was 72 dpi and a signal resolution of 48 bits (16 per channel) was selected. Films were placed in the center of the digitizer bed and no correction nor filters were applied during acquisition. The digitizer was powered on 30 min before reading and five readings were taken and discarded for warming purposes. Images were stored in TIFF format.

After reading, three matrices were obtained for each image, one per channel. A central ROI of 19×4 cm^2 was used for analysis. A narrow width of 4 cm was chosen to avoid the lateral artifact [1]. Figure 2.1 shows the RGB channels (I_r, I_g and I_b) for one of the EBT3 films analyzed.

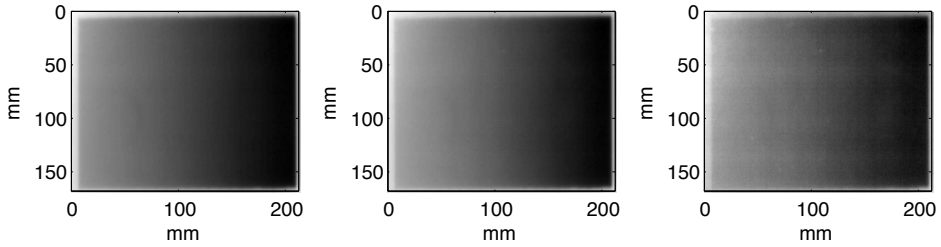

Figure 2.1: Red channel (left), green channel (center) and blue channel (right) from a digitized image of an EBT3 film irradiated with a wedged $6MV$ x-ray beam, with doses ranging from 112 cGy to 473 cGy.

Channel k reading I_k ($k \in \{r, g, b\}$) was affected of many disturbances [8]: systematic local variations and random perturbations. Random perturbations changed between different scans, while systematic local variations were consistent in time. Electronic noise and scanner instability can be classified as random, whereas thickness variations of the active layer and lateral artifact are systematic variations.

In this study, scanner instability was removed by scanning the whole film in a single session. Lateral artifact is also mitigated by restricting our analysis to a narrow strip along the scanning direction. Therefore, assuming that the Beer-Lambert law, valid for monochromatic light, is still valid for the range of frequencies detected by each color channel, the channel k reading depends

on film coordinates $\mathbf{r}$ and dose D through

$$I_k(\mathbf{r}, D) = I_{k,0} e^{-\lambda_k(D)(z(\mathbf{r}))} + n_k(\mathbf{r}), \tag{2.1}$$

where $I_{k,0}$ is the incident light intensity, $\lambda_k(D)$ is the dose dependent light attenuation coefficient, $z(\mathbf{r})$ stands for active layer thickness and $n_k(\mathbf{r})$ stands for random fluctuations or noise.

Channel independent perturbations are taken into account by spatial variations of active layer thickness $z(\mathbf{r})$, whereas differences in response between channels are modeled by different coefficients $\lambda_k(D)$ per channel. Finally, random perturbations $n_k(\mathbf{r})$ are assumed additive and channel-dependent.

Given two channels I_1 and I_2, the joint probability density function $f_{I_1,I_2}(I_1, I_2)$ can be estimated from the joint histogram $Hist(I_1, I_2)$ by

$$f_{I_1,I_2}(I_1, I_2) = \frac{Hist(I_1, I_2)}{N}, \tag{2.2}$$

where N is the number of pixels in each channel.

In order to obtain the conditional probability density of channel I_1 given channel I_2 $f_{I_1|I_2}(I_1|I_2)$, each column of the joint histogram $Hist(I_1, I_2)$ is divided by the sum of the elements in that column,

$$f_{I_1|I_2}(I_1|I_2) = \frac{Hist(I_1, I_2)}{\sum_{I_1} Hist(I_1, I_2)}, \tag{2.3}$$

The expectation of channel I_1 given I_2 can be calculated as

$$E[I_1|I_2] = \sum_{I_1} f_{I_1|I_2}(I_1|I_2) I_1, \tag{2.4}$$

and the conditional variance of channel I_1 given channel I_2 is obtained from

$$Var[I_1|I_2] = \sum_{I_1} f_{I_1|I_2}(I_1|I_2)(I_1 - E[I_1|I_2])^2 \tag{2.5}$$

Noise in each RC film and each channel was obtained from a multiresolution analysis [9] of the corresponding image. A multiresolution decomposes an image in frequency bands and the highest frequency band is, with a small fraction of exceptions, essentially noise [10]. The multiresolution analysis is carried out by means of a filter bank using Haar filters. Noise is obtained as the detail coefficients of the highest resolution and diagonal orientation of the decimated wavelet transform.

Lateral artifact and extended dose range were also investigated in this work. In order to study the effect of lateral artifact, the central ROIs of the film in figure 2.1 were extended to 19×15 cm^2. For extended dose range, two EBT3 films were irradiated with doses ranging from 52 cGy to 1290 cGy, and the joint probability density functions between channels were obtained.

2.3. Results

Figure 2.2 shows joint probability density functions $f_{I_r,I_g}(I_r, I_g)$, $f_{I_r,I_b}(I_r, I_b)$ and $f_{I_g,I_b}(I_g, I_b)$ for channels shown in figure 2.1. Similar results were found for the other EBT3 films and, regarding statistical dependences, EBT2 films showed similar joint PDFs.

Joint PDFs and conditional PDFs showed a strong correlation between channels. In all cases, there was a strong linear correlation with a relatively small variance in the conditional distribution.

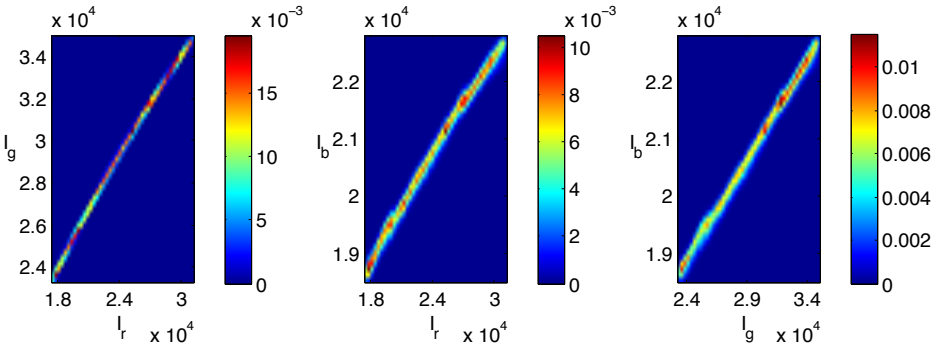

Figure 2.2: Joint probability density functions between color channels for channels shown in figure 2.1.

The linear relationship between channels is clear in figure 2.3, where the conditional expectations between channels are shown (plus signs). Linear fits between conditioning channels and conditioned expectations are also plotted (continuous lines).

Tables 2.1 and 2.2 show fitting coefficients and adjusted R^2 for linear fits of the conditional expectation. These tables show the lowest and highest values found in slope, y-intercept and adjusted R^2 for ten different films. Table 2.1 shows data for five EBT2 films, and table 2.2 shows data for five EBT3 films.

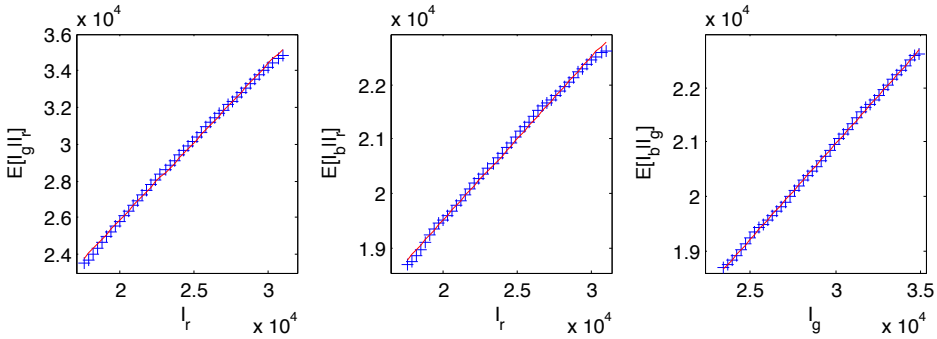

Figure 2.3: Conditional expectations between channels for EBT3 film shown in figure 2.1.

Table 2.1: Intervals containing fitting coefficients and adjusted R^2 for linear fits of the conditional expectation of five EBT2 films.

	$E[I_g\|I_r]$	$E[I_b\|I_r]$	$E[I_b\|I_g]$
slope	[0.883,0.889]	[0.305,0.312]	[0.343,0.350]
y-intercept	[9733,9841]	[15169,15297]	[11780,11986]
Adjusted R^2	[0.998,0.998]	[0.996,0.998]	[1.000,1.000]

In both EBT2 and EBT3 films, correlation between red and green channels is slightly better than between red and blue channels and, as tables 2.1 and 2.2 show, blue and green channels correlate better than blue and red channels.

Figure 2.4 presents the conditional variances between channels. These variances seem to be fairly constant, independent of the conditioning channel value.

Figure 2.5 shows the joint probability density function for noise in channels red, green and blue. A small statistical dependence can be seen between noise in different channels.

Table 2.2: Intervals containing fitting coefficients and adjusted R^2 for linear fits of the conditional expectation of five EBT3 films.

	$E[I_g\|I_r]$	$E[I_b\|I_r]$	$E[I_b\|I_g]$
slope	[0.843,0.852]	[0.298,0.305]	[0.351,0.355]
y-intercept	[8817,9014]	[13401,13540]	[10322,10459]
Adjusted R^2	[0.997,0.998]	[0.996,0.997]	[1.000,1.000]

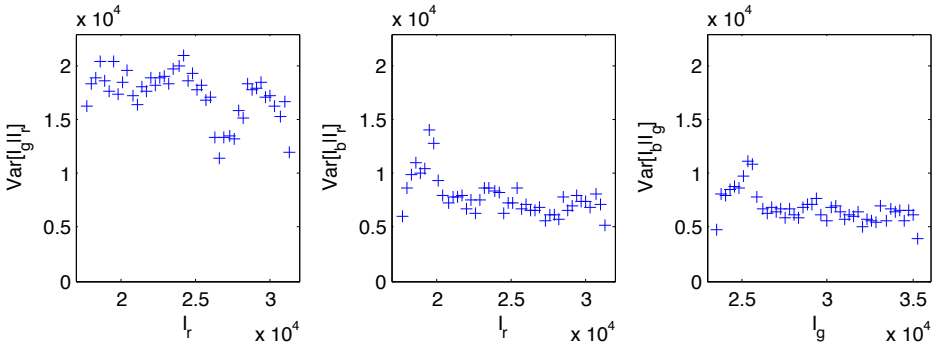

Figure 2.4: Conditional variances between channels for EBT3 film shown in figure 2.1. In order to minimize the lateral artifact, the size of the analyzed area was limited to a narrow band around the scanning direction (19×4 cm^2).

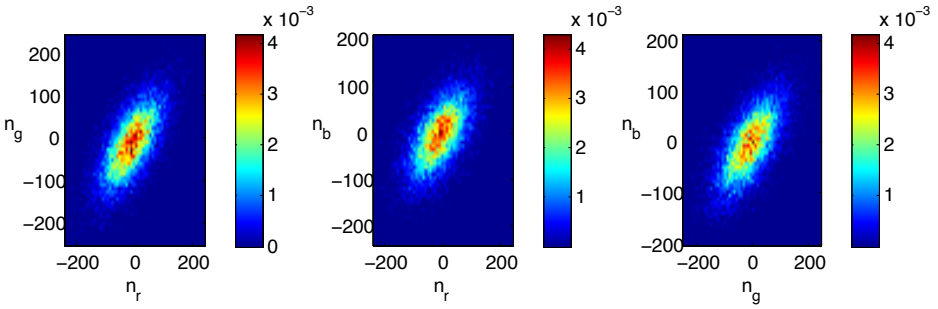

Figure 2.5: Joint probability density functions between noise in color channels for channels shown in figure 2.1.

In order to study the effect of lateral artifact, a wider area of the exposed film was analyzed. When the ROI size is extended from 19×4 cm^2 to 19×15 cm^2, the linear behavior for the expected value of one channel given another channel is still valid, but the conditional variance increases (figure 2.6).

Figure 2.7 shows joint probability density functions for pairs of channels when the dose range spans from 52 cGy to 1290 cGy. The curvature of the distribution is clearly visible. Therefore, the linear behavior shown in the lower dose range (figure 2.2) seems to be an approximation to a more complex functional relationship.

2.4. Discussion

Channels resulting from the reading of RC films present similarities along the whole range of intensity values (figure 2.1). These similarities are explicit

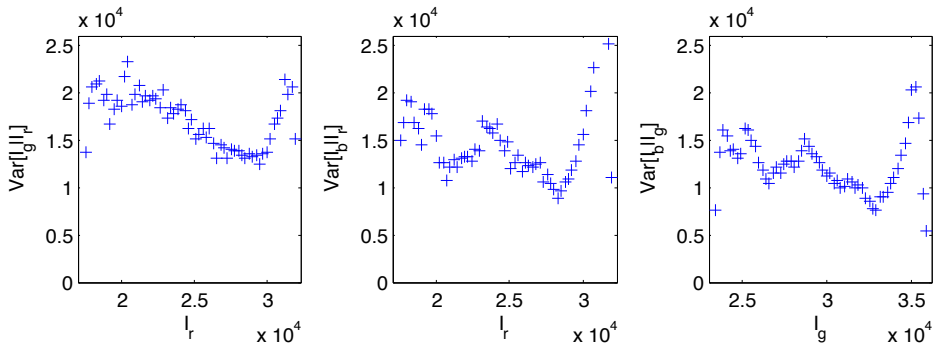

Figure 2.6: Conditional variances between channels for the film shown in figure 2.1. The size of the analyzed area was extended to 19×15 cm^2.

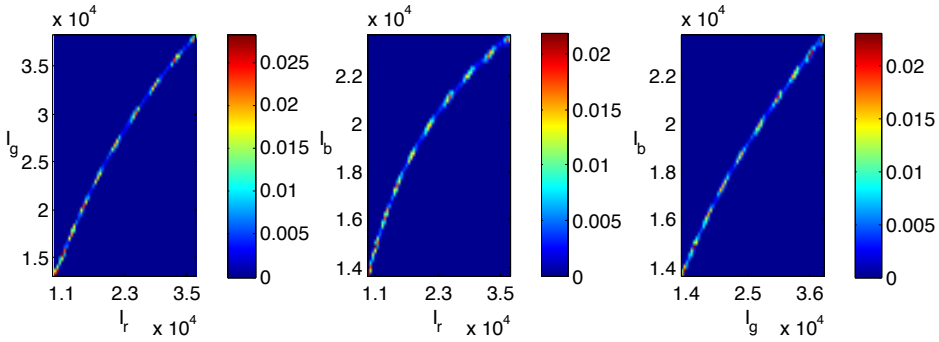

Figure 2.7: Joint probability density functions between color channels for a film irradiated with doses ranging between 52 cGy and 1290 cGy

in Figure 2.2, where the joint probability density functions for three pairs of channels (red-green, red-blue and green-blue) are shown. The distribution of intensity values shows a statistical dependence: the value of the dependent channel tends to increase with increasing values of the independent channel.

Figures 2.3 and 2.4 quantify these dependences in terms of conditional expected values and variances. Studying central trends as the conditional expectation minimizes the effect of the random term $n_k(\mathbf{r})$ in equation 2.1. Conditional expectations show a linear behaviour dominating the relationship between channels. For both films analyzed, similar dependences have been found. In fact, tables 2.1 and 2.2 show that the slopes of the straight lines describing the conditional expectations are quite similar.

The conditional variances between channels, presented in figure 2.4, are fairly constant, and the conditional variance of the blue channel given the red channel is similar to the conditional variance of the blue channel given the green one. The correlation between blue and green channels was also higher

than the correlation between blue and red channels (tables 2.1 and 2.2).

The statistical dependences studied for the signal present in film readings were also studied for noise. There is a weak correlation between noise in different channels (figure 2.5), much weaker than that found for signals (figure 2.2).

The statistical nature of the dependences between channels implies that CCD sensor elements producing the RGB signal are affected by different amounts of noise. On the other hand, the conditional expectation presented in figure 2.3 shows a functional dependency. In this way, the variabilities between the RGB channels are only due to noise, once the linear relationship between them is taken into account. Moreover, an RGB image is a redundant representation of information that partly justifies the good performance of multichannel dosimetry.

According to Mayer [2], the expected dose D derived from extracted red, green and blue channel doses (D_r, D_g and D_b) can be obtained by minimizing the cost functionΦ

$$\Phi(\Delta, D) = \sum_{k=r,g,b} (D_k + a_k\Delta - D)^2, \tag{2.6}$$

where D_k is the estimated dose from channel k, Δ is the disturbance or channel independent perturbation and a_k is the derivative

$$a_k = \frac{\partial D_k}{\partial I_k} \tag{2.7}$$

of the LUT for the kth channel.

The optimized dose can be expressed as [2]

$$D = \frac{D_{ave} - wt\frac{\sum_{k=r,g,b} D_k a_k}{\sum_{k=r,g,b} a_k}}{1 - wt}, \tag{2.8}$$

with

$$D_{ave} = \frac{1}{3}\sum_{k=r,g,b} D_k \tag{2.9}$$

and

$$wt = \frac{(\sum_{k=r,g,b} a_k)^2}{3\sum_{k=r,g,b} a_k^2} \tag{2.10}$$

Now, we can take advantage of the relationship between channels to simplify equation 2.6. Expressing $\frac{\partial D_k}{\partial I_k}$ as

$$\frac{\partial D_k}{\partial I_k} = \frac{\partial D_k}{\partial D_r}\frac{\partial D_r}{\partial I_r}\frac{\partial I_r}{\partial I_k}, \tag{2.11}$$

and taking into account that $\frac{\partial D_k}{\partial D_r} = 1$ and $c_k = \frac{\partial I_r}{\partial I_k}$ is constant, equation 2.8 becomes

$$D = \frac{D_{ave} - wt\frac{\sum_{k=r,g,b} D_k c_k}{\sum_{k=r,g,b} c_k}}{1 - wt}. \tag{2.12}$$

Furthermore, wt can be simplified to

$$wt = \frac{(\sum_{k=r,g,b} c_k)^2}{3\sum_{k=r,g,b} c_k^2} \tag{2.13}$$

and is constant too.

Equation 2.12 depends on dose estimations D_k and replaces the derivatives of the LUTs a_ks for constant values c_ks, simplifying the calculations. In fact, $c_r = 1$ and the values c_g and c_b are greater than 1 (inverses of slopes in tables 2.1 and 2.2) for EBT2 and EBT3 films.

Equation 2.12 shows a correction of the average dose D_{ave}. This correction involves every single channel estimation D_k, weighted by the slope c_k of the linear relationship between the red channel and channel k. As this slope increases, the correction increases and the final contribution of channel k to estimation D reduces. As tables 2.1 and 2.2 show, the slope for blue channel c_b is about 2,8 larger than the slope for the green channel c_g. So, the reduction in the final contribution of the blue channel to dose estimation D is 2,8 times larger than for the green channel.

In order to validate these theoretical results, dose calculations were carried out by five different methods: single-channel dosimetry (for each of the three channels), multichannel dosimetry and the simplified method given by equation 2.12. The dose was calculated for the film shown in figure 2.1, on a ROI of size 19×15 cm^2 and centered in the exposed film. The mean absolute difference between the multichannel method and the simplified method was 3.2 cGy, while the mean absolute differences between the multichannel method and the red, green and blue methods were 16.1 cGy, 17.1 cGy and 54.9 cGy respectively.

2.5. Conclusion

Scanning a radiochromic film with a color scanner produce three estimates of dose, one per channel. These estimates provide redundancy, and this can be used for denoising. These three estimates also allow accurate dose calculations by means of optimization processes like the multichannel method.

Reading the film is affected by two types of disturbances: channel independent perturbations, like spatial variations of the active layer thickness, and random perturbations like electronic noise.

In this study, we have investigated the effect of dose and independent perturbation on red, green and blue channels of RCF images obtained with a flatbed scanner. For this purpose we carried out a statistical analysis aimed at mitigating the effect of the random perturbation. Our findings show a linear relationship between channels when the dose range is small enough, and a more complex relationship when the dose range is extended. It was also investigated the effect of lateral artifact, which was found to increase the uncertainty in the relationship between channels.

Specifically, the statistical dependence found implies that the conditional expectation of one channel given another channel behaves as a smooth function, and this function approximates a linear function in restricted dose ranges. This study has shown the linear approximation to be valid in the dose range from 112 cGy to 473 cGy. The second result states that conditional variance between channels remains fairly constant. Last, noises in different channels are shown to correlate weakly.

Finally, the linear relationships between channels have been used to simplify the equations in multichannel dosimetry. Dose calculation obtained by the simplified method is shown to closely approximate that of the multichannel method.

[1] A. Micke, D. F. Lewis y X. Yu. «Multichannel film dosimetry with nonuniformity correction». En: *Medical Physics* 38.5 (2011), pp. 2523-2534.

[2] R. R. Mayer, F. Ma, Y. Chen, R. I. Miller, A. Belard, J. McDonough y J. J. O'Connell. «Enhanced dosimetry procedures and assessment for EBT2 radiochromic film». En: *Medical Physics* 39.4 (2012), pp. 2147-2155.

[3] D. Lewis, A. Micke, X. Yu y M. F. Chan. «An efficient protocol for radiochromic film dosimetry combining calibration and measurement in a single scan». En: *Medical Physics* 39.10 (2012), pp. 6339-6350.

[4] W. McLaughlin, J. Puhl, M. Al-Sheikhly, C. Christou, A. Miller, A. Kovács, L. Wojnarovits y D. Lewis. «Novel Radiochromic Films for Clinical Dosimetry». En: *Radiation Protection Dosimetry* 66.1-4 (1996), pp. 263-268.

[5] M. J. Butson y P. K. N. Cheung T. andYu. «Absorption spectra variations of EBT radiochromic film from radiation exposure». En: *Physics in Medicine & Biology* 50.13 (2005), N135.

[6] H. Alnawaf, T. Cheung, M. J. Butson y P. K. Yu. «Absorption spectra response of XRQA radiochromic film to x-ray radiation». En: *Radiation Measurements* 45.1 (2010), pp. 129-132.

[7] M. J. Butson, P. K. N. Yu, T. Cheung y P. Metcalfe. «Radiochromic film for medical radiation dosimetry». En: *Materials Science and Engineering: R: Reports* 41.3 (2003), pp. 61-120.

[8] I. Méndez, P. Peterlin, R. Hudej, A. Strojnik y B. Casar. «On multichannel film dosimetry with channel-independent perturbations». En: *Medical Physics* 41.1 (2014), 011705-n/a.

[9] S. Mallat. *A Wavelet Tour of Signal Processing: The Sparse way*. 3.ª ed. Academic Press, 2009.

[10] D. L. Donoho y I. M. Johnstone. «Ideal Spatial Adaptation by Wavelet Shrinkage». En: *Biometrika* 81.3 (1994), pp. 425-455.

Capítulo 3

Monte Carlo uncertainty of dose estimates in radiochromic film dosimetry with single-channel and multichannel algorithms

Phys Med. 2018 March;47:23-33

Monte Carlo uncertainty of dose estimates in radiochromic film dosimetry with single-channel and multichannel algorithms

Juan Antonio Vera Sánchez[1,2], Carmen Ruiz Morales[2],Antonio González López[3]

[1] *Hospital Universitari Sant Joan de Reus, Servicio de Física Médica. Reus (Tarragona), Spain*
[2] *PhD Programme in Physics and Space Science of the University of Granada. Granada, Spain*
[3] *Hospital Universitario Virgen de la Arrixaca. El Palmar (Murcia), Spain*

Purpose: To provide a multi-stage model to calculate uncertainty in radiochromic film dosimetry with Monte-Carlo techniques. This new approach is applied to single-channel and multichannel algorithms.

Material and methods: Two lots of Gafchromic EBT3 are exposed in two different Varian linacs. They are read with an EPSON V800 flatbed scanner. The Monte-Carlo techniques in uncertainty analysis provide a numerical representation of the probability density functions of the output magnitudes. From this numerical representation, traditional parameters of uncertainty analysis as the standard deviations and bias are calculated. Moreover, these numerical representations are used to investigate the shape of the probability density functions of the output magnitudes. Also, another calibration film is read in four EPSON scanners (two V800 and two 10000XL) and the uncertainty analysis is carried out with the four images.

Results: The dose estimates of single-channel and multichannel algorithms show a Gaussian behavior and low bias. The multichannel algorithms lead to less uncertainty in the final dose estimates when the EPSON V800 is employed as reading device. In the case of the EPSON 10000XL, the single-channel algorithms provide less uncertainty in the dose estimates for doses higher than four Gy.

Conclusion: A multi-stage model has been presented. With the aid of this model and the use of the Monte-Carlo techniques, the uncertainty of dose estimates for single-channel and multichannel algorithms are estimated. The application of the model together with Monte-Carlo techniques leads to a complete characterization of the uncertainties in radiochromic film dosimetry.

3.1. Introduction

The characteristics of radiochromic film (RCF) such as its near tissue equivalence, small dependence on both energy and dose rate and high spatial resolution [1] make RCF the choice in many dosimetry applications. In particular, these characteristics make RCF a very interesting dosimeter when the electronic equilibrium is lost or high resolution dosimetry is required. Small fields found in radiosurgery or SBRT, highly inhomogeneous fields found in IMRT or VMAT treatment verifications and high dose gradients of brachytherapy treatments are frequently measured with RCF [2-5].

The exposition of RCF to ionizing radiation produces a response, the darkening of the film. This response is usually read with flatbed color scanners [6, 7]. These devices produce three different color channels per reading, red-green-blue or RGB. In order to be able to convert film responses of a film lot to absorbed doses a calibration should be performed. Several protocols for the calibration of a RCF lot have been described in the bibliography [1, 8-16]. The aim of these protocols is to obtain sensitometric curves relating film responses in every channel and doses.

Once the calibration of a film lot has been performed, the film responses found in any irradiated film of the lot may be converted to a dose map. The single-channel algorithms obtain the doses with the application of the sensitometric curve to film responses of the selected channel [1, 10, 11, 14, 17]. The multichannel algorithms work with the film responses of the three available channels and the three sensitometric curves simultaneously to obtain the doses [13, 14]. Some advantages of the multichannel algorithms include the reduction of noise and the partial mitigation of the scanning lateral artifact.

The target of the dosimetric process with RCF is to obtain a dose estimate for every pixel of the evaluated film, exploding the high resolution of the dosimeter. However, every stage of the calibration procedure is affected by uncertainties. Moreover the final estimation of the dose map is carried out by means of the results of the calibration process and by employing the selected algorithm (single-channel or multichannel). In order to calculate the uncertainty of the final dose estimates, the uncertainties arising from the calibration procedure, the uncertainties of the evaluated film responses and how the selected algorithm manages all the uncertainties should be taken into account. Previous works have evaluated the uncertainty in dose estimates of RCF dosimetry with single-channel algorithms [1, 10, 11, 17, 18] and the law of propagation of the uncertaities [19]. However, the analysis and quan-

tification of the uncertainty in dose estimates when multichannel algorithms are employed is still an unsolved issue. In the case of these algorithms a complete uncertainty analysis should comprise the characterization of the film responses in the three reading channels and their correlations [20] as well as the particularities of the multichannel algorithms.

In this paper we present a multi-stage model for uncertainty analysis of the dose estimates in RCF dosimetry.The model is valid for single-channel and multichannel algorithms, so it is applied simultaneously to both kinds of algorithms. Based on this model, the probability density functions (PDFs) of the input magnitudes are characterized and they are propagated through the model with Monte-Carlo techniques. The resulting uncertainties of every stage of the model are calculated, presented and analyzed. In this way, the uncertainties of the dose estimates are obtained and compared for single-channel and multichannel algorithms. Finally, the implications of the scanner employed for the reading process are studied and their impact on the final uncertainty of the dose estimates is discussed.

3.2. Material and methods

3.2.1. Experimental measurements

Two lots of Gafchromic EBT3 films (Ashland Inc, Russell, USA) with serial numbers #04141403 and #11021501 were calibrated and analyzed in this work. One calibration film per lot was considered and these films were manipulated according to recommendations [21]. Every calibration film was divided in eight pieces of 20.4 cm x 2.9 cm. The pieces of the two calibration films were exposed with the same setup. They were placed at a deep of 10 cm in a slabbed equivalent water phantom (RW3) with a source to surface distance of 90 cm. The projection of the crosshair was marked in every piece for alignment purposes. The pieces were irradiated with beams of a nominal energy of 6 MV and a field size of 20 cm x 20 cm, with doses ranging from 0 to 10 Gy. The calibration film of the lot #04141403 was irradiated using a DHX Clinac (Varian, Palo Alto, USA), while the calibration film of the lot #11021501 was irradiated in a Varian Trilogy linac.

Prior to the irradiation of the pieces of the calibration films, the output of the linac was measured using the same setup that was employed for the irradiation of the film pieces. In the case of the DHX Clinac an A12 ionization

chamber (Standard Imaging, Middelton, USA) and a PC Electrometer (Sun Nuclear Corp., Melbourne, USA) were employed, while in the case of the Trilogy linac a PTW Farmer 30013 chamber and a PTW Webline Unidos electrometer (PTW, Freiburg, Germany) were used.

At least four hour post-irradiation of the film pieces, they were read in an EPSON V800 scanner (Seiko EPSON Corp., Nagano, Japan) in portrait orientation. In order to avoid the undesired inter-scan variability, all the pieces of the same calibration film were digitized together. The marks of the crosshair projection onto the pieces were aligned with the center of the bed of the digitizer to minimize the lateral scanning artifact. The images were acquired with all the corrections turned off and were saved in tiff format with a resolution of 72 dpi. The digitizer was switched on half and hour prior to the scanning session and seven open scans of the whole field of the bed were performed to warm up the system before the acquisition of the images of the calibration films. Finally, the images were loaded into Matlab (Mathworks, Massachusetts, USA) and analyzed with in-house software.

Additionally another calibration film from the lot #11021501 was irradiated in the DHX Clinac with doses ranging from 0 to 11 Gy. The exposition and the reading protocols for this film were the aforementioned protocols, except for the post-exposure time, higher than 48 hours. This film was read in four different scanners: two EPSON 10000XL and two EPSON V800. The aim of this procedure was to evaluate the influence of the reading devices in the final uncertainty analysis achieved with single-channel and multichannel algorithms.

3.2.2. Uncertainty analysis: from the law of propagation of uncertainty to the Monte-Carlo approach.

Traditionally the law of propagation of uncertainty is employed to obtain the combined uncertainty $u_c(y)$ of a magnitude y from the known uncertainties $u(x_i)$ of the magnitudes x_i $i = 1, ..., N$, with covariances $u(x_i, x_j)$ between the $x_i s$ magnitudes, and related to y by the expression $y = f(x_i)$. Thus, by employing equation 3.1 the combined uncertainty of the output magnitude y is obtained as the positive root of its variance $u_c^2(y)$:

$$u_c^2(y) = \sum_{i=1}^{N} (\frac{\partial f}{\partial x_i})^2 u^2(x_i) + 2 \sum_{i=1}^{N-1} \sum_{j=i+1}^{N} (\frac{\partial f}{\partial x_i})(\frac{\partial f}{\partial x_j}) u(x_i, x_j) \qquad (3.1)$$

With this approach, the uncertainty of the output magnitude may be expressed as the standard uncertainty, $u_c(y)$, or as a confidence interval by employing a proper coverage factor, as it is widely described in [19]. However, in certain circumstances this approach may lead to inappropriate results due to an inadequate representation of the linearity of the problem or a deviation from the Gaussian behaviour [22].

The Monte-Carlo approach [22-24] to uncertainty analysis is intended to deal with complex relationships between the input magnitudes and to take into account any nonlinearity present in the model. Also the correlation between the input magnitudes and the deviations from the Gaussian behaviour are contemplated in this approach. It is worth to mention that these Monte-Carlo methods do not realize a probabilistic calculation of the uncertainty. Instead, they are intended to propagate the PDFs of the input magnitudes throughout a previously established model to obtain a numerical realization of the output magnitude(s) PDF(s), as it is schematized in figure 3.1. From this output PDF, the uncertainty may be estimated as a standard deviation or a confidence interval [22, 24]. The model is intended to relate the input and the output magnitudes, including the equations or algorithms that lead to the calculation of the output magnitude(s) from the input magnitudes. For complex uncertainty evaluations a model composed by several stages may be employed [22, 24]. Every stage of the model may be independently analyzed, and, moreover, the numerical output of the firsts stages may be considered as the input for the next stages, and so, until the whole model is traveled, and, finally, the numerical realization of the output magnitude PDF is obtained. Previously to the application of the Monte-Carlo techniques to the proposed model, the PDFs of the input magnitudes should be investigated and properly characterized, including the correlations between them, in order to realize a correct sampling from these PDFs. For input magnitudes whose PDFs are unknown, the principle of maximum entropy should be applied [22, 25], and a specific PDF between all possible should be assigned.

The Monte-Carlo techniques for the uncertainty analysis are numerical methods, so special attention should be focused on the adequacy and numerical stability of the results. In this paper we follow the metodology introduced in references [22, 24]. When a scalar magnitude is considered as the output magnitude, firstly four independent simulations of at least ten thousand histories are carried out. The four independent realizations of the output magnitude PDF are checked to be numerically stable. If this condition is not satisfied, the number of independent simulations should be increased until the numerical stability is reached. Once the numerical stability is reached, all

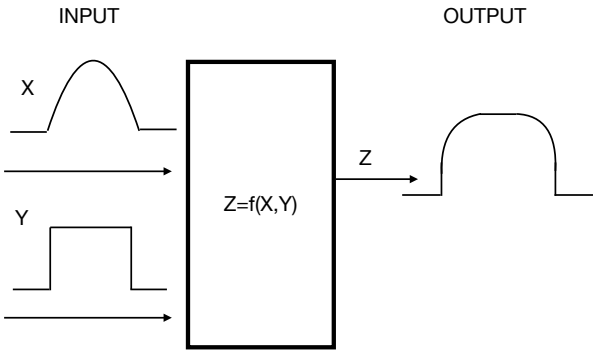

Figure 3.1: Scheme of the Monte-Carlo approach for uncertainty estimation.

the different simulations must be joined to obtain the numerical realization of the output magnitude PDF. From this output PDF, the magnitude and its uncertainty may be calculated as the mean and its standard deviation [22]. Moreover, with the information of the independent simulations, the numerical tolerance of the estimate of the magnitude and its uncertainty are obtained. When a vector magnitude is considered as the output, firstly, ten independent simulations of at least ten thousand histories must be carried out. In this case, the numerical stability of every component of the output vector magnitude and the correlations between all the components of the vector must be checked to be numerically stable. If the stability is not reached, the number of independent simulations should be increased until this numerical stability is reached. Once the stability is reached, as in the scalar case with the join of all the independent simulations, the estimates of the output components of the vector are calculated, the uncertainties of every component of the vector are obtained, and, finally the correlations between all the components of the vector are also determined [24]. As in the scalar case, from the information of the independent simulations, numerical tolerances are obtained for the component of the output magnitude, their uncertainties and the correlations between components of the vector.

3.2.3. Single-channel and multichannel algorithms in RCF dosimetry

In order to obtain dose estimates from every reading pixel value (PV) of the evaluated film in a particular channel, red, green or blue, the lot sensitometric curve should be known. It is assumed that it has been previously determined by exposing some film pieces to known doses and performing a nonlinear fit between the film responses obtained in the calibration film pieces and the absorbed doses to what these pieces were exposed. The sensitometric curve in a particular channel may be expressed as $y = f(x; a_i)$, where y represents the film responses values or the doses values and x the other magnitude and the $a_i s$ are the fit parameters. In this case, the single-channel dose estimates may be obtained by replacing the film responses in the former equation and obtaining the dose estimates for every pixel of the scanned image. In the next sections the details about the sensitometric curve and the nonlinear fit carried out in this work may be found. Previous works [1, 10, 11, 17, 18] have described the uncertainty analysis of this dosimetry process by employing the aforementioned law of propagation of uncertainties. In these works, the characterization of the film responses uncertainties in the considered channel are employed together with the uncertainties of the fit parameters and the sensitometric curve to provide a final uncertainty of the dose estimates obtained with the single-channel algorithms. In this paper, we analyze the single-channel RCF dosimetry also with the Monte-Carlo method and the multistage model described below, since this new approach may be also employed to provide a uncertainty analysis in this case.

The multichannel algorithms provide dose estimates by employing the three lot sensitometric curves and the film responses in the three channels simultaneously. With all these inputs, a cost function is optimized and a dose estimate is obtained for every pixel. Two different multichannel algorithms are employed in this work, the multichannel algorithm of Micke et al [14] and the multichannel algorithm of Mayer et al [13]. These two algorithms work by optimizing two different cost functions, although they provide very close results as it is described in [13]. Beside the different cost functions, the choice of the independent variable in the sensitometric curves is also different for both protocols. To the best of our knowledge the uncertainty analysis of the dose estimates when the multichannel algorithms are employed has not been resolved yet. In this case, the application of the law of propagation of the uncertainties may be hard due to the fact that the film responses as well as the sensitometric curves in the three channels should be considered, and also the film responses in the three channels are highly correlated. In addition,

due to the complexity of the algorithms and the lack of knowledge about the PDFs of the fit parameters, the law of propagation of uncertainties may not work properly. For these reasons, we propose a multistage model and a Monte-Carlo approach to provide a uncertainty analysis of the dose estimates with multichannel algorithms.

3.2.4. Multistage model for Monte-Carlo uncertainty analysis of RCF dosimetry

The uncertainty analysis of the RCF dosimetry is carried out with the multistage model, shown in Fig. 3.2. The input for the model are the data collected for the calibration procedure, film readings in the pieces and doses to what these pieces were exposed. As may be seen, the model is composed of four stages, three of them involve Monte-Carlo simulations, and the outputs of some stages are considered as inputs for another posterior stages. The different stages are widely described in the next sections and results from every stage are displayed.

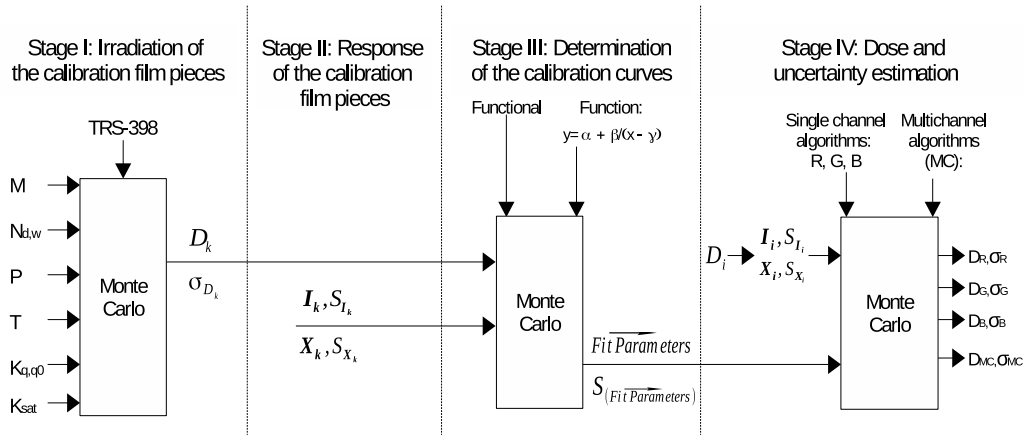

Figure 3.2: Description of the multistage model.

3.2.4.1. Stage I: Irradiation of the calibration film pieces

The objective of this stage is the calculation of the doses delivered to the calibration film pieces, $D_k \;\; k = 1, ..., 8$ and their uncertainties, $\sigma_{D_k} \;\; k = 1, ..., 8$. In accordance with the TRS-398 protocol [26], the absorbed dose in an homogeneous media delivered by an open beam may be obtained with the aid of a cylindrical chamber. From the charge collected by the electrometer M,

the calibration coefficient of the chamber-electrometer set, $N_{d,w}$, the pressure-temperature factor $K_{p,t}$, the beam quality factor, $K_{q,q0}$ and the factors of polarization and saturation of the chamber-electrometer set, K_{pol} and K_{sat}, correspondingly, the dose delivered in the absence of the air cavity of the chamber is obtained as:

$$D = M \cdot N_{d,w} \cdot K_{q,q0} \cdot K_{p,t} \cdot K_{pol} \cdot K_{sat} \tag{3.2}$$

By introducing the definition of the pressure-temperature factor, this equation 3.2 may be rewritten as:

$$D = M \cdot N_{d,w} \cdot K_{q,q0} \cdot K_{pol} \cdot K_{sat} \cdot \frac{T/P}{T_0/P_0} \tag{3.3}$$

From this equation 3.3, Monte-Carlo simulations may be carried out to obtain the numerical realizations of the dose output PDFs. The output magnitudes of this stage are the absorbed doses to what the calibration film pieces were exposed and their PDFs. As they are scalar magnitudes, the considerations formerly presented about the determination of a scalar mangnitude PDF and its numerical stability should be taken into consideration. The Monte-Carlo simulations are carried out to obtain the numerical realizations of the PDFs of everyone of the eight calibration doses levels. It is worth to mention that a dose uncertainty corresponding to a exposition of 5 cGy was assigned to the unexposed piece. According to reference [22], the doses are calculated as the mean of the output PDFs, and the uncertainties are calculated as the standard deviations of these output PDFs. Moreover, the shapes of the PDFs may be investigated from their numerical realization.

In order to carry out the Monte-Carlo simulations, the PDFs of the input magnitudes in equation 3.3 should be properly characterized. They are considered to be independent of each others. The collected charge, M, is obtained from five independent expositions, so a sample mean and a sample standard deviation are calculated from these five values. By one hand, following the maximum entropy principle [22, 25], when a sample mean and a sample standard deviation are available, a Gaussian distribution should be assigned. On the other hand, as the expectation and the standard deviation are unknown, a t-distribution should be employed to properly draw the collected charge. The pressure and the temperature are read from the scales of the mercury devices. In this case, the maximum entropy principle is applied by assigning uniform distributions to these magnitudes. The width of the distributions are

equal to the separation between the divisions of the scales and the center of these distributions are the readings. For magnitudes that are obtained from a calibration certificate a Gaussian distribution should be assigned [22].Thus, the PDF of the calibration factor, $N_{d,w}$, is drawn from a normal distribution, whose mean and standard deviation are taken from the calibration certificate. The same consideration is held for the value and the uncertainty of the beam quality factor, $K_{q,q0}$, that are obtained from the reference [26]. The saturation factor is also sampled from a Gaussian distribution with the uncertainty estimated for every camera from the two potentials method [26]. This factor is found to have a low relative weight as may be seen in [27]. Finally, the measurements are carried out with the same polarity and voltage as those used in the calibration certificate, so the polarity factor is not considered to add uncertainty.

3.2.4.2. Stage II: Response of the calibration film pieces

In this stage, the film responses to dose expositions are characterized. The film responses are evaluated using symmetric ROIs of 2 cm x 2 cm around the intersection of the crosshair projections onto the film pieces. The film responses may be examined as raw pixel values of every channel, $I_C \quad C = R, G, B$ or using the normalized channel X values: $X_C = \frac{I_C}{65535} \quad C = R, G, B$. As may be seen, the channel X values are just a normalization of the raw pixel values, so, they follow the same distribution than the raw pixel values, with the corresponding normalized parameters.

As it was demonstrated in a previous work [20], the film responses of the three different channels are highly correlated. So, in every ROI, the film responses are considered as a vector magnitude whose components are the three color responses $\mathbf{I_j} = (I_{R_j}, I_{G_j}, I_{B_j}) \quad j = 1, 2, ..., N$, where N is the number of pixels in the ROI. In this work eight calibration film pieces were considered, so the eight film responses were characterized. The characterization of every film piece response is based on the determination of the statistical parameters of the pixels in the ROI. In every ROI, the sample means of the vector whose components are the pixel values $\hat{\mathbf{I}}_\mathbf{k} \quad k = 1, .., 8$ and the sample covariance matrix $S_k \quad k = 1, .., 8$ were calculated according to reference [24]. From the sample covariance matrix, the uncertainties of every film response in every channel, $\sigma_{I_{C,K}} \quad C = R, G, B \quad k = 1, ..., 8$ and the sample correlation matrix, $R_k \quad k = 1, ..., 8$, between the three channel film responses may be also obtained.

Taking into account the sample data, i. e. the data of every ROI, the

distributions of the film piece responses may be sampled via numerical or empirical methods. In this work, we decided to use normal probability plots to investigate the shape of the distributions in every channel of the film responses, and considering the results of section 3.3.2, we assign multivariate Gaussian distributions to film responses in every of the eight dose levels. Again, the expectation and the covariance matrix are unknown, so multivariate t-distributions should be employed to make correct draws of the film responses.

3.2.4.3. Stage III: Determination of the calibration curves

In this work, we employ a rational function previously defined in references [14, 28] to relate film responses in the calibration pieces and doses:

$$y = \alpha + \frac{\beta}{x - \gamma} \tag{3.4}$$

This fitting function works properly for every channel in the analyzed dose range and it may be easily inverted. So this fitting function may be employed to examine differences introduced by the election of the independent variable, i. e. film response or dose.

Once the fitting function is chosen, the fit is carried out by minimizing a selected functional. In this work, we choose the so-called Total Variance (TV) functional, that has been proposed to carry out fits when both variables have uncertainties [29]. The definition of the functional as it was applied in every color channel, is:

$$TV_C = \sum_{k=1}^{N} (\frac{y_{C,k} - I_{C,k}}{\sigma_{I_{C,k}}})^2 + (\frac{x_{C,k} - D_k}{\sigma_{D_k}})^2 \quad C = R, G, B \tag{3.5}$$

This functional should be minimized with every channel data to find the channel fit parameters α_C, β_C and $\gamma_C \quad C = R, G, B$. In our case the sum has eight terms, one per calibration film piece. The values $(x_{C,k}, y_{C,k}) \quad C = R, G, B \quad k = 1, ..., 8$ are points of the channel calibration curve related by the equation 3.4. It should be mentioned that minimizing the TV functional is a complicated task that involve numerical methods [29]. In this work we employ the grid search method [23] and the simplex method [30], though no difference was found between both methods.

Once the fit parameters of the calibration curves have been calculated for every channel, the uncertainties of these fit parameters should be also determined. To take into account the uncertainties of the two magnitudes in the fit, it has been proposed in reference [24] to consider the fit parameters as components of a vector and to carry out Monte-Carlo simulations to obtain the numerical realization of the vector PDF. In the former stages, the PDFs of the doses delivered to the calibration film pieces and the PDFs of the film responses in these pieces were determined. Thus, according to these known PDFs, independent draws of the doses and the film responses may be carried out for each of the levels of the calibration and with these sampled values the fit parameters may be calculated, completing a history of one of the simulations. It should be mentioned that every draw of the film responses produces sampled values for the three color channels, as the film responses are considered as components of a vector. So, simultaneously for the eight levels of the calibration, the doses and the three channel responses are obtained and the determination of the fit parameters in the three channels may be accomplished. The fit parameters are considered as the components of a vector so the considerations previously described about the number of simulations and their numerical stability for this kind of magnitude must be taken into account. The output of this stage are the fit parameters of every channel and their PDFs.

3.2.4.4. Stage IV: Dose and uncertainty estimations

This final stage is expected to provide the dose estimates, their uncertainties and their bias over the whole calibration dose range, independently of the algorithm employed to convert film responses to doses. The film responses and the fit parameters are the input to the algorithm employed to convert film responses to doses. At this point, it should be mentioned that to carry out a proper characterization of the dose estimates, the film responses and their uncertainties, and the fit parameters and their uncertainties should be considered as independent sources of uncertainty since, in RCF dosimetry, the results of the calibration procedure are applied to different films of the same lot [13, 14]. So, with the participation of the film responses and their uncertainties, the fit parameters and their uncertainties, and the algorithm employed to convert film responses to doses, Monte-Carlo simulations may be carried out with the correct sampling of the input magnitudes to obtain the final dose estimates PDFs. Finally, from these PDFs, the uncertainties and the bias of the final dose estimates are calculated.

In the previous stages, a complete determination of the behavior of the multivariate PDFs of the film responses has been made for the eight calibration dose levels. This knowledge may be employed to obtain a suitable interpolation of the film response PDFs between the calibration dose levels. Thus, in this stage we consider simulated levels with doses ranging from 10 cGys until the maximum dose employed in the calibration in steps of 10 cGys. For every step dose, the values of the film responses in the three channels are obtained with the calibration curves and the corresponding multivariate PDFs of film responses are obtained by convex linear interpolation of the empirical multivariate PDFs of the two levels among which the simulated level is found. Once the film response multivariate PDF for a particular step dose is obtained, it may be sampled and with the numerical representation of the fit parameters PDFs of the previous stage, both magnitudes may be traveled through the algorithm employed to convert film responses to dose. At this point it is worth to mention that the characteristics of the fit parameter PDFs, described in section 3.3.3, make it a complicated task to sample the fit parameters from a known equation. However this is not a problem since the numerical representation of the PDFs obtained in the previous stage may be considered as the input for this stage, as it is described in [24]. It also should be mentioned that the whole numerical characterizations of the fit parameter multivariate PDFs are taken into account, so ten simulations of ten thousand histories are carried out to obtain the numerical representations of the dose estimates PDFs. Finally, for every step dose, the behavior of the PDF, its uncertainty and its bias are calculated. The bias is obtained as the difference between the initial step dose considered and the mean of the output PDF. This procedure is applied to single-channel and multichannel algorithms simultaneously and the output PDFs for the dose estimates obtained with these algorithms are obtained.

3.3. Results

3.3.1. Stage I: Irradiation of the calibration film pieces

The PDFs of the calibration doses to what the film pieces of both lots were exposed show a Gaussian behavior.This was checked by means of normal probability plots for all the calibration dose levels. In Fig 3.3 normal plots of a dose level for every lot are shown. This result may be explained by the fact that the highest and dominant sources of uncertainties in equation 3.3 are the calibration coefficient and the beam quality factor, that are characterized

by a Gaussian behavior. Results for the two analyzed lots are very similar due to the fact that the calibration coefficients of both chamber-electrometer sets had very close relative uncertainties.

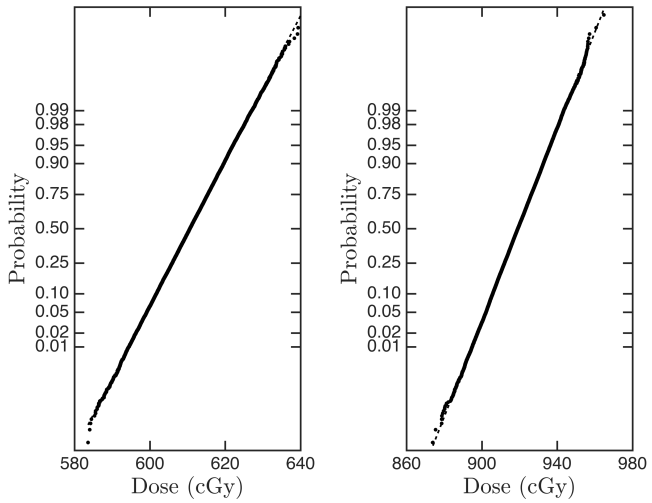

Figure 3.3: Normal probability plots of the dose PDFs: a) exposition of 611 cGy for the calibration of the lot #11021511 b) exposition of 919 cGy. for the calibration of the lot #04141403

The result of the Gaussian behavior of the PDFs of the calibration doses is important for the posterior stages. In particular in the third stage, in order to calculate the uncertainties of the fit parameters, the PDFs of the calibrations doses should be sampled and the Gaussian behavior simplifies the draws to be made.

3.3.2. Stage II: Response of the calibration film pieces

The film responses in every channel of all the evaluated pieces from the two lots, even the unexposed ones, are well described by a Gaussian behavior. In Fig. 3.4, the normal probability plots of the raw pixel values in the three channels of the experimental PDFs are shown for a calibration piece from the second lot. Also normal plots for a piece from the other lot are provided as supplementary material.

The standard deviations and the correlations of the film responses found for both lots are shown in table 3.1. As it may be seen, these statistical parameters show low variations through the whole dose calibration range.

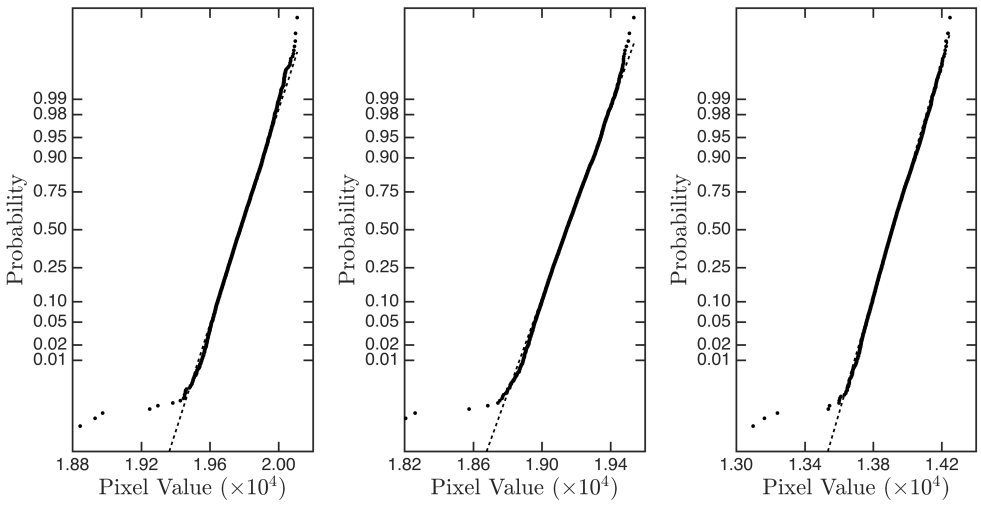

Figure 3.4: Film responses to the irradiation shown in Fig 3.3 (a)Red channel, (b)Green channel and (c)Blue channel from the lot #11021501

Table 3.1: Standard deviation intervals and correlation intervals found in the film responses of the calibration pieces.

		Lot #04141403	Lot #11021501
Standard Deviations	R	[90, 157]	[90, 133]
	G	[115, 142]	[108, 135]
	B	[103, 125]	[92, 110]
Correlations	RG	[0,87, 0,94]	[0,88, 0,92]
	RB	[0,69, 0,82]	[0,79, 0,85]
	GB	[0,84, 0,89]	[0,86, 0,92]

From the evaluation of figure 3.4, the film responses to dose exposition in the calibration pieces show a gaussian behaviour for every single channel. Also, taking into account the correlation values shown in table3.1 as well as in reference [20], the film responses of the three channels are highly correlated. So, the film responses of the calibration film pieces are well described by a multivariate Gaussian distribution, and they should be sampled from a multivariate t-distribution [24].

Moreover, it is worth to notice the low variability found in the standard deviations of the raw pixel values in every channel and in the correlations between the channels over the calibration range. By taking this result into account, the PDFs of the film responses that do not match a calibration level are obtained by a convex interpolation from two calibration film piece PDFs, one corresponding to an immediately lower calibration dose and the other to

an immediately higher calibration dose value.

3.3.3. Stage III: Determination of the calibration curves

Results of the values obtained from the Monte-Carlo simulations for the fit parameters and their uncertainties for both investigated lots are shown in table 3.2. As may be seen, the values of every parameter and its uncertainty are very close despite of the choice of the independent variable. This may be explained by the fact that the TV functional treats the two magnitudes involved in the fit procedure symmetrically.

Table 3.2: Values of the fit parameters and their uncertainties for the two lots analyzed.

		Lot #04141403		Lot #11021501	
		PV vs. D	D vs. PV	PV vs. D	D vs. PV
R	α (cGy)	$-339{,}4 \pm 9{,}9$	$-338{,}8 \pm 10{,}1$	$-353{,}7 \pm 9{,}4$	$-353{,}6 \pm 9{,}4$
	$\beta/10^7$ $(PV \cdot cGy)$	$1{,}0710 \pm 0{,}0390$	$1{,}0700 \pm 0{,}0400$	$1{,}2400 \pm 0{,}0415$	$1{,}2385 \pm 0{,}0415$
	γ (PV)	8690 ± 285	8700 ± 290	6910 ± 300	6910 ± 300
G	α (cGy)	$-546{,}0 \pm 21{,}5$	$-546{,}0 \pm 22{,}0$	$-617{,}4 \pm 22{,}7$	$-618{,}0 \pm 22{,}0$
	$\beta/10^7$ $(PV \cdot cGy)$	$1{,}901 \pm 0{,}100$	$1{,}9005 \pm 0{,}1010$	$2{,}3010 \pm 0{,}1170$	$2{,}304 \pm 0{,}114$
	γ (PV)	3165 ± 550	3160 ± 550	430 ± 590	410 ± 578
B	α (cGy)	-771 ± 85	-775 ± 71	-1119 ± 127	-1116 ± 99
	$\beta/10^7$ $(PV \cdot cGy)$	$0{,}95 \pm 0{,}15$	$0{,}950 \pm 0{,}135$	$1{,}610 \pm 0{,}280$	$1{,}600 \pm 0{,}230$
	γ (PV)	7470 ± 640	7420 ± 580	4660 ± 900	4680 ± 745

The PDFs of the fit parameters of the two lots behave in the same way. They present high correlations between the parameters corresponding to the same channel film responses, higher than 0.9 in absolute value. Moreover, the fit parameters of different channels are also found to have correlations higher than 0.5 in absolute value. This may be explained by the correlations of the film responses, the values of the three channels were sampled together from multivariate t-distributions, and then, the fits in the three channels were carried out. In this way, the correlations of the film responses were transferred to fit parameters.

It should be mentioned that some fit parameters, especially those of blue channel, do not have a Gaussian behavior, as may be seen in Fig. 3.5 for the blue channel fit parameters of the lot #11021501. The behavior is the same for the two investigated lots, and the normal probability plots of the blue channel fit parameters for the other lot as provided as supplementary material. Also, the normal probability plots of the fit parameters from red and green channels for the lot #11021501 are provided as supplementary

material.

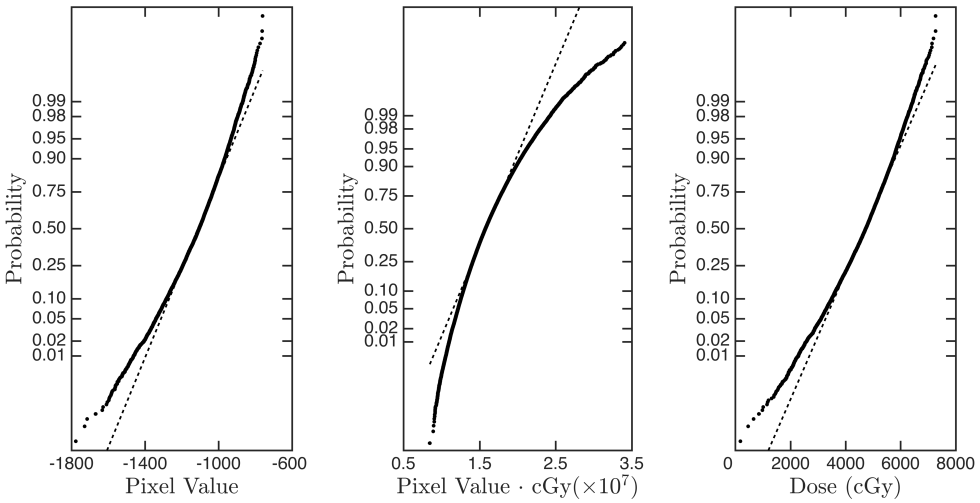

Figure 3.5: Normal probability plots of blue channel fit parameters: (a)Fit parameter α, (b)Fit parameter β and (c)Fit parameter γ for the lot #11021501

Finally, while in the case of the red and green channels the mean values of the fit parameter PDFs are in good accordance with the results of the TV functional optimization, some apparent discrepancies may be obtained between the optimum blue channel fit parameter values obtained by minimizing the TV functional and those shown in table3.2 obtained from the Monte-Carlo numerical realization of the fit parameter PDFs. However, once analyzed the normal probability plots of the fit parameter PDFs, it is clear that the skewness of the blue channel fit parameter PDFs is the cause of the differences. Also, since the blue channel fit parameter PDFs are not symmetrical, the mean values and the standard deviation of these PDFs should not be good parameters to describe these PDFs as reported in [22, 24]. Fortunately, this is not a problem for the Monte-Carlo approach that we are following, since the numerical realization of these PDFs are considered as numerical inputs for the next stages.

3.3.4. Stage IV: Dose and uncertainty estimation

The dose estimates of single-channel and multichannel algorithms show a Gaussian behavior in the considered dose range. In Fig. 3.6 the normal probability plots of the PDFs of the dose estimates obtained with the mul-

tichannel protocol of Micke et al are shown for the two lots. It is worth to mention that the results shown in Fig. 3.6 do not correspond to a dose level of the calibration, instead they correspond to a intermediate dose between two calibration levels. The Gaussian behavior of dose estimates is held through the whole dose range for both lots, and similar results are found when the dose is considered as the independent variable in the single-channel algorithms or in the multichannel protocol of Mayer et al.

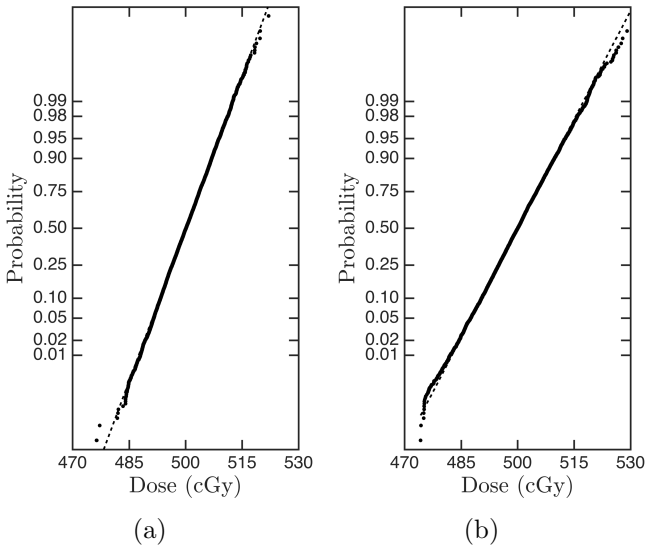

Figure 3.6: Normal probability plots of the PDFs of the dose estimates for 500 cGy with the multichannel protocol of Micke: a) lot #11021501 and b) #04141403.

Results of the bias and the uncertainties of the dose estimates for the two investigated lots are shown in Fig. 3.7. As in the preceding figure, the single-channel algorithms are those that consider the film response as the independent variable and the multichannel algorithm is the Micke et al one. As may be seen, the red and green single-channel algorithms and the multichannel algorithm have a very low bias, close to zero, while the blue single-channel algorithm give rise to the highest bias. The uncertainties of the blue channel dose estimates are also the highest, and this may be explained by the low dynamic range of the blue channel in the considered dose range. Although the uncertainties of the film responses in the three channels have very similar values, the low dynamic range of the blue channel responses makes the uncertainties of the blue channel to have a relative high weight in the final blue single-channel uncertainty estimates. No significative differences for the bias of the dose estimates of the two investigated lots are found. When the uncertainties of the dose estimates are considered, the multichannel algorithms

are found to provide lower uncertainties than the single-channel algorithms.

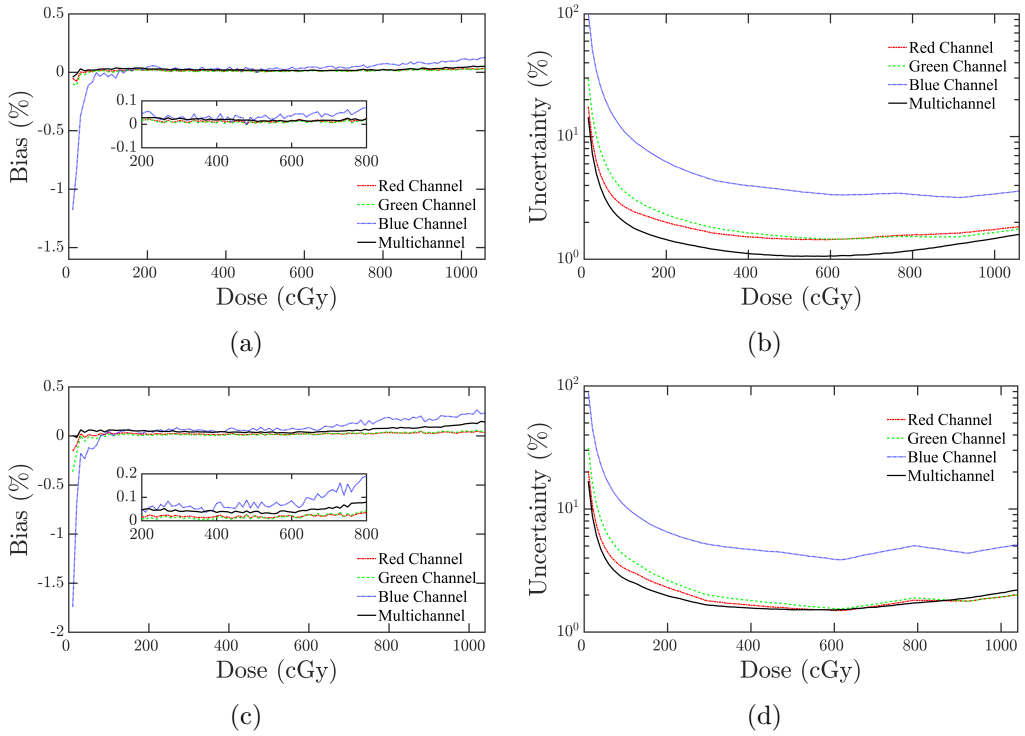

Figure 3.7: Results of the uncertainty analysis with the protocol of Micke: (a) Bias of dose estimates with lot #11021501, (b) Uncertainties (One sigma) of dose estimates with lot #11021501, (c) Bias of dose estimates with lot #04141403 and (d) Uncertainties (One sigma) of dose estimates with lot #04141403

Finally, the differences between the two investigated multichannel algorithms are presented in Fig. 3.8 for the two investigated lots. The slight differences found in table 3.2 between the PDFs of the fit parameters due to the choice of the independent variable explain the differences in the bias of the two investigated protocols. However, it may be seen that these differences have no significance due to the fact that both protocols provide very close uncertainties of the dose estimates and the bias of the dose estimates are also very low.

3.3.5. Effect of the reading device in the uncertainty of the dose estimates

Once the multistage model and the Monte-Carlo approach to analyze the uncertainty of the dose estimates obtained with multichannel algorithms ha-

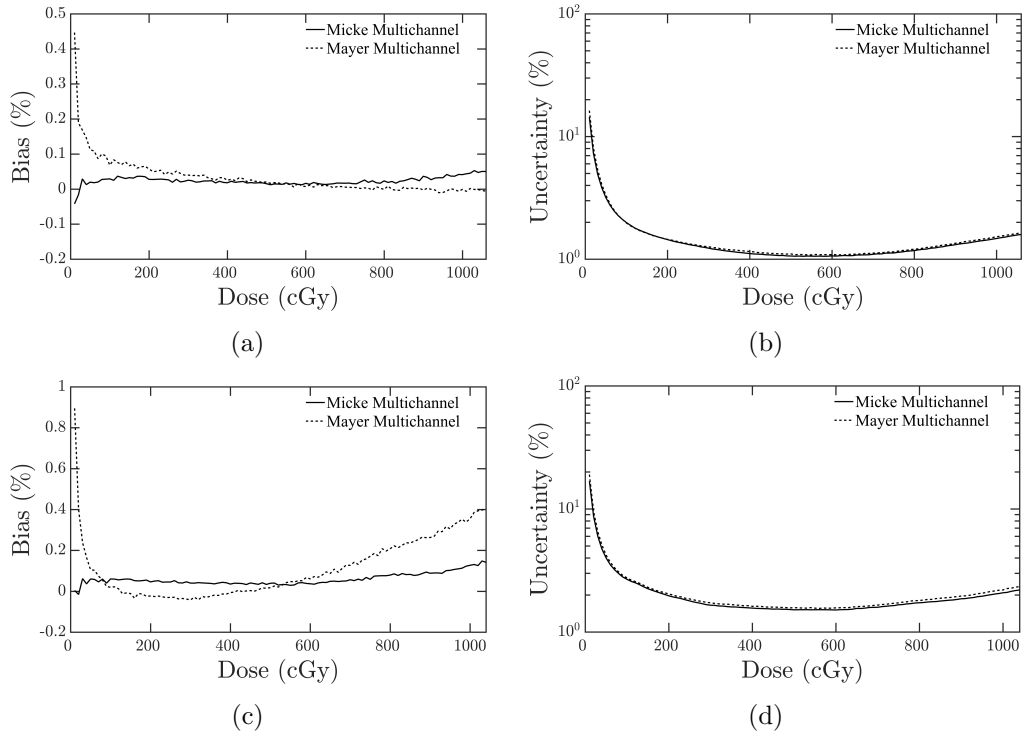

Figure 3.8: Comparison between the two multichannel protocols: (a)Bias and (b)Uncertainty (One sigma) with lot #11021501 and (c)Bias and (d)Uncertainty (One sigma) with lot #04141403

ve been developed, we apply this methodology to the same calibration film read in four different EPSON scanners (two V800 and two 10000XL). The multichannel of Lewis et al and the single-channel algorithms are considered. From the results of the previous section, it has been shown that the multichannel algorithms provide dose estimates with lower uncertainties when the EPSON V800 is employed as the reading device. As it may be seen in the next figure, in the case of the EPSON 1000XL, the multichannel algorithm provide doses estimates with lower uncertainties than the single channel dose estimates in the range 0 to 4 Gy. This result has been also found with a calibration film from the lot #01171702 read in two EPSON scanners, a 1000XL and a V800 (results not shown), and this is a point to be discussed.

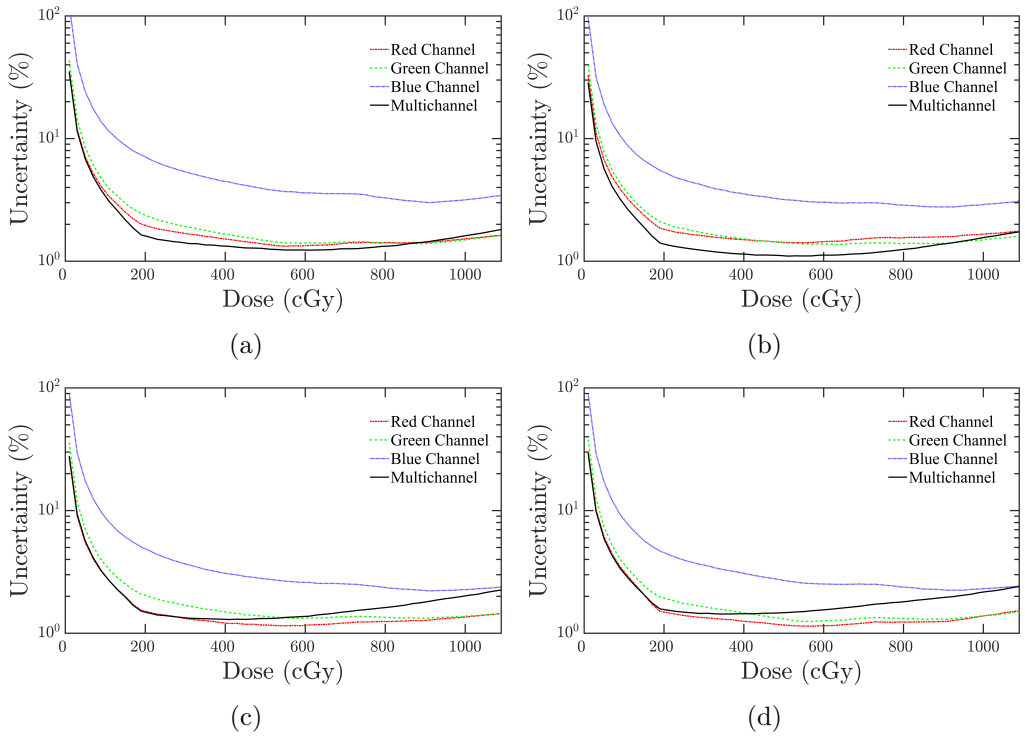

Figure 3.9: Uncertainty of the same lot calibration film read in four EPSON scanners: a) Scanner EPSON V800 #1 b) Scanner EPSON V800 #2 b c) Scanner EPSON 10000XL #1 and d) Scanner EPSON 10000XL #2

3.4. Discussion

In the context of RCF dosimetry, the law of propagation of uncertanties has been applied the to single-channel algorithms [1, 11, 17, 18]. In order to accomplish uncertainty analysis of RCF dosimetry we propose a new multistage model together with the use of the Monte-Carlo techniques. As in the case of the previous efforts, the proposed multistage model works with only two input magnitudes: the doses to what the calibration film pieces were exposed and the film responses obtained in these film pieces. In the case of the new multistage model, a deeper characterization of the input magnitudes is carried out. This effort provides a better understanding of the magnitudes involved in the dosimetric process with RCF, especially of the film responses. From the results of this characterization, the input PDFs are propagated trough the model with Monte-Carlo techniques to obtain the final numerical realization of the output dose PDFs. These Monte-Carlo calculations provide numerical results of every stage of the process and also allow to examine the

uncertainties arising in every stage. Another advantage of the new approach with respect to previous efforts, is that a complete uncertainty analysis, including calculation of the uncertainty, bias and description of the output PDF may be achieved for the dose estimates in RCF dosimetry.

The multistage model and the Monte-Carlo approach to the uncertainty analysis shown in this work are straightforward applied to single-channel and multichannel algorithms. In this way, the uncertainty analyses of the single-channel and the multi-channel algorithms are simultaneously computed. By one hand, despite the different uncertainty sources and their different PDFs in equation 3.3, the PDFs of the calibration doses to what the film pieces were exposed show a Gaussian behavior as shown in figure 3.4. On the other hand, the film responses characterization should take into account the correlations between the film responses in the three channels together with the Gaussian behavior shown in figure 3.5. Thus the film responses in the three channels are described by a Gaussian multivariate distribution. In this way, the film responses in the calibration film pieces and the absorbed doses to what they were exposed may be properly drawn in a simple way for the next stages.

In a previous work [18], the choice of the independent variable has been pointed out as a possible cause of bias in the dose estimates of RCF dosimetry. Also in the work of Ramos et al. [12] it has been shown how the consideration of the uncertainties in both variables, film responses and doses, lead to an improvement in the characterization of the sensitometric curves. It should be mentioned that both references work with single channel dose estimates. In this work, we have chosen to perform the fit relating doses and film responses by minimizing the total variance functional that take into account the uncertainties in both variables. In this way, as may be seen in the numerical values of the table 3.2, the fit parameters and their uncertainties show very close values regardless of the independent variable choice.

The uncertainty characterization of the fit parameters in non-linear least squares fitting has been treated in previous works [23, 31] and it is recommended the employment of the Monte-Carlo techniques due to the deviations from the Gaussian behaviour. In the case of RCF dosimetry, the characterization of the fit parameter PDFs should take into account the particularities of the reading process. Once the calibration film is read, for every pixel in the image three reading values are obtained -one per channel, RGB- and these values are not independent of each others, instead they are highly correlated [20]. The correlation in the film responses is transmitted to the fit parameters, even for fit parameters from different color channels, as described in section 3.3.3. Also, as may be seen in figure 3.5, the PDFs of the blue

channel fit parameters deviate from the Gaussian behavior. Thus the characterization of the fit parameter PDFs by employing a known distribution or a experimental characterization that takes into account all the aforementioned characteristics may be a complicated task. In our case, the numerical realizations of the fit parameter PDFs are straightforward considered as numerical input for the next stage. In this way, the lack of Gaussian behavior, the correlations between the fit parameters and other possible particularities are taking into account. So, this may be regarded as one of the advantages of the Monte-Carlo approach to uncertainty analysis, the possibility for designing multistage models where the output of one stage is the input for another stage, gives rise to a simple way of dealing with complicated intermediate PDFs.

The uncertainty characterization of the dose estimates with multichannel algorithms in section 3.3.4 shows Gaussian behavior and low bias for the dose estimates, and no relevant differences are found between the algorithms of Mayer et al. and Micke et al. Also, lower uncertainties are achieved with the use of the multichannel algorithms and the EPSON V800 reading device. For the single-channel algorithms, the blue channel give rise to the higher uncertainties, since this channel is the less sensitive to dose exposition and presents the lower dynamic range in the film responses. However, as may be seen in section 3.3.5, the use of the multichannel algorithms with the EPSON 10000XL give rise to dose estimates with higher uncertainties than the single-channel dose estimates, especially for dose expositions higher than 4 Gy. This fact may be explained by the different correlation values obtained in the film responses with both models of scanners. The scanners of the same model give rise to very close uncertainty for the dose estimates, slighty differences are found with different lot films. So, the differences in the uncertainty analysis of the dose estimates may be attributed to the influence of the reading device model and in particular to the different film response correlations between channels.

3.5. Conclusion

A new multi-stage model to compute dose estimates bias and uncertainties in RCF dosimetry has been proposed. This model may also be employed with multichannel algorithms. A complete characterization of the PDFs of the input variables, doses to what the film pieces were exposed and film responses has been carried out. The application of the Monte-Carlo based

uncertainty estimation approach together with the multi-stage model has lead to a complete characterization of the uncertainties in RCF dosimetry with single-channel and multichannel algorithms. The choice of the Monte-Carlo approach is highly recommended to compute uncertainties in complex models as is the case of RCF dosimetry. Finally, the influence of the reading device model in the final uncertainty of the dose estimates with multichannel algorithms has been shown.

[1] S. Devic, N. Tomic y D. Lewis. «Reference radiochromic film dosimetry: Review of technical aspects». En: *Physica Medica* 32 (2016), pp. 541-556.

[2] R. Ramani, A. W. Lightstone, D. L. D. Mason y P. F. O'Brien. «The use of radiochromic film in treatment verification of dynamic stereotactic radiosurgery». En: *Medical Physics* 21.3 (1994), pp. 389-392.

[3] J. A. Vera-Sánchez, C. Ruiz-Morales y A. González-López. «Technical Note: Characterization of noise and digitizer response variability in radiochromic film dosimetry. Impact on treatment verification». En: *Physica Medica* 32.9 (2016), pp. 1167-1176.

[4] A. L. Palmer, A. Nisbet y D. Bradley. «Verification of high dose rate brachytherapy dose distributions with EBT3 Gafchromic film quality control techniques». En: *Physics in medicine & biology* 58.3 (2013), pp. 497-511.

[5] J.-F. Calvo-Ortega, M. Pozo, S. Moragues y J. Casals. «Fast protocol for radiochromic film dosimetry using a cloud computing web application». En: *Physica Medica* 39 (2017), pp. 1-8.

[6] I. Méndez, Ž. Šljivić, R. Hudej, A. Jenko y B. Casar. «Grid patterns, spatial inter-scan variations and scanning reading repeatability in radiochromic film dosimetry». En: *Physica Medica* 32 (9 2016), pp. 1072-1081.

[7] T. Kamomae y col. «Characterization of stochastic noise and post-irradiation density growth for reflective-type radiochromic film in therapeutic photon beam dosimetry». En: *Physica Medica* 32.10 (2016), pp. 1314-1320.

[8] I. Méndez, V. Hartman, R. Hudej, A. Strojnik y B. Casar. «Gafchromic EBT2 film dosimetry in reflection mode with a novel plan-based calibration method». En: *Medical Physics* 40.1 (2013), p. 011720.

[9] L. Chang, S. Ho, T. Lee, S. Yeh, H. Ding y P. Chen. «Calibration of EBT2 film using a red-channel PDD method in combination with a modified three-channel technique». En: *Medical Physics* 42.10 (2015), pp. 5838-5847.

[10] B. C. Ferreira, M. C. Lopes y M. Capela. «Evaluation of an Epson flatbed scanner to read Gafchromic EBT films for radiation dosimetry». En: *Physics in Medicine & Biology* 54.4 (2009), pp. 1073-1085.

[11] M. Martišíková, B. Ackermann y O. Jäkel. «Analysis of uncertainties in Gafchromic® EBT film dosimetry of photon beams». En: *Physics in Medicine & Biology* 53.24 (2008), pp. 7013-7027.

[12] L. I. Ramos-Garcia y J. F. Pérez-Azorin. «Improving the calibration of radiochromic films by the use of uncertainties in optical density and dose». En: *Medical Physics* 40.7 (2013), p. 071726.

[13] R. R. Mayer, F. Ma, Y. Chen, R. I. Miller, A. Belard, J. McDonough y J. J. O'Connell. «Enhanced dosimetry procedures and assessment for EBT2 radiochromic film». En: *Medical Physics* 39.4 (2012), pp. 2147-2155.

[14] A. Micke, D. F. Lewis y X. Yu. «Multichannel film dosimetry with nonuniformity correction». En: *Medical Physics* 38.5 (2011), pp. 2523-2534.

[15] J. P. Chung, S. W. Oh, Y. M. Seong, K. J. Chun y H.-T. Chung. «An effective calibration technique for radiochromic films using a single-shot dose distribution in Gamma Knife®». En: *Physica Medica* 32 (2016), pp. 368-378.

[16] C. Ruiz-Morales, J. A. Vera-Sánchez y A. González-López. «On the recalibration process in radiochromic film dosimetry». En: *Physica Medica* 42 (2017), pp. 67-75.

[17] S. Saur y J. Frengen. «GafChromic EBT film dosimetry with flatbed CCD scanner: A novel background correction method and full dose uncertainty analysis». En: *Medical Physics* 35.7 (2008), pp. 3094-3101.

[18] H. Bouchard, F. Lacroix, G. Beaudoin, J. F. Carrier y I. Kawrakow. «On the characterization and uncertainty analysis of radiochromic film dosimetry». En: *Medical Physics* 36.6 (2009), pp. 1931-1946.

[19] Joint Committe for Guides in Metrology. *Evaluation of measurement data – Guide to the expression of uncertainty in measurement (GUM 1995 with minor corrections)*. Inf. téc. 2008.

[20] A. González-López, J. A. Vera-Sánchez y C. Ruiz-Morales. «Technical Note: Statistical dependences between channels in radiochromic film readings. Implications in multichannel dosimetry». En: *Medical Physics* 43.5 (2016), pp. 2194-2199.

[21] A. Niroomand-Rad y col. «Radiochromic film dosimetry: Recommendations of AAPM Radiation Therapy Committee Task Group 55». En: *Medical Physics* 25.11 (1998), pp. 2093-2115.

[22] Joint Committe for Guides in Metrology. *Evaluation of measurement data – Supplement 1 to the Guide to the expression of uncertainty in measurement – Propagation of distributions using a Monte Carlo method*. Inf. téc. 2008.

[23] I. G. Hughes y T. P. Hase. *Measurements and their Uncertainties, A Practical Guide to Modern Error Analysis*. 1.ª ed. Oxford University Press, 2010.

[24] Joint Committe for Guides in Metrology. *Evaluation of measurement data – Supplement 2 to the Guide to the expression of uncertainty in measurement – Extension to any number of output quantities*. Inf. téc. 2011.

[25] D. S. Sivia. *Data Analysis: A Bayesian Tutorial*. 1.ª ed. Oxford Science Publications, 1996.

[26] INTERNATIONAL ATOMIC ENERGY AGENCY. *Absorbed Dose Determination in External Beam Radiotherapy*. Technical Reports Series 398. Vienna: INTERNATIONAL ATOMIC ENERGY AGENCY, 2000.

[27] P. Castro, F. García-Vicente, C. Mínguez, A. Floriano, D. Sevillano, L. Pérez y J. Torres. «Study of the uncertainty in the determination of the absorbed dose to water during external beam radiotherapy calibration». En: *Journal of Applied Clinical Medical Physics* 9.1 (2008), p. 2676.

[28] D. Lewis, A. Micke, X. Yu y M. F. Chan. «An efficient protocol for radiochromic film dosimetry combining calibration and measurement in a single scan». En: *Medical Physics* 39.10 (2012), pp. 6339-6350.

[29] J. Ross-Macdonald y W. J. Thompson. «Least-squares fitting when both variables contain errors: Pitfalls and possibilities». En: *American Journal of Physics* 60.1 (1992), pp. 66-73.

[30] J. C. Lagarias, J. A. Reeds, M. H. Wright y P. E. Wright. «Convergence Properties of the Nelder-Mead Simplex Method in Low Dimensions». En: *SIAM Journal of Optimization* 9.1 (1998), pp. 112-147.

[31] J. S. Alpher y R. I. Gelb. «Standard errors and confidence intervals in nonlinear regression: comparison of Monte Carlo and parametric statistics». En: *The Journal of Physical Chemistry* 94.11 (1990), pp. 4747-4751.

Capítulo 4

Incidence of the different sources of noise on the uncertainty in radiochromic film dosimetry using single channel and multichannel methods

Phys Med Biol. 2017 Nov 1;62(22):N525-N536

Incidence of the different sources of noise on the uncertainty in radiochromic film dosimetry using single channel and multichannel methods

Antonio González López[1], Juan Antonio Vera Sánchez[2], Carmen Ruiz Morales[3]

[1] *Hospital Universitario Virgen de la Arrixaca. El Palmar (Murcia), Spain*
[2] *Hospital Universitari Sant Joan de Reus, Servicio de Física Médica. Reus (Tarragona), Spain*
[3] *PhD Programme in Physics and Space Science of the University of Granada. Granada, Spain*

The incidence of the different sources of noise on the uncertainty in radiochromic film (RCF) dosimetry using single channel and multichannel methods is investigated in this work. These sources of noise are extracted from pixel value (PV) readings and dose maps.

Different pieces of a RCF were irradiated to uniform doses ranging from 0 to 1092 cGy. Then, the pieces were read at two resolutions (72 and 150 ppp) with two flatbed scanners: Epson 10000XL and Epson V800, representing two states of technology. Noise was extracted as described in ISO 15739, separating its different contributions: random noise and fixed pattern (FP) noise.

Regarding the PV maps, FP noise is the main source of noise for both models of digitizers. Also, the standard deviation of the random noise in the 10000XL model is almost twice that of the V800 model.

In the dose maps, the FP noise is smaller in the multichannel method than in the single channel ones. However, random noise is higher in this method along the whole dose range.

In the multichannel method, FP noise is reduced as a consequence of its ability to eliminate channel independent perturbations. However, the random noise increases because the dose is calculated as a linear combination of the doses obtained by the single channel methods. The values of the coefficients of this linear combination are obtained and the root of the sum of their squares is shown to range between 0.9 and 1.9 in the dose range studied.

These results make the random noise to play a fundamental role in the uncertainty of RCF dosimetry: low levels of random noise are required in the digitizer for fully exploiting the advantages of the multichannel dosimetry method. This is particularly important for measuring high doses with high spatial resolutions.

4.1. Introduction

The radiochromic film (RCF) EBT3 (Ashland, Inc., Wayne, NJ) is a widely used film for two-dimensional dosimetry in radiotherapy [1, 2]. Besides being self-developing and having a low sensitivity to room light [3], it is provided with a high spatial resolution, has a response within clinical dose levels [4], is near-tissue equivalent and has a very weak energy dependency [5], making the dose response insensitive to field size and depth. Also, the dose response is independent of the dose rate [6].

These properties make the EBT3 film suitable for radiation dosimetry in quality assurance of treatment planning systems and linear accelerators. In particular, this film is a widely used verification tool for intensity modulated radiation therapy [7, 8]. However, the response of RC films has a poor spatial homogeneity due to differences in the thickness of the active layer [9], which constitutes a main drawback for dosimetric applications. Moreover, digitizing the films also introduces complex inhomogeneities. Van Battum et al. [10] and Schoenfeld et al. [11] show that important lateral inhomogeneities are introduced by a flatbed scanner, and these inhomogeneities are function of the dose.

Aimed at mitigating spatial inhomogeneities and lateral scanning artefacts, multichannel film dosimetry methods [12-14] have been introduced. These methods take advantage of the spectral sensitivity of the film and the available information in the three channels RGB of the scanned image and calculate the dose as a linear combination of the doses obtained by the three single channel methods.

After irradiating and reading the film, the reading is converted to dose. The resulting dose map contains the dosimetric information of interest: the measurement of dose at every point of the film. In addition to this, other undesirable contributions as noise are included in the dose map. Noise is an important source of uncertainty in the dose determination, since it introduces errors in film readings that propagate through the dosimetric chain and can lead to errors in the final dosimetric evaluation [15].

Recommendation ISO 15739 [16] specifies methods for measuring and reporting noise versus signal level on digital cameras. The recommendation provides a method to split noise sources such as random or temporal noise and fixed pattern noise (FPN) arising from the imager and the film.

In RCF dosimetry FP noise has two main components. On the one si-

de, spots of spontaneous polymerization, scratches on the film substrates or dust produce high frequency noise patterns. On the other hand, thicknesses variations of the active layer and the lateral artefact of the flatbed scanners give rise to low frequency noise patterns. Random noise is due to quantum noise in the radiation field, lamp intensity fluctuations of the digitizer and electronic noise.

In this work, the methods of ISO 15739 are applied to radiochromic film readings. The objective is to separate random noise from FP noise in both PV maps and dose maps. Noise energy is studied as a function of dose for two different flat-bed digitizers operating at two different resolutions.

The goal is presenting how the different components of noise affect the uncertainty in the dose determination in both digitizers and for the different dosimetric methods analysed. In particular, we show the different effects that random and FP noises have on the noise in dose maps obtained with the multichannel method.

4.2. Materials and methods

4.2.1. Films, irradiation and digitization

Seven cutouts of size 120 mm × 23 mm from an EBT3 film were irradiated in a Varian Clinac (Varian Medical Systems, Palo Alto, CA) with 6MV x-ray beams. The cutouts were placed in a slabbed RW3 phantom and large fields (field size of 250 mm × 250 mm) were used to provide an uniform dose (with a uniformity lower than 1.5 %) at each piece of film. The dose levels used were 0, 182, 364, 546, 728, 910 and 1092 cGy. Also, two pieces of 60 mm × 23 mm were cut for the two level correction, one for background and one for a dose of 1274 cGy.

For every cutout, nine adjacent regions of 10 mm × 10 mm were selected and in each of these region noise sources were obtained. The final result for a given cutout was calculated by averaging each noise component over these nine regions. In this way, although the analysis area for noise distilling calculation is kept small, the results obtained represent a wider area of the film. Keeping a small area guarantees high dose uniformity through it.

After irradiation, all the film cutouts were assembled on the digitizers' beds and were read. The digitizers used were two Epson 10000XL and two

Epson V800 (Epson America, Inc., Long Beach, CA, USA). For each model, two digitizers were used. Also, two spatial resolutions were investigated: 72 dpi and 150 dpi, and a signal resolution of 48 bits (16 per channel) was selected. Films were placed in the centre of the digitizer bed and no correction nor filters were applied during acquisition. The digitizer was powered on 30 min before reading and five readings were taken and discarded for warming purposes. Images were stored in TIFF format.

For each digitizer and each resolution, a number of $R = 20$ readings of the same film were used for the study of noise, giving rise to twenty images. In order to avoid the inter-scan effect [15], two control cutouts were used to carry out a two levels correction throughout all the repeated scans. For this reason, the scanning area was kept fixed and included both control cutouts, placed in a fixed position in the digitizer bed.

After each reading, the pixel values in each image were linearly corrected in such a way that the mean PV of two ROIs, one for each control cutout, was the same for the twenty different images of a given digitizer and resolution.

4.2.2. Noise distilling

The study of noise is carried out firstly in the PV domain. In this work noise is considered the sum of random and fixed pattern contributions, and the pixel variance is assumed to be the sum of its components

$$\sigma_{tot}^2 = \sigma_{random}^2 + \sigma_{fp}^2, \tag{4.1}$$

where σ_{tot} stands for the standard deviation of total noise or root mean square (RMS) fluctuation over a nominally uniform area, σ_{random} is the standard deviation of random noise observed from scan to scan and σ_{fp} is the standard deviation of the fixed pattern noise.

The total variance estimate s_{tot}^2 was computed over all pixels of each region and the entire data set of R images. Considering all the data as a matrix $x_{i,j,r}$, where i and j stand for the pixel value at row i and column j respectively and r refers to reading number,

$$s_{tot}^2 = \frac{1}{IJR-1} \sum_{i=1}^{I} \sum_{j=1}^{J} \sum_{r=1}^{R} \left(x_{ijr} - \overline{x}\right)^2, \tag{4.2}$$

where I and J are the number of rows and columns in the reading region

and $\overline{x}$ is the grand mean

$$\overline{x} = \frac{1}{IJR} \sum_{i=1}^{I} \sum_{j=1}^{J} \sum_{r=1}^{R} x_{i,j,r}. \tag{4.3}$$

Averaging of each group of R images reduces the random noise and the resulting averaged image approximates a random noise free image. Under this approximation, the random noise can be estimated from the differences between each digitization and the average image. The mean pixel value at position (i, j) can be obtained as

$$\overline{x}_{i,j} = \frac{1}{R} \sum_{r=1}^{R} x_{i,j,r} \tag{4.4}$$

Also, the sample variance for the temporal noise at position (i, j) can be estimated as

$$s^2_{i,j} = \frac{1}{R-1} \sum_{r=1}^{R} (x_{i,j,r} - \overline{x}_{i,j})^2. \tag{4.5}$$

Then, an estimation of the random noise variance can be calculated as

$$s^2_{random} = \frac{1}{IJ} \sum_{i=1}^{I} \sum_{j=1}^{J} s^2_{i,j}, \tag{4.6}$$

Also, the mean image $\overline{x}_{i,j}$ can be used to estimate the fixed pattern noise with the aid of the mean value $\overline{x}$,

$$\overline{x} = \frac{1}{IJ} \sum_{i=1}^{I} \sum_{j=1}^{J} \overline{x}_{i,j}. \tag{4.7}$$

$$s^2_{fp} = \frac{1}{IJ-1} \sum_{i=1}^{I} \sum_{j=1}^{J} (\overline{x}_{i,j} - \overline{x})^2 - \frac{s^2_{random}}{R}. \tag{4.8}$$

The last term in equation 4.8 eliminates the contribution of the random noise remaining in the mean image.

4.2.3. Noise in dose maps. Effect of conversion to dose

Dose was calculated by three single channel methods, using the red, green and blue channels respectively. For every channel, a lot calibration curve was

used (see figure 4.1). These lot calibration curves were corrected for each reading following the efficient protocol of Lewis et al. [17]. Also, the dose was calculated by the multichannel method of Mayer et al. [12].

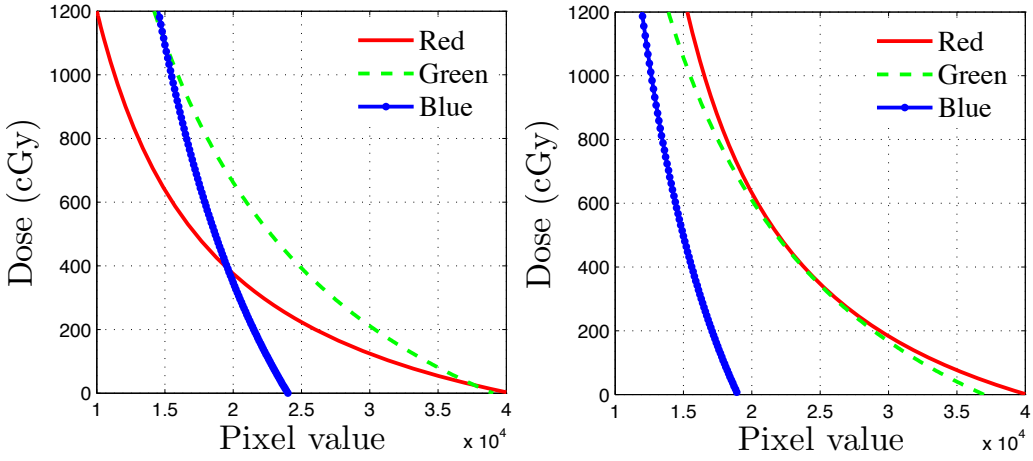

(a) Epson 10000XL. (b) Epson v800.

Figure 4.1: Lot calibration curves used to convert pixel values to doses for each of the three colour channels and both digitizer models.

In the multichannel algorithm, dose is calculated as a linear combination of the doses calculated using the single channel methods,

$$D_{MC} = aD_R + bD_G + cD_B, \tag{4.9}$$

where D_{MC}, D_R, D_G and D_B are the doses calculated by the multichannel, red, green and blue methods respectively. According to Mayer et al. coefficients a, b and c depend on both the dose D and the independent channel perturbation Δ [12] and are a function of the spatial coordinates of the film.

The statistical distributions of each of the coefficients a, b and c were investigated. These distributions were studied from one of the readings of the films. In this way, for instance, the sample for coefficient a consists of a set $\{a_i, D_i\}$, were i stands for the spatial coordinates of the reading image, D_i is the dose calculated at position i and a_i is the value of coefficient a at i.

Then, the statistical dependencies between the coefficients a, b and c and the dose D was studied by means of the joint histograms of each coefficient and the dose. By normalization of these histograms the joint probability density function (PDF) of each coefficient and the dose was obtained, and from these PDF's the experimental expected value of each coefficient given

the dose was calculated. These values and equation 4.9 allow us to know the relationship between random noise in single-channel methods and random noise in the multichannel method.

After converting to dose, noise distilling was carried out on dose maps, following the procedure explained in subsection 4.2.2.

4.3. Results

4.3.1. Noise distilling in PV maps

As mentioned in the previous section, two digitizers were analysed for the 10000XL model and two digitizers for the V800 one. The results obtained in both cases for digitizers from the same model were very similar. As an example, figure 4.2 shows the random and FP noise sources in the red channel for two 10000XL digitizers and the resolution of 72 ppp.

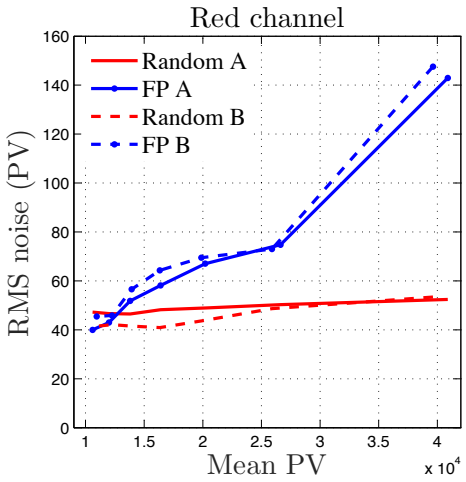

Figure 4.2: Comparison of noise sources (random and FP) in the red channel of radiochromic film readings for two Epson 10000XL digitizers (named A and B in the figure) and a resolution of 72 ppp.

Figures 4.3(a) and 4.3(b) show the components of noise for the Epson 10000XL and Epson V800 digitizers respectively for the resolution of 72 ppp. Each subfigure shows the results found for the three colour channels: red, green and blue. Two components are shown, random noise calculated as in equation 4.6 and FP noise calculated as in equation 4.8. Total noise as calculated by equation 4.2 is also presented.

For both digitizers, these figures show how total noise increases with increasing pixel value for the red and the green channels. This trend is also followed for the FP noise in these channels. Noise in the blue channel does not show such a strong dependence on the pixel value, particularly in the Epson 10000XL, where it remains fairly constant.

Contrary to what is shown in the case of the FP noise, random noise does not show a dependence on the pixel value. In both digitizers, the random noise remains fairly constant through the whole range of pixel values and colour channels.

Figures 4.3(c) and 4.3(d) show the components of noise for the red channel and the resolution of 150 dpi of the Epson 10000XL and Epson V800 digitizers respectively. Both, random and FP noises increase with resolution and the shape of the curves resemble those of the lower resolution. Similar results were found for the green and blue channels at the resolution of 150 dpi.

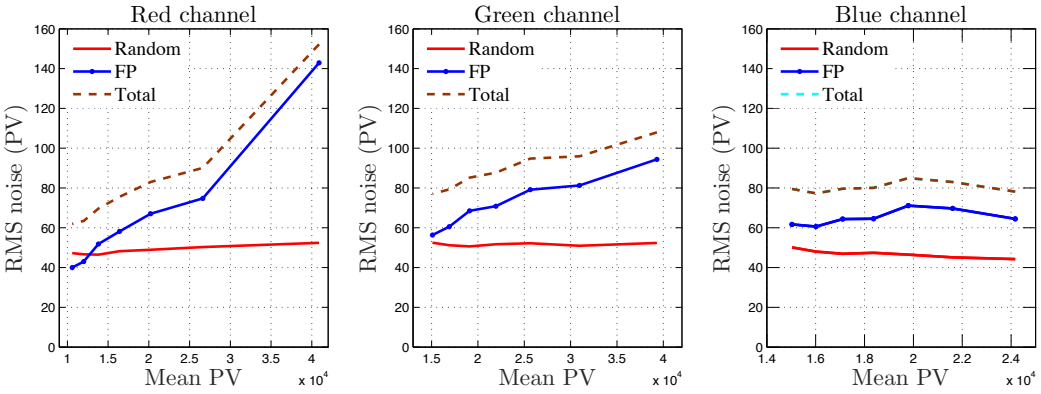

(a) Epson 10000XL. 72 ppp.

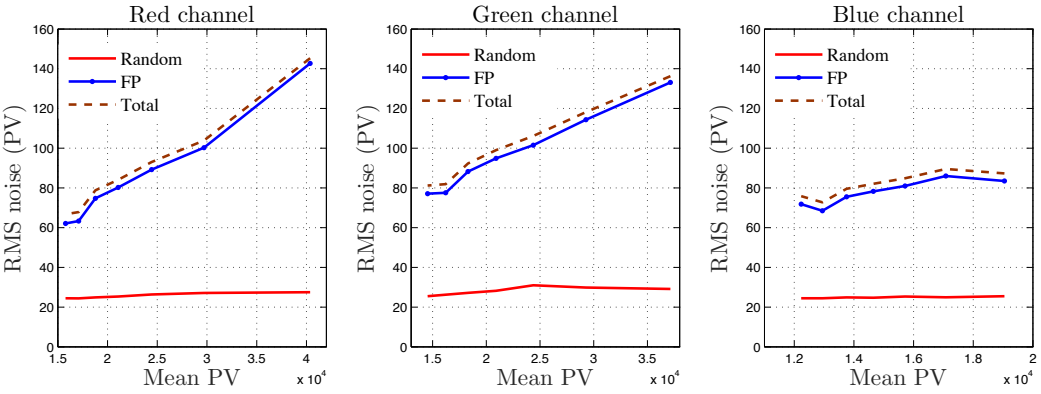

(b) Epson V800. 72 ppp.

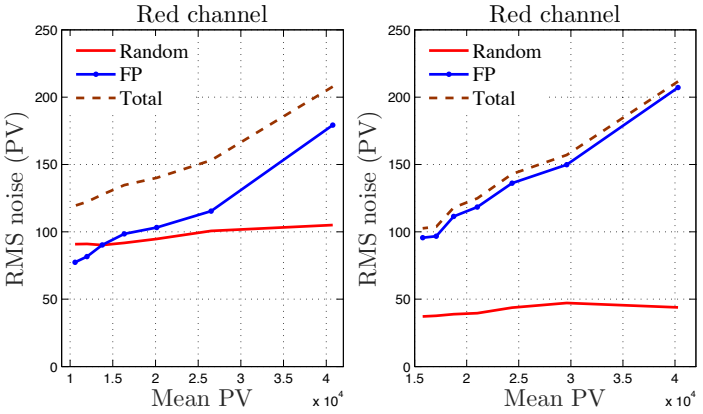

(c) Epson 10000XL. 150 ppp. (d) Epson V800. 150 ppp.

Figure 4.3: Noise sources in radiochromic film readings for two digitizers. The resolution was of 72 ppp (subfigures (a) and (b)) and 150 ppp (subfigures (c) and (d)).

4.3.2. Components of the dose calculation by the multichannel algorithm

Figure 4.4 shows the expected values of the coefficients a, b and c of equation 4.9 given the dose D (left), and the square root of the sum of their squares (right).

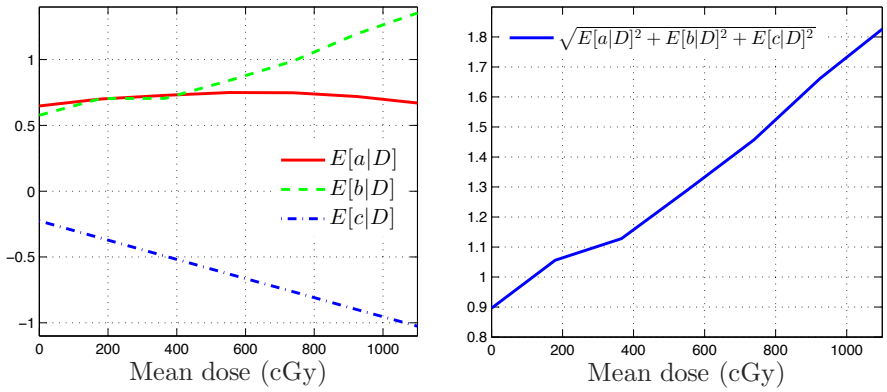

Figure 4.4: Expected values of the coefficients in the multichannel calculation method (left). Square root of the sum of the squares of the coefficients (right).

The contribution of the red channel to the multichannel dose calculation is represented by the coefficient a in equation 4.9 and ranges between 0.65 and 0.75 when the dose varies from 0 to 1092 cGy. The range of variation of the coefficients for the green b and blue c channels are 0.57 to 1.365 and -0.22 to -1.04 respectively. The square root of the sum of the square of the expected values of the coefficients a, b and c is smaller than one at zero dose, but increases up to 1.84 at 1092 cGy.

With the exception of the red channel, the absolute value of the coefficients increases with increasing dose, which implies that random noise in the multichannel method is rapidly amplified.

4.3.3. Noise distilling in dose maps

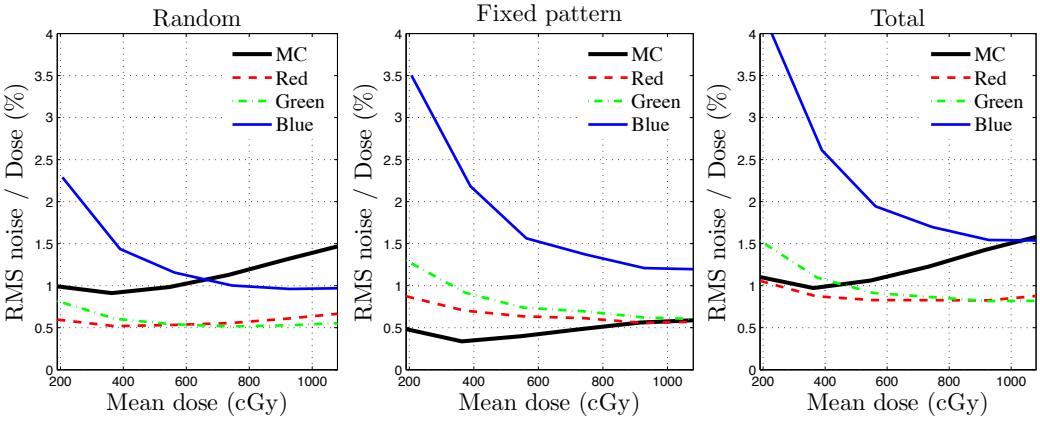

(a) Epson 10000XL. 72 ppp.

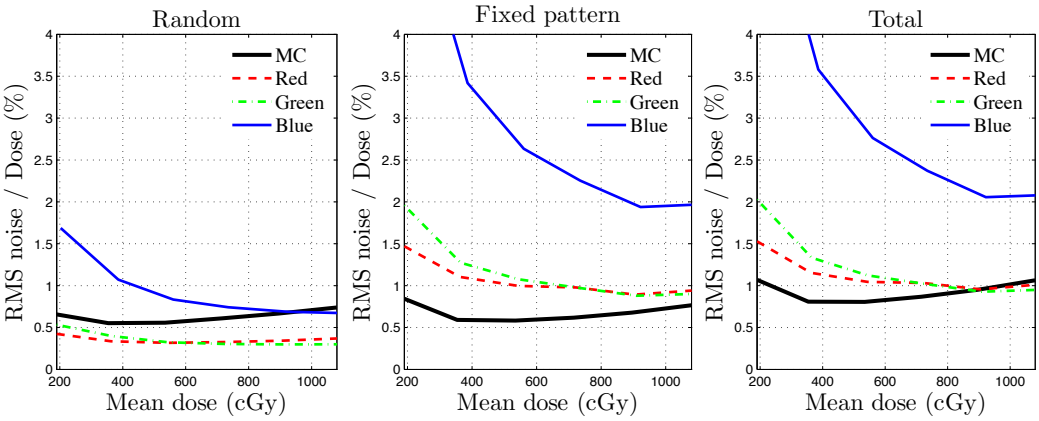

(b) Epson V800. 72 ppp.

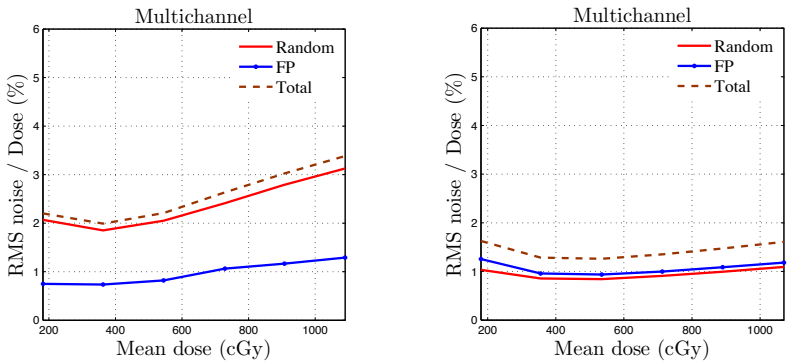

(c) Epson 10000XL. 150 ppp.

(d) Epson V800. 150 ppp.

Figure 4.5: Noise distilling in the dose maps using two digitizers for three single channel methods (red, green and blue) and the multichannel (MC) method. Relative noise is shown for resolutions of 72 ppp (subfigures (a) and (b)) and 150 ppp (subfigures (c) and (d)).

Figure 4.5 shows relative noise levels in dose maps. Figures 4.5(a) and 4.5(b) show the components of noise for two digitizers at the resolution of 72 ppp. Random noise is always higher in the multichannel method than in the red and green single channel methods. It also exceeds the blue channel at doses above 650 cGy (10000XL) and 900 cGy (V800).

The FP noise is lower in the multichannel than in the single channel methods in both digitizers (see figures 4.5(a) and 4.5(b)). For the highest doses, the FP noise in the multichannel approaches to FP noise in the red and green methods.

Figures 4.5(c) and 4.5(d) show the components of noise in dose maps for the multichannel method at the resolution of 150 ppp. In all cases increasing the spatial resolution increases the random and FP noise, but the shape of the curves and their contributions to the total noise are similar to those found at the resolution of 72 ppp.

It's worth noting the important contribution of random noise to total noise in dose maps calculated in the 10000XL digitizer following the multichannel method (figure 4.5(a)). As a consequence, total noise is clearly higher for the multichannel than for the single channel red and green methods, especially for doses higher than 4 Gy. On the contrary, total noise is kept similar for these three methods in the V800 digitizer (figure 4.5(b)) at the highest dose levels.

4.4. Discussion

A common characteristic of the random noise in PV maps is found: For a given digitizer and resolution, random noise is kept fairly constant through the whole range of doses and through the different colour channels (see figure 4.3). In dose maps, however, absolute random noise increases with dose and is higher in the blue channel than in the red and green ones. It's worth noting how relative random noise in the red and green channels changes slowly with the dose, remaining fairly constant in a wide range of doses (figures 4.5(a) and 4.5(b)).

The relationship between PV and dose explains these different behaviours. For every pixel value and every colour channel $PV_k, k = R, G, B$, a dose value is calculated using a rational function $D_k = \alpha_k + \frac{\beta_k}{PV_k - \gamma_k}$. Noise in PV_k is propagated to D_k through this rational function, and the absolute value of the slope of this curve increases with dose (see figure 4.1), increasing noise.

The same results are expected for other types of functions converting PV to dose, like polynomial or power functions, since the slopes of their curves are expected to be similar to that of the rational one. It also applies to those protocols using optical density (OD), obtained as $OD = -log_{10}(PV/PV_{max})$ [18], since the function f that converts OD into dose $D = f(OD)$ can be seen as one of the functions in a composition of functions g that converts PV into dose $D = g(PV) = f(-log_{10}(PV/PV_{max}))$.

The FP noise in the blue channel shows another big difference between PV and dose maps. FP noise in the blue channel is lower than in the red or green ones (figures 4.3(a) and 4.3(b)). In the dose maps (figures 4.5(a) and 4.5(b)) the situation is reversed, with the highest FP noise variances found in the blue channel. This can also be explained in terms of the slope of the curves used to convert PV into dose: The absolute value of the slope is higher in the case of the blue channel (figure 4.1).

Regarding the multichannel method, the noise components have different behaviours. On the one hand, the FP noise is lower than in the single-channel methods. This fact can be explained because this method reduces the effect of the independent channel perturbations, and these perturbations are part of the FP noise. On the other hand, random noise is higher than in the red and green single channel methods. Since random noise in the different channels can be considered uncorrelated [19], the variance of random noise in the multichannel method $\sigma^2_{random}(MC)$ can be obtained as

$$\sigma^2_{random}(MC) = a^2\sigma^2_{random}(R) + b^2\sigma^2_{random}(G) + c^2\sigma^2_{random}(B), \qquad (4.10)$$

where a, b and c are the coefficients in equation 4.9 and $\sigma^2_{random}(R)$, $\sigma^2_{random}(G)$ and $\sigma^2_{random}(B)$ are the variances of random noise in the red, green and blue channels respectively.

The square root of the sum of the square of the expected values of the coefficients a, b and c increases with the dose up to 1.84 (figure 4.4). This number would represent the amplification of standard deviation of the random noise in the multichannel case if the variances of noise in every single channel were the same.

At low doses, random noise is quite higher in the blue channel than in the red and green ones. This makes that equation 4.10 can be simplified by $\sigma^2_{random}(MC) = c^2\sigma^2_{random}(B)$ and, since c^2 is lower than one at these low doses, the random noise is lower in the multichannel than in the blue channel method. This situation changes at high doses, where the relative differences

between channels are reduced. Then, the increase in the absolute value of coefficients a, b and c with the dose is responsible of the increase in the random noise.

Regarding total noise, for the 1000XL digitizer, figure 4.5(a) shows how the red, green and multichannel methods have similar noise for doses less than 400 cGy. From this value of the dose, the noise in the multichannel becomes higher and reaches the blue channel at a dose of 1000 cGy. For the V800 digitizer the results are different, and the lowest noise is found in the multichannel method for doses between 0 and 850 cGy (figure 4.5(b)).

The lower levels of random noise in the readings of the V800 digitizer keep random noise in the dose maps similar to FP noise, preventing the high rise of total noise found in the 10000XL digitizer.

4.5. Conclusion

In this work we present a method for distilling the sources of noise in RCF dosimetry. The method is used to study two models of digitizers and is applied to both PV maps and dose maps.

In both digitizers and for all the colour channels and resolution, FP noise increases with the PV. Contrary to this, random noise is fairly constant and independent of PV. Converting PV to dose makes relative noise to slightly decrease with increasing dose in the red and green channels. For the multichannel method, relative total noise reaches a minimum at 364 cGy and increases with dose from this dose value on. In this method, the increase is more important for the 10000XL digitizer than for the V800 one, being total noise in the 10000XL two times higher than in the V800 for a dose of 1092 cGy and a resolution of 150 ppp (figures 4.5(c) and 4.5(d)).

The main difference found in the readings of both digitizers lies in the random noise. Random noise RMS in the V800 model is about one half the random noise in the 10000XL model in all the colour channels and the resolutions studied.

This has an important effect on the total noise in the dose determination by means of the multichannel method. This method reduces part of the FP noise, as the channel independent perturbation component, but has not such an important effect on the random noise. This makes random noise to dominate the total noise in the 10000XL model. On the contrary, the low level

of random noise in the V800 prevents this effect and reduces the total noise especially at high doses and high spatial resolutions.

[1] J. El Barouky, N. Fournier-Bidoz, A. Mazal, G. Fares y J. Rosenwald. «Practical use of Gafchromic® EBT films in electron beams for in-phantom dose distribution measurements and monitor units verification». En: *Physica Medica* 27.2 (2011), pp. 81-88.

[2] A. L. Palmer, A. Nisbet y D. Bradley. «Verification of high dose rate brachytherapy dose distributions with EBT3 Gafchromic film quality control techniques». En: *Physics in medicine & biology* 58.3 (2013), pp. 497-511.

[3] M. J. Butson, P. K. N. Yu y P. E. Metcalfe. «Effects of read-out light sources and ambient light on radiochromic film». En: *Physics in Medicine & Biology* 43.8 (1998), p. 2407.

[4] M. Martišíková y O. Jäkel. «Study of Gafchromic® EBT film response over a large dose range». En: *Physics in Medicine & Biology* 55.10 (2010), N281.

[5] B. Arjomandy, R. Tailor, A. Anand, N. Sahoo, M. Gillin, K. Prado y M. Vicic. «Energy dependence and dose response of Gafchromic EBT2 film over a wide range of photon, electron, and proton beam energies». En: *Medical Physics* 37.5 (2010), pp. 1942-1947.

[6] L. Karsch, E. Beyreuther, T. Burris-Mog, S. Kraft, C. Richter, K. Zeil y J. Pawelke. «Dose rate dependence for different dosimeters and detectors: TLD, OSL, EBT films, and diamond detectors». En: *Medical Physics* 39.5 (2012), pp. 2447-2455.

[7] A. H. Aitkenhead, C. G. Rowbottom y R. I. Mackay. «Marvin: an anatomical phantom for dosimetric evaluation of complex radiotherapy of the head and neck». En: *Physics in Medicine & Biology* 58.19 (2013), p. 6915.

[8] L. Marrazzo, M. Zani, S. Pallotta, C. Arilli, M. Casati, A. Compagnucci, C. Talamonti y M. Bucciolini. «GafChromic® EBT3 films for patient specific IMRT QA using a multichannel approach». En: *Physica Medica* 31 (2015), pp. 1035-1042.

[9] A. Niroomand-Rad y col. «Radiochromic film dosimetry: Recommendations of AAPM Radiation Therapy Committee Task Group 55». En: *Medical Physics* 25.11 (1998), pp. 2093-2115.

[10] L. J. Van Battum, D. Hoffmans, H. Piersma y S. Heukelom. «Accurate dosimetry with GafChromic^{TM} EBT film of a 6 MV photon beam in water: What level is achievable?» En: *Medical Physics* 35.2 (2008), pp. 704-716.

[11] A. A. Schoenfeld, S. Wieker, D. Harder y B. Poppe. «The origin of the flatbed scanner artifacts in radiochromic film dosimetry—key experiments and theoretical descriptions». En: *Physics in Medicine & Biology* 61.21 (2016), p. 7704.

[12] R. R. Mayer, F. Ma, Y. Chen, R. I. Miller, A. Belard, J. McDonough y J. J. O'Connell. «Enhanced dosimetry procedures and assessment for EBT2 radiochromic film». En: *Medical Physics* 39.4 (2012), pp. 2147-2155.

[13] A. Micke, D. F. Lewis y X. Yu. «Multichannel film dosimetry with nonuniformity correction». En: *Medical Physics* 38.5 (2011), pp. 2523-2534.

[14] I. Méndez. «Model selection for radiochromic film dosimetry». En: *Physics in Medicine & Biology* 60.10 (2015), p. 4089.

[15] J. A. Vera-Sánchez, C. Ruiz-Morales y A. González-López. «Technical Note: Characterization of noise and digitizer response variability in radiochromic film dosimetry. Impact on treatment verification». En: *Physica Medica* 32.9 (2016), pp. 1167-1176.

[16] ISO 15739. *Photography. Electronic Still-Picture Imaging. Noise Measurements*. Inf. téc. Switzerland, 2013.

[17] D. Lewis, A. Micke, X. Yu y M. F. Chan. «An efficient protocol for radiochromic film dosimetry combining calibration and measurement in a single scan». En: *Medical Physics* 39.10 (2012), pp. 6339-6350.

[18] S. Devic, N. Tomic y D. Lewis. «Reference radiochromic film dosimetry: Review of technical aspects». En: *Physica Medica* 32 (2016), pp. 541-556.

[19] A. González-López, J. A. Vera-Sánchez y C. Ruiz-Morales. «Technical Note: Statistical dependences between channels in radiochromic film readings. Implications in multichannel dosimetry». En: *Medical Physics* 43.5 (2016), pp. 2194-2199.

Capítulo 5

Characterization of noise and digitizer response variability in radiochromic film dosimetry. Impact on treatment verification

Phys Med. 2016 Sep;32(9):1167-74

Characterization of noise and digitizer response variability in radiochromic film dosimetry. Impact on treatment verification

Juan Antonio Vera Sánchez[1], Carmen Ruiz Morales[2],Antonio González López[3]

[1] *Hospital Universitari Sant Joan de Reus, Servicio de Física Médica. Reus (Tarragona), Spain*
[2] *Hospital IMED, Servicio de Oncología Radioterápica. Elche (Alicante), Spain*
[3] *Hospital Universitario Virgen de la Arrixaca. El Palmar (Murcia), Spain*

Purpose: To study how noise and scanner response variability affect radiochromic film dosimetry. Methods: Five treatment plans were analyzed in this work with two different multichannel protocols: the multichannel algorithm of Mayer et al. and the efficient protocol of Lewis et al. Results and conclusion: The multichannel protocol of Mayer et al. is not able to compensate variability in scanner response, which is an important issue for radiochromic film dosimetry. The efficient protocol compensates variations of scanner response, so dose values and gamma scores become more accurate and reproducible. The compensation of digitizer scan variability of the efficient protocol, together with time averaging improve radiochromic film dosimetry. Noise is related to selected resolution in the scanner, our results show that if high resolution measurements are required, de-noising should be considered.

5.1. Introduction

Radiochromic (RC) film has a high spatial resolution and a small dependence on both energy spectrum and dose rate [1]. However, the film itself and scanners used for film reading have an important inhomogeneity issue [2-5]. Also, the amount of noise in a scanned image is a function of the scanning resolution [6].

Therefore, the scanner variability and the digitization set-up must be taken into account for accurate dosimetry with RC films. The process of film digitization has been widely developed. There are two known methods for dealing with the issue of noise: spatial averaging and time averaging. Spatial averaging is appropriate for dose estimation of a piece of film exposed to an homogeneous dose [7], but it results in an undesirable lack of spatial resolution when evaluating more complex dose distributions. Time averaging is limited by changes in the response of the scanner that may lead to a loss of accuracy [6, 8]. In addition, noise level has been estimated as the standard deviation of the pixel value or the net optical density of a region exposed to a uniform dose [7, 9], but quantifying the noise in a complex distribution of dose is still an unsolved problem.

Multichannel film dosimetry methods [10-14] have been introduced to take advantage of the spectral sensitivity of the film and the available information in the three channels of the scanned RGB(Red, Green, Blue) image. These multichannel methods are aimed to partially mitigate spatial inhomogeneities of the film and lateral scanning artifacts. Two different multichannels methods are compared in this study: the multichannel method of Mayer et al (MC), that works with a unique calibration for the whole lot and the efficient protocol of Lewis et al (EP), that introduces a two level correction in order to provide a specific calibration for every digitalization.

In this work, the influence of the film reading variability and noise added by the scanner on RC film dosimetry with two different multichannel methods is analyzed. Also, a novel method for the estimation of noise in dose maps obtained from RC film by means of wavelet processing is introduced. And, finally, de-noising capabilities by combining time averaging and efficient protocol are studied. In particular, the impact of noise and digitizer variabilities in gamma scores is shown.

5.2. Materials and Methods

Three prostate and two cerebral VMAT treatment plans were analyzed. They were irradiated on a Trilogy Linac (Varian, Palo Alto, CA) with 6MV, and they were calculated with Analytical Anisotropic Algorithm (AAA) in Eclipse Treatment Planning System (Varian, Palo Alto, CA). Prostates 1 and 2 and cerebral cases 1 and 2 were prescribed with 2 Gy per fraction and prostate 3 was prescribed with 2.5 Gy per fraction.

For every plan, two dose maps (sagittal and coronal) were verified and accepted for clinical treatment using a Matrixx chamber array (IBA Dosimetry GmbH, Schwarzenbruck, Germany) placed in a MULTICUBE phantom. These treatment plans were also irradiated in the same phantom with EBT3 model Gafchromic films (Ashland Inc, USA).

5.2.1. Irradiation protocol for EBT3 films

Two lots of EBT3 films were used in this work. Lot ♯072281401 was employed to expose prostates 1 and 2 and cerebral 1 cases, and lot ♯12011401 was used for prostate 3 and cerebral 2 cases. Prior to film irradiation, linac output was measured for 6 MV beams using 20 cm x 20 cm field size at a depth of 10 cm (SSD = 90 cm) in a slabbed RW3 phantom with a PTW 30013 Farmer chamber and a Webline electrometer (PTW, Freiburg, Germany). For every film, two pieces of 4 cm x 20.3 cm were cut for the two level correction, one for background and one for a known dose value, and the rest of the film was used for the dose plane irradiation.

5.2.2. Digitalization protocol

The films were scanned using an EPSON EXPRESSION 10000XL (Seiko EPSON Corp., Nagano, Japan). It was switched on half an hour prior to measurements and a warm up of seven digitalizations was performed. The digitalizations were made with approximately one minute between consecutive scans. Three different scanning resolutions were used in this work, 72, 96 and 150 dpi. The digitalizations were made in positive film mode without image adjustment features, in portrait orientation, and the film was placed at the center of the scanner bed.

The films were scanned at least two hours post irradiation. The temporal

window between irradiations of pieces of the same film and digitalization was more than four times longer than the temporal interval between irradiation of pieces of the same film [10]. The films from the first lot, prostate 1 and 2 and cerebral 1 cases, were scanned three times at every interest resolution. The films from the second lot, prostate 3 and cerebral 2 cases, were scanned twenty times at every working resolution.

5.2.3. Analysis

The complete set of images for every film was analyzed with an in-house software developed with Matlab (Mathworks, Inc, Natick, MA). The available images were cropped symmetrically using the cross-hairs marks on the film with the same size fixed for all resolutions. Therefore, the investigated area was always the same for every plane, so gamma scores could be compared consistently. The regions of interest (ROIs) used for the two level correction of the efficient protocol were cropped in this way too.

Two different frameworks were considered. The first framework, based on films from lot ♯072281401, included three single digitized images for every studied resolution, and the set of available images was composed by these three single scanned images and an averaged image was created using Matlab. For every available image a dose map was calculated using a multichannel protocol, and an averaged dose map was calculated using Matlab, as described in Fig.5.1.

The second framework included twenty digitalizations for every film at each resolution. It was intended as a deeper investigation in the averaging process, including de-noising capabilities and accuracy gain regardless of changes in scanner response. Dose maps from single scanned images, dose maps from the average of the firsts three, five, ten, fifteen and twenty images and averaged dose maps of the firsts three, five, ten, fifteen and twenty dose maps -from the single scanned images- were then considered at each resolution. In this second framework, the same scheme of Fig.5.1 was followed, with the number of scans described before.

5.2.3.1. Multichannel methods

First, the multichannel algorithm of Mayer et al. [11] was implemented. This algorithm obtains a dose value for every pixel from a cost function working with the pixel values of the three channels (RGB) and a calibration

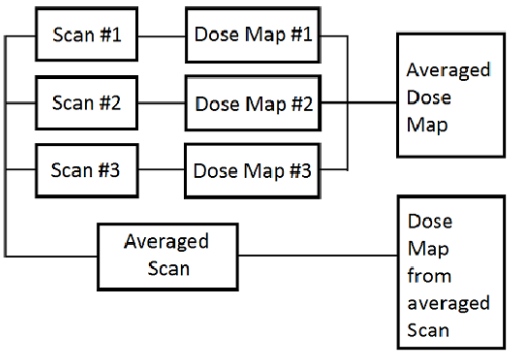

Figure 5.1: Followed scheme to obtain analyzed dose maps

-dose vs. pixel value- for every channel. The multichannel algorithm of Mayer et al. and the multichannel algorithm of Micke et al. [12] give rise to the same dose distribution [11]. The goal of this algorithm is the mitigation of the lateral response of the scanner and the compensation of variability in the thickness of the active layer.

Second, the efficient protocol of Lewis et al. [10] was implemented. This protocol works with a normalized specific calibration for the whole lot and, with the two pieces of the film exposed to known doses, derives a particular calibration for one digitalization that is intended to correct temperature and humidity deviations, and inter-scan and intra-lot variabilities. Once the particular calibration for the digitalization is obtained, the multichannel algorithm of Micke et al. works with this calibration and the corresponding image to obtain the dose map. The goal of this method is the mitigation of all mentioned variabilities, keeping the corrections included in the multichannel method.

5.2.3.2. Scanner response

The pixel values of the two cropped pieces used for the two level correction were analyzed to calculate the digitizer response variability. In addition, the impact of scanner variability in dose estimation was controlled by defining a dose ROI of 1 cm x 1 cm placed in a low gradient region, as shown in Fig. 2:

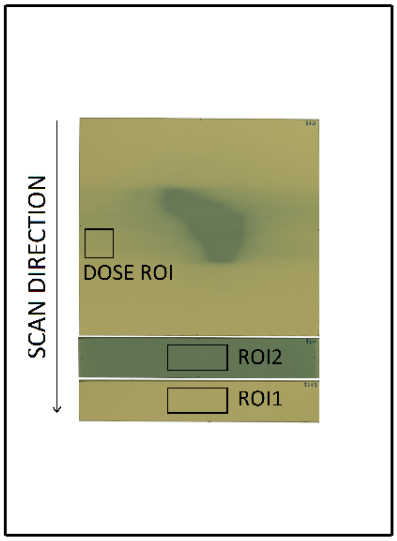

Figure 5.2: ROIs employed for the control of the scanner response (they are not shown to scale).

5.2.3.3. Noise metric

No filter was applied to images or dose maps. Only time averaging of images or dose maps was considered as a method for de-noising. Noise was considered as aleatory fluctuations of the pixel dose values, other variabilities such as the lateral artifact of the scanner, intra-lot variability of the films [9] and scanner response variability [6, 8] were considered as artifacts. The influence of the lateral artifact of the scanner was mitigated using the multichannel approaches [12] and the compensation of the intra-lot variability and the scanner response of the two multichannel approaches was studied.

Both multichannel approaches reduce the spatial variations of the sensitive gel thickness and the lateral response effect of the scanner. Both kinds of inhomogeneities dominate the low and medium frequency components of the spatial response. On the other hand, the high frequency components of the response variations are dominated by noise, and these are treated with de-noising methods. Therefore, in the case of noise the high frequency components of the response are of interest.

Also, taking into account the small bandwidth of the spatial dose distributions, a multiresolution approximation [15] may be employed to extract the noise components from a dose map and to compute the noise power. A multiresolution approximation decomposes an image in bands of frequency and, as pointed out previously [16], the variance of the noise can be calculated from the highest resolution band. In this work, for each dose map, a wavelet decomposition was carried out using the symlet family of wavelets sym4. From the absolute values of the highest resolution detail coefficients $w1$, the variance of noise was estimated [15, 16],

$$\sigma = \frac{Median(\mid w1 \mid)}{0{,}6745} \tag{5.1}$$

The method followed to estimate the noise variance assumes additive Gaussian noise. This assumption has been verified in flatbed scanners over films of homogeneous optical density [4]. In order to verify it in the present work, a new approach was followed: as twenty different dose maps from single scanned images were available for every dose plane, for every pixel of these dose maps, twenty different dose estimations were available. These samples of twenty dose estimations for every pixel were checked to be Gaussian by means of the Jarque-Bera test. The Jarque-Bera test is a two-sided goodness of fit test. The test statistic takes into account the sample size, the sample skewness and the sample kurtosis. In this work, the usual significance level of 0.05 was employed to carry out the test.

5.2.3.4. Gamma analysis

The gamma analysis [17, 18] is a common tool for the comparison of two dose distributions, the reference and the evaluated ones. The gamma index values are directly influenced by the geometry of the two distributions, the dose values of the reference distribution and the amount of noise in the reference distribution. The passing rate and mean gamma are directly influenced by the same factors than the gamma index values, as demonstrated in [17-19].

In this work, every dose plane was compared to several dose maps obtained from different images of the same film. In this context, the impact of the geometry was minimized by choosing the same analysis area and alignment for all investigated dose maps, regardless of resolution changes, as described in sections 5.2.2 and 5.2.3. With this precaution, now it is clear that do-

se maps of the same resolution exactly had the same spatial component of the gamma index, and dose maps of different resolutions only had slightly differences caused by different resolutions in the spatial component of the gamma index. Moreover, differences in the gamma parameters were caused by different values of the reference doses or by the amount of noise present in dose maps. The gamma analysis was performed in Matlab. The measured dose distributions in RC films were established as the reference distributions and the calculated dose maps were established as the evaluated distributions in order to avoid artificially improved gamma scores caused by noise [20]. Also, the evaluated distributions were corrected by corresponding daily linac output. Dose criteria were obtained from the evaluated distribution in order to avoid artificial increase of dose limiting values caused by noise. The analysis of all dose maps was realized according to the 3mm,3 %, 2mm, 2 % and 1mm, 1 % criteria with a threshold of 10 % of the maximum evaluated dose.

5.3. Results

5.3.1. First framework: Three scans

Results of analysis carried out for all available dose maps with 72 dpi of a film exposed to the coronal dose plane of the prostate 1 plan are shown in Table5.1. High frequency noise energy, passing rates and mean gamma values for 3mm,3 %, 2mm,2 % and 1mm,1 % criteria are shown for the two multichannel methods investigated. Dose maps 1 to 3 are obtained from single scanned images, averaged scan is obtained from the averaged image of the three single scanned images and averaged dose map is the average of the three dose maps.

Table 5.1: Noise energy, passing rate and mean gamma results for all available dose maps of the film exposed to the coronal plane of the prostate 1 dose plan and digitized with 72 dpi. MC stands for the Mayer et al. protocol and EP stands for the Lewis et al. protocol.

Dose Map	Noise Energy		3mm 3%				2mm 2%				1mm 1%			
			Passing Rate		Mean Gamma		Passing Rate		Mean Gamma		Passing Rate		Mean Gamma	
	MC	EP	MC	EP	MC	EP	MC	EP	MC	EP	MC	EP	MC	EP
Dose Map1	0.52	0.52	97.24	94.76	0.31	0.36	92.56	88.77	0.47	0.53	67.54	62.94	0.94	1.07
Dose Map2	0.52	0.52	97.11	94.86	0.31	0.35	92.45	89.14	0.47	0.53	67.53	63.32	0.94	1.06
Dose Map3	0.53	0.52	94.72	94.44	0.34	0.35	88.66	88.81	0.51	0.53	67.18	64.83	1.02	1.06
Averaged scan	0.22	0.22	97.06	95.24	0.30	0.34	92.35	89.35	0.45	0.51	70.08	65.31	0.91	1.03
Av. dose map	0.22	0.22	97.06	95.23	0.30	0.34	92.34	89.33	0.45	0.51	70.80	65.30	0.91	1.03

Noise energy and passing rate using 3mm, 3 % criteria for both methods

are shown in Table5.2 for prostate 1, prostate 2 and cerebral 1 plans. All sagittal planes and all resolutions used in this work are presented in this Table5.2.

Table 5.2: Noise energy and passing rate using 3mm,3 % criteria for all sagittal planes with Mayer et al. protocol and Lewis et al. protocol.

		Prostate1				Prostate2				Cerebral1			
		Noise Energy		Passing Rate		Noise Energy		Passing Rate		Noise Energy		Passing Rate	
	Dose Map	MC	EP	MC	EP	MC	EP	MC	EP	MC	EP	MC	EP
72dpi	Dose Map1	0.51	0.51	93.14	86.35	1.16	1.15	95.36	97.76	0.50	0.52	98.50	97.53
	Dose Map2	0.51	0.51	91.61	86.13	1.14	1.12	94.12	97.51	0.50	0.52	98.05	97.51
	Dose Map3	0.51	0.52	90.81	86.03	1.19	1.17	93.15	97.60	0.52	0.54	98.37	97.54
	Averaged Scan	0.21	0.21	92.35	86.85	0.48	0.47	95.28	98.40	0.21	0.21	98.77	98.36
	Av. dose map	0.21	0.21	92.34	86.84	0.48	0.47	95.27	98.39	0.21	0.21	98.78	98.36
96dpi	Dose Map1	3.87	3.94	91.45	83.21	8.73	8.67	93.30	94.48	3.90	4.06	95.10	94.28
	Dose Map2	3.84	3.89	90.64	82.58	8.78	8.68	91.79	94.17	3.94	4.10	94.87	93.89
	Dose Map3	3.90	3.93	90.07	83.26	8.78	8.69	91.34	94.13	3.92	4.06	95.39	93.97
	Averaged Scan	1.55	1.56	92.28	85.33	3.46	3.42	94.65	96.73	1.55	1.60	97.24	96.78
	Av. dose map	1.55	1.56	92.25	85.27	3.46	3.43	94.61	96.70	1.55	1.60	97.26	96.76
150dpi	Dose Map1	5.01	5.09	90.27	82.95	11.06	11.03	94.12	93.93	4.96	5.17	93.70	92.97
	Dose Map2	5.02	5.08	88.55	82.03	11.14	11.15	94.45	93.91	4.94	5.14	93.48	93.24
	Dose Map3	5.05	5.09	87.41	82.00	11.24	11.13	93.16	93.84	5.03	5.20	94.90	92.84
	Averaged Scan	2.19	2.20	90.69	84.65	4.82	4.79	96.52	96.55	2.15	2.22	96.56	96.24
	Av. dose map	2.19	2.20	90.64	84.59	4.83	4.80	96.48	96.51	2.15	2.22	96.58	96.22

Results from table 5.1 and table 5.2 show better gamma scores for the Mayer protocol in three of the four dose planes considered. In addition, a descending trend in passing rates with consecutive scans for the Mayer protocol is observed, while the Lewis protocol shows a more stable behaviour.

5.3.2. Second framework: Twenty scans

Figs. 5.3 to 5.5 correspond to sagittal plane of the prostate 3 case evaluated in this framework. All analyzed films exhibit a similar behaviour for treated points: scanner variability, noise energy and gamma analysis. Scanner variability results of the ROI 2 uniformly exposed are shown in Fig.5.3a. Pixel values are normalized to the value of the corresponding channel to first digitalization at 72 dpi. Deviations through all the performed digitalizations and all the resolutions taken into account are considerably minor in red and green channels than in the blue one. Scans 1 to 20 are single scanned images, and results of the averaged scans from the first three, five, ten, fifteen and twenty images are included. The impact of scanner variability in dose calculation is shown in Fig.5.3b. Dose ROI values are normalized to dose ROI value obtained from first digitalization at 72 dpi for every method. Dose maps 1 to 20 are obtained from single scans. Results of dose maps obtained

from averaged scans from the first three, five, ten, fifteen and twenty images and results of the average of dose maps from the first three, five, ten, fifteen and twenty single scan images are presented too.

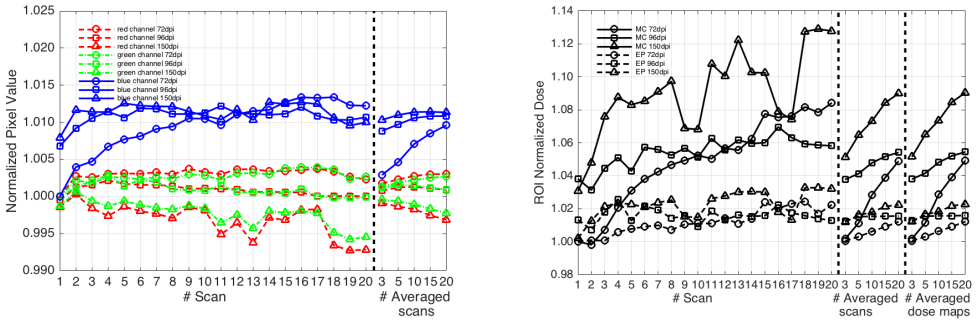

(a) (b)

Figure 5.3: Variability of digitizer response: (a) shows the evolution of averaged pixel value for ROI2 exposed to 3.04 Gy used for the two level correction.(b)Impact of scanner response in dose calculation for the multichannel method (MC) and the efficient protocol (EP)

Fig.5.3a shows the impact of inter-scan digitizer variabilities in the uniformly exposed ROI2, similar results were found for the unexposed ROI1. These variabilities in film readings are transferred to dose estimations as shown in Fig.5.3b. The Lewis protocol shows more stable dose estimations than the Mayer protocol. Dose maps from averaged scans and averaged dose maps also show dose estimations affected by this variability if the Mayer protocol is employed, while the Lewis protocol is able to compensate the effect of inter-scan variabilities in these dose maps.

Fig.5.4 shows noise energy values of all analyzed dose maps. Dose maps from single scanned images of the same resolution have very similar noise energy for both methods (dose maps 1 to 20). Dose maps from single scanned images of 150 dpi have the highest noise energy and dose map from single scanned images of 72 dpi the lowest noise energy. Dose maps from averaged scans and averaged dose maps have less noise than dose maps from single scanned images of the same resolution. Very similar values are found between noise energy of a dose map from averaged images and dose map from averaged dose maps derived from the same images. Results from the Jarque-Bera test show that the 94.8 % of the pixels have a Gaussian behaviour for the 72 dpi resolution. For the 96 dpi resolution the 94.9 % of the pixels have a Gaussian behaviour, while for the 150 dpi the percentage is the 95 % of the pixels.

Results of gamma analysis 3mm, 3 %, 2mm, 2 % and 1mm, 1 % criteria are shown in Fig.5.5 for sagittal plane of the prostate 3 plan.

Fig.5.6 shows the results of gamma analysis for 3mm,3 % criteria of the coronal plane of the prostate 3 plan and the sagittal and coronal planes of the cerebral 2 case.

As shown in Fig.5.5 and Fig.5.6, for single scan images, the gamma scores of the Mayer protocol show a descending trend for the passing rates and an ascending trend for the mean gamma, while the protocol of Lewis show more stables gamma scores for both, passing rates and mean gamma. In particular, the firsts three dose maps from single scan images show the same behaviour that was found in the first framework, in some cases the protocol of Mayer gives rise to better results and in other cases the protocol of Lewis shows better results. Averaging single scan images and calculating the corresponding dose map or averaging dose maps give rise to a decrease in noise energy. This decrease in noise energy is translated to gamma scores, in general, passing rates are higher and mean gammas are lower, especially when the protocol of Lewis et al is employed.

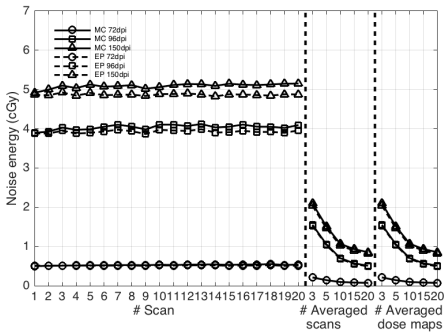

Figure 5.4: Noise energy values of all available dose map

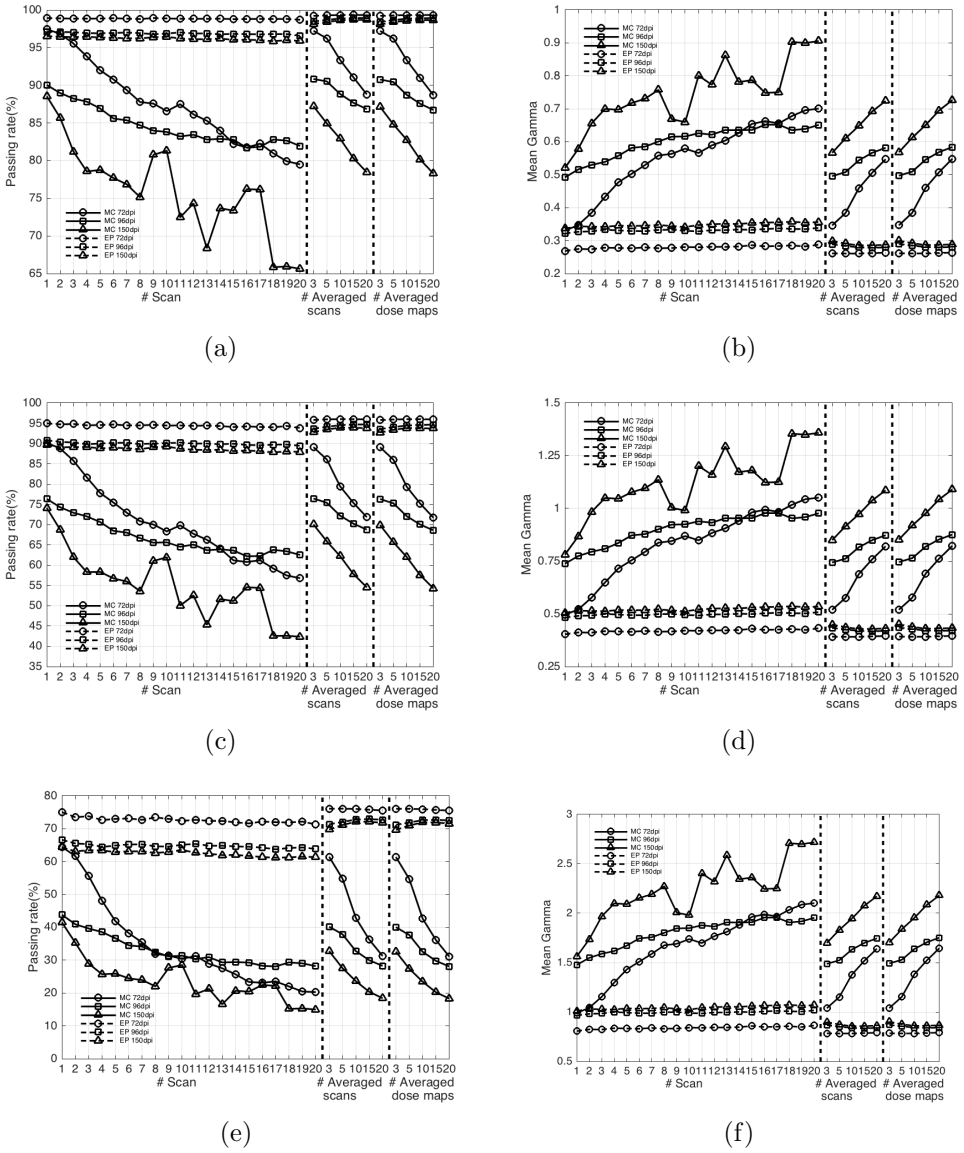

Figure 5.5: Results of gamma analysis of the sagittal plane of the prostate plan: (a) Passing rate for 3mm,3 % criteria (b) mean gamma for 3mm,3 % criteria (c) Passing rate for 2mm,2 % criteria (d) Mean gamma for 2mm,2 % criteria (e) Passing rate for 1mm,1 % criteria (f) Mean gamma for 1mm,1 % criteria

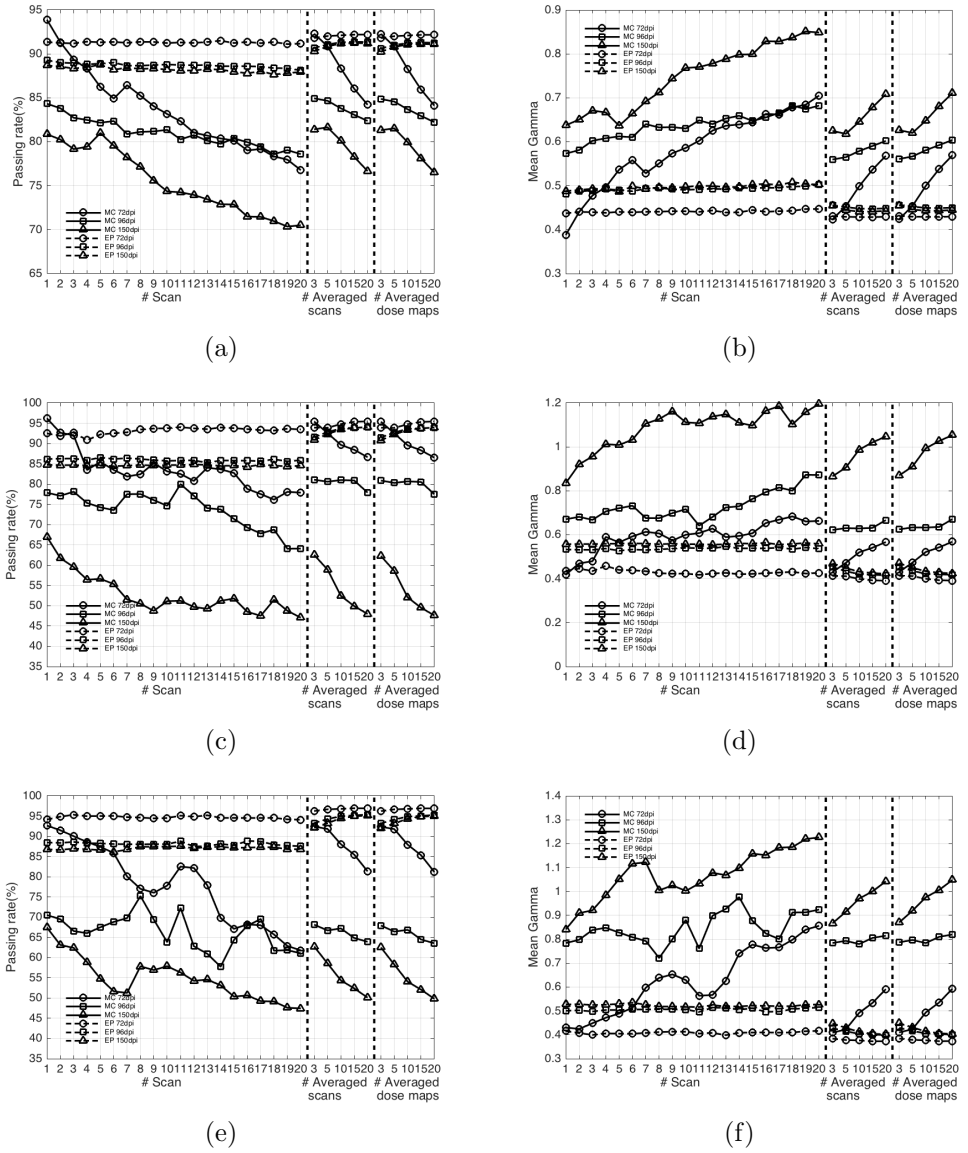

Figure 5.6: Results for gamma analysis 3mm,3 % criteria of: (a) Coronal plane of prostate 3. Passing rate (b) Coronal plane of prostate 3. Mean gamma (c) Sagittal plane of cerebral 2. Passing rate (d) Sagittal plane of cerebral 2. Mean gamma (e) Coronal plane of cerebral 2. Passing rate (f) Coronal plane of cerebral 2. Mean gamma

5.4. Discussion

Accurate RC film dosimetry with a flatbed scanner is a challenge due to all present variabilities. The multichannels algorithms, like the protocols of Mayer et al or Micke et al, partially mitigate intra-scan variabilities. However, more variabilities should be considered for accurate dosimetry with RC films [7]. In particular, the impact of inter-scan and intra-lot variabilities have been raised in this work. The usual workflows, based on the protocols of Mayer et al or Micke et al, use a film for the calibration of the lot, and the other films are used to measure dose distributions in different scanning sessions. This usual workflow is fully affected by inter-scan and intra-lot variabilities, and these variabilities are transferred to both, dose estimations and gamma scores. On the other hand, the protocol of Lewis et al was intended to correct inter-scan and intra-lot variabilities by employing a two level correction. When intra-lot and inter-scan variabilities have been partially mitigated with the protocol of Lewis et al, dose estimations and gamma scores become more robust and reproducible.

It should be mentioned that the comparison between the two investigated protocols based on the value of gamma scores should be made with caution. In daily clinical practice, it has been recommended to minimize the number of scans [3]. In the first framework, an exhaustive warm up of the digitizer is carried out and only three single scans per resolution are considered. Regarding to dose maps from single scanned images, in some dose planes of this first framework, the protocol of Mayer et al gives rise to better gamma scores. However, with these few scans, it is difficult to identify the causes of the different results obtained with the two investigated protocols. Moreover, a decision about the preferred protocol should be based on arguments that take into account the whole picture, not only the gamma scores. In the second framework, twenty scans per resolution are considered. The digitizer response is monitored via the raw pixel values of the two ROIs employed for the two level correction. The raw pixel values in the three channels show a trend over consecutive scans due to inter-scan variability. This trend is transferred to dose estimations obtained with the protocol of Mayer et al, but when the protocol of Lewis et al is considered, dose estimations are quite independent of the trend in raw pixel values, due to the two level correction. This trend in raw pixel values is also observed in averaged images. And, again, dose estimations from averaged scans with the protocol of Mayer et al are affected by this trend. However, when the protocol of Lewis et al is employed, dose estimations are quite stable. In this work, special attention was focused on the gamma analysis procedure. The spatial component of the

gamma index was kept the same for all dose maps corresponding to the same plane. So, differences in gamma scores along the investigated dose maps may be attributed exclusively to changes in dose estimations. At this point the picture is complete, uncorrected digitizer variabilities affect dose estimations and gamma scores. Moreover, uncorrected digitizer variabilities may lead to overestimation and underestimation of passing rates, as demonstrated by our results. In other words, in order to achieve reproducible and accurate results with RC film dosimetry, digitizer variabilities should be always mitigated. The two level correction mitigates intra-lot and inter-scan variabilities. Even with averaged images, the two level correction gives rise to right dose estimations. Finally, the recomendation of minimizing the number of scans [3] for accurate RC film dosimetry may be avoided with the use of the protocol of Lewis et al.

A new approach has been used to quantify noise. This approach is based on the multiresolution approximation of the dose maps. In a multiresolution approximation, approaches of a signal at different scales are determined with a discrete orthogonal basis obtained as dilations and translations of a scaling function. On a discrete signal, this is carried out by a cascade of filter banks. In each step the low pass and high pass filters are applied to the approximation coefficients of a scale and, after subsampling the output, the approximation and detail coefficients of the next scale are obtained. The multiresolution approximation can accurately extract the high frequency noise as the output of the high pass filter in the first step, due to the low frequency nature of dose distributions, inhomogeneities arising from active layer thickness and scanner lateral artifact. High energy noise is then obtained as the detail coefficients of the highest resolution and diagonal orientation of the decimated wavelet transform used in the multiresolution. Regarding the statistical nature of noise in the dose maps, for every dose value, the noise distribution was shown to be Gaussian, as demonstrated by the Jarque-Bera test.Noise reduction by means of time averaging is shown to be efficient once the inter-scan variabilities are compensated. Otherwise, time averaging is worthless due to the importance of these variabilities.

In addition, it should be pointed out that the use of the protocol of Lewis et al, together with time averaging do not affect the accuracy of dose estimations and give rise to a decrease of noise energy present in dose maps. The gamma scores are improved by noise reduction, higher passing rates and lower mean gammas are obtained. In particular, very similar results are obtained when time averaging is employed and noise energies of dose maps have similar values regardless of scanning resolution. Finally, as a recommendation

for saving time in daily clinical practice, averaging images and calculating the dose map with the use of the protocol of Lewis is suggested, as results are very similar to those obtained averaging dose maps from single scanned images.

5.5. Conclusion

The effect of digitizer response variabilities and noise on radiochromic film dosimetry has been studied in this work. For accurate radiochromic film dosimetry, digitizer response variability must be compensated. A new estimation of noise present in dose maps has been provided. The use of the efficient protocol of Lewis et al. has been extended to average images. The intrinsic compensation of present variabilities in radiochromic film dosimetry of the efficient protocol of Lewis et al., together with the time-averaging process and the knowledge of the present noise level leads to an improvement in the radiochromic film dosimetry process. This improvement may be used to extent the working resolutions in treatment verifications without loss of accuracy caused by noise.

[1] S. Devic, N. Tomic y D. Lewis. «Reference radiochromic film dosimetry: Review of technical aspects». En: *Physica Medica* 32 (2016), pp. 541-556.

[2] B. Hartmann, M. Martišíková y O. Jäkel. «Technical Note: Homogeneity of Gafchromic® EBT2 film». En: *Medical Physics* 37.4 (2010), pp. 1753-1756.

[3] B. D. Lynch, J. Kozelka, M. K. Ranade, J. G. Li, W. E. Simon y J. F. Dempsey. «Important considerations for radiochromic film dosimetry with flatbed CCD scanners and EBT GAFCHROMIC® film». En: *Medical Physics* 33.12 (2006), pp. 4551-4556.

[4] A. González-López. «Useful optical density range in film dosimetry: limitations due to noise and saturation». En: *Physics in Medicine & Biology* 52.15 (2007), N321.

[5] D. Lewis y S. Devic. «Correcting scan-to-scan response variability for a radiochromic film-based reference dosimetry system». En: *Medical Physics* 42.10 (2015), pp. 5692-5701.

[6] M. Martišíková, B. Ackermann y O. Jäkel. «Analysis of uncertainties in Gafchromic® EBT film dosimetry of photon beams». En: *Physics in Medicine & Biology* 53.24 (2008), pp. 7013-7027.

[7] S. Aldelaijan, F. Alzorkany, B. Moftah, I. Buzurovic, J. Seuntjens, N. Tomic y S. Devic. «Use of a control film piece in radiochromic film dosimetry». En: *Physica Medica* 32.1 (2016), pp. 202-207.

[8] L. Paelinck, W. De Neve y C. De Watger. «Precautions and strategies in using a commercial flatbed scanner for radiochromic film dosimetry». En: *Physics in medicine & biology* 52.10 (2007), pp. 231-242.

[9] S. Saur y J. Frengen. «GafChromic EBT film dosimetry with flatbed CCD scanner: A novel background correction method and full dose uncertainty analysis». En: *Medical Physics* 35.7 (2008), pp. 3094-3101.

[10] D. Lewis, A. Micke, X. Yu y M. F. Chan. «An efficient protocol for radiochromic film dosimetry combining calibration and measurement in a single scan». En: *Medical Physics* 39.10 (2012), pp. 6339-6350.

[11] R. R. Mayer, F. Ma, Y. Chen, R. I. Miller, A. Belard, J. McDonough y J. J. O'Connell. «Enhanced dosimetry procedures and assessment for EBT2 radiochromic film». En: *Medical Physics* 39.4 (2012), pp. 2147-2155.

[12] A. Micke, D. F. Lewis y X. Yu. «Multichannel film dosimetry with nonuniformity correction». En: *Medical Physics* 38.5 (2011), pp. 2523-2534.

[13] J. F. Pérez Azorín, L. I. Ramos García y J. M. Martí-Climent. «A method for multichannel dosimetry with EBT3 radiochromic films». En: *Medical Physics* 41.6 (2014), 062101-n/a.

[14] I. Méndez, P. Peterlin, R. Hudej, A. Strojnik y B. Casar. «On multichannel film dosimetry with channel-independent perturbations». En: *Medical Physics* 41.1 (2014), 011705-n/a.

[15] S. Mallat. *A Wavelet Tour of Signal Processing: The Sparse way*. 3.ª ed. Academic Press, 2009.

[16] D. L. Donoho y I. M. Johnstone. «Ideal Spatial Adaptation by Wavelet Shrinkage». En: *Biometrika* 81.3 (1994), pp. 425-455.

[17] D. A. Low, W. B. Harms, S. Mutic y J. A. Purdy. «A technique for the quantitative evaluation of dose distributions». En: *Medical Physics* 25.5 (), pp. 656-661.

[18] D. A. Low y J. F. Dempsey. «Evaluation of the gamma dose distribution comparison method». En: *Medical Physics* 30.9 (), pp. 2455-2464.

[19] J. Y. Huang, K. B. Pulliam, E. M. McKenzie, D. S. Followill y S. F. Kry. «Effects of spatial resolution and noise on gamma analysis for IMRT QA». En: *Journal of Applied Clinical Medical Physics* 15.4 (), pp. 93-104.

[20] Y. J. Graves, X. Jia y S. B. Jiang. «Effect of statistical fluctuation in Monte Carlo based photon beam dose calculation on gamma index evaluation». En: *Physics in Medicine & Biology* 58.6 (), p. 1839.

Capítulo 6

Commissioning of the tongue-and-groove modelling in treatment planning systems: from static fields to VMAT treatments.

Phys Med Biol. 2017 Aug 1;62(16):6688-6707

Commissioning of the tongue-and-groove modelling in treatment planning systems: from static fields to VMAT treatments

Víctor Hernández Masgrau[1], Juan Antonio Vera Sánchez[1], Laure Vieillevigne[2] Jordi Saez [3]

[1] *Department of Medical Physics, Hospital Universitari Sant Joan de Reus, IISPV, 43204 Tarragona, Spain*
[2] *Department of Medical Physics, Institut Claudius Regaud-Institut Universitaire du Cancer de Toulouse, 31059 Toulouse, France*
[3] *Department of Radiation Oncology, Hospital Clínic de Barcelona, 08036 Barcelona, Spain*

Adequate modelling of the multi-leaf collimator (MLC) by treatment planning systems (TPS) is essential for accurate dose calculations in intensity-modulated radiation-therapy. For this reason modern TPSs incorporate MLC characteristics such as the leaf end curvature, MLC transmission and the tongue-and-groove. However, the modelling of the tongue-and-groove is often neglected during TPS commissioning and it is not known how accurate it is. This study evaluates the dosimetric consequences of the tongue-and-groove effect for two different MLC models using both film dosimetry and ionisation chambers. A set of comprehensive tests are presented that evaluate the ability of TPSs to accurately model this effect in (a) static fields, (b) sliding window beams and (c) VMAT arcs. The tests proposed are useful for the commissioning of TPSs and for the validation of major upgrades. With the ECLIPSE TPS, relevant differences were found between calculations and measurements for beams with dynamic MLCs in the presence of the TG effect, especially for the High Definition MLC, small gap sizes and the 1 mm calculation grid. For this combination, dose differences as high as 7 % and 10 % were obtained for dynamic MLC gaps of 5 mm and 10 mm, respectively. These differences indicate inadequate modelling of the tongue-and-groove effect, which might not be identified without the proposed tests. In particular, the TPS tended to underestimate the calculated dose, which may require tuning of other configuration parameters in the TPS (such as the dosimetric leaf gap) in order to maximise the agreement between calculations and measurements in clinical plans. In conclusion, a need for better modelling of the MLC by TPSs is demonstrated, one of the relevant aspects being the tongue-and-groove effect. This would improve the accuracy of TPS calculations, especially for plans using small MLC gaps, such as plans with small target volumes or high complexities. Improved modelling of the MLC would also reduce the need for tuning parameters in the TPS, facilitating a more comprehensive configuration and commissioning of TPSs.

6.1. Introduction

It is well known that adequate modelling of the multi-leaf collimator (MLC) is essential for accurate dose calculations in intensity-modulated radiation-therapy (IMRT) treatments involving dynamic MLCs [1, 2]. For this reason, modern treatment planning systems (TPSs) incorporate MLC characteristics such as the leaf end curvature, MLC transmission and the tongue-and-groove.

Transmission through the MLC is defined as a ratio between the doses from an open field and a field with a fully closed MLC. Transmission between leaves (interleaf transmission) is higher than the average transmission due to the thin layer of air between leaves, which reduces the ability of the MLC to shield the beam. Therefore, many MLC models have a 'tongue-and-groove' design, where the sides of adjacent leaves interlock in order to minimise interleaf transmission. However, this arrangement can produce underdosage between adjacent leaf pairs in asynchronous MLC movements due to this region being further shielded by the tongue of opposing leaf sides in different phases of treatment delivery [3]. This underdosage is known as the tongue-and-groove effect (TG effect).

In general, IMRT plans may involve many highly irregular and small MLC apertures and in volumetric-modulated arc therapy (VMAT) individual leaves may repeatedly extend into the radiation field, giving rise to considerable TG effects. Proper modelling of all MLC characteristics is particularly relevant, therefore, in VMAT treatments [4]. Nevertheless, it is difficult for a TPS to fully consider the effects of the beam delivery system [2]. Some investigators [5] have reported that TPS calculations are able to reproduce patterns of dose dips and peaks for a static test field with maximum TG effect. However, the accuracy of the tongue-and-groove modelling in treatments with dynamic MLCs has not been thoroughly investigated.

Since the modelling of tongue-and-groove, rounding of the leaf tips and MLC transmission is essential, these aspects must be considered in the TPS commissioning. Despite that, current guidelines do not include specific tests for the tongue-and-groove, which is often neglected during TPS commissioning [4, 6-8].

The purpose of this study is to evaluate the modelling of the TG effect in TPSs and to provide comprehensible procedures for the commissioning of TPSs regarding this effect. To this aim, the TG effect is characterised and calculations are compared to measurements for (1) static fields, (2) sliding window beams and (3) VMAT arcs. In particular, a novel test that allows a

simple and practical evaluation of both the impact of the TG effect in VMAT treatments and the accuracy of TPS calculations is presented.

6.2. Materials and Methods

This study focuses on the ECLIPSE TPS and Varian linear accelerators. In the subsequent sections we describe the equipment (section 6.2.1), tests (section 6.2.2) and measurements (section 6.2.3) used.

6.2.1. Equipment

Three institutions participated in the study and measurements from four linear accelerators (linacs) were evaluated. The study was mainly conducted in centre A, with 2 linear accelerators: a Varian Trilogy^{TM} equipped with a high definition MLC (HDMLC) and an iX linac with a Millennium120 MLC. For comparison purposes, several tests were repeated for two more linacs from different institutions: a TrueBeam STx system equipped with an HDMLC (centre B) and a 2100CD linac with a Millennium120 MLC (centre C). All experiments were carried out with X-rays with a nominal energy of 6 MV.

The HDMLC consists of 60 pairs of leaves: 32 inner leaves of 2.5 mm width and 28 outer leaves with a leaf width of 5.0 mm defined at the isocentre plane. The Millennium120 MLC also consists of 60 pairs of leaves: 40 inner leaf pairs 5 mm wide and 20 outer leaf pairs of leaves that are 10 mm wide at the isocentre plane. Thus, the maximum field length in the in-plane direction is 22 cm for the HDMLC and 40 cm for the Millennium120 MLC. There are important differences between these two MLC models, such as leaf height, leaf tip curvature and material composition. Detailed information on their exact geometry and characteristics can be found in the literature [9]. For both models the extensions of the tongue (protruding part of half the leaf edge that sticks out into the adjacent leaf) and the groove (stretching of the other half of the leaf edge) are 0.4 mm.

Different versions of the ECLIPSE TPS were evaluated: v13 (centre A), v11 and v13 (centre B) and v10 (centre C). The Analytical Anisotropic Algorithm (AAA) was used, which is an analytical photon dose calculation algorithm based on pencil beam convolution/superposition methods. VMAT plans were also calculated with AcurosXB, which belongs to the class of the

Linear Boltzmann Transport Equation solvers and calculations were renormalised to the corresponding $10 \times 10\,cm^2$ field to minimise differences between algorithms. All calculations were carried out with two calculation grid sizes: 2.5 mm and 1 mm. The 2.5 mm grid was selected because it is commonly used in clinical practice. The grid of 1 mm was evaluated because it is the finest resolution allowed by the TPS and assessing the fine details of the tongue-and-groove structure prompts the use of the smallest available grid size.

The linacs, MLCs, TPSs and calculation algorithms investigated in this study are summarised in table 6.1. All TPSs were commissioned according to international protocols.

Table 6.1: Summary of the equipment used

Centre	Linac	MLC model	TPS	Calculation algorithms
A	Trilogy™	HDMLC	Eclipse 13.5.35	AAA & AcurosXB
A	2300iX	Millennium120	Eclipse 13.5.35	AAA & AcurosXB
B	TrueBeam STx	HDMLC	Eclipse 11.0.31 & 13.7.14	AAA
C	2100CD	Millennium120	Eclipse 10.0.28	AAA

6.2.2. Tests

Three types of tests were devised, involving (1) static fields, (2) sliding window beams and (3) VMAT arcs. The main characteristics of the tests are given in the following subsections and sketched in table 6.2. All DICOM plan files corresponding to these tests will be provided by the authors upon request.

6.2.2.1. Static fields

A combination of two static fields was used to evaluate the case with maximum TG effect. The first field was defined by an MLC where all leaves with even numbers were open while their neighbour leaves (with odd numbers) were closed. The second field consisted of the complementary MLC, with even leaves closed and odd leaves open. Field jaws were set to $12 \times 22\,cm^2$ and $12 \times 32\,cm^2$ for fields with the HDMLC and the Millennium MLC, respectively, in order to include information from leaves of different widths.

Similar MLC patterns have been used in the literature [5, 9]. The interest of this test is that the combination of the two static fields generates a uniform

dose distribution except for the TG effect. As a consequence, a clear pattern is produced with underdosage at the positions corresponding to leaf edges. Thus, this test provides information about the dosimetric consequences of the maximum TG effect caused by the different leaves.

6.2.2.2. Sliding window beams

The sliding window technique involves beams with static gantry and dynamic MLCs. The MLC leaves start at one side of the field and move unidirectionally towards the opposite side while the beam is on. A typical test involving dynamic MLCs is the sweeping gap test, where all leaves are uniformly extended defining a certain gap and move at the same constant speed [10].

Since the sweeping gap test involves uniformly extended leaves, it does not generate any TG effect. To incorporate the TG effect, a shift was applied to the position of adjacent leaves, generating a 'moving fence pattern'. Thus, all leaves with even number were shifted with respect to their neighbour leaves, generating a fence-shaped MLC pattern (as illustrated in table 2). Despite the shift, all leaves moved at the same constant speed, keeping the MLC pattern unchanged. The same gap size was produced by all leaf pairs, but, since leaves are not uniformly extended, this test incorporated a certain degree of TG effect that depends on the value of the shift. Similar tests have been used by other investigators [11, 12]. In the present study this test will be referred to as the asynchronous sweeping gap (a-SG) test.

Table 6.2: Tests used for (a) static fields, (b) sliding window beams and (c) VMAT arcs. The main settings and a sketch of the MLCs used for each test is provided

Tests	MLC
(a) Static test – Static gantry – Sum of two static MLCs Gantry = 0° Collimator angle = 0° X = 10 cm Y = { 22 cm (HDMLC); 32 cm (Millennium) }	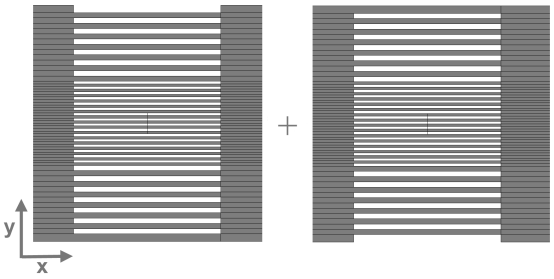
(b) Asynchronous sweeping gap test (a-SG) – Static gantry – Dynamic MLC Gantry = 0° Collimator angle = 0° X = 10 cm Y = { 22 cm (HDMLC); 32 cm (Millennium) } Gaps = 5, 10, 20, 30 mm Several TG fractions	case with gap = 20 mm and TG fraction = 0.5 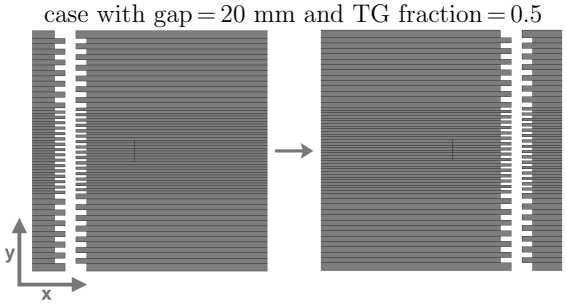 starting position final position
(c) Asynchronous oscillating sweeping gap test (a-OSG) – VMAT arc – Dynamic MLC Gantry = Full rotation Collimator angle = 30° X = 6 cm Y = 8 cm Gaps = 10, 20, 30 mm Several TG fractions	case with gap = 20 mm and TG fraction = 1 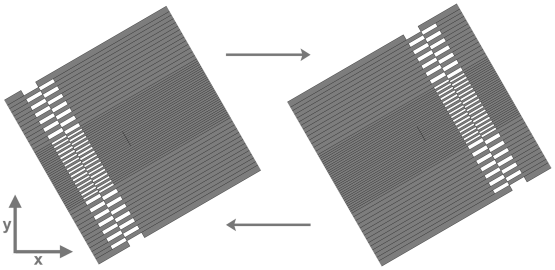 repeated MLC movement during gantry rotation

The files for the a-SG test were created by modifying the DICOM files provided by the manufacturer for the sweeping gap test, where the centre of the MLC gap moves from -6 cm to +6 cm with 13 control points that define the position of the leaves every 10 mm to ensure that the off-axis

correction for the MLC is accurately applied [13]. The field size was the same as used for the static field test and the collimator rotation was kept at 0°. The investigated MLC gap widths were 5, 10, 20 and 30 mm in order to include the range of gaps representative of clinical treatments. For each gap width g, a range of shifts s were evaluated and the tongue-and-groove fraction was expressed as TG fraction $= s/g$. Thus, for TG fraction $= 0$, all leaves are uniformly distributed and there is no TG effect and the higher the TG fraction, the more important the TG effect. The maximum TG fraction varied between 1 and 2 depending on the gap size due to limitations related to the maximum leaf span of the MLC.

6.2.2.3. VMAT arcs

To investigate the TG effect in VMAT treatments we designed a test based on the oscillating sweeping gap (OSG) test presented by [14]. In the OSG test a uniform MLC gap repeatedly moves across the field at a constant speed during a full gantry rotation. Thus, an approximately uniform dose distribution in a cylindrical volume is created, which allows a simple detection of errors in dose calculations. For this reason, the verification of the MLC beam model inside the TPS is one of the potential applications of the test [14]. To this aim, we incorporated the TG effect into the OSG test by introducing a shift between the positions of adjacent leaf pairs as described in the previous section for the a-SG test. This extension of the OSG test will be referred to as the asynchronous oscillating sweeping gap (a-OSG) test.

DICOM plans for this test were generated with an in-house software developed in MATLAB (Mathworks, Massachusetts, USA). Each plan consists of an arc with a gantry rotation between 179° and 181° defined by 178 control points, similar to full arcs from clinical plans. The MLC forms a moving fence pattern that subsequently moves forward and backwards across the field. In particular, the MLC carries out 11 cycles during the gantry rotation from -4.5 cm to +4.5 cm: 6 sweeps in one direction and 5 sweeps in the opposite direction. This code produces VMAT plans where both the gap size and the TG fraction (as defined in the previous section) are selected. The gap sizes investigated were 10 mm, 20 mm and 30 mm and several TG fractions were evaluated for each gap.

All VMAT arcs delivered 700 MU with the maximum dose rate set to 600 MU/min. The same plans (adapted to each MLC model) were used for all linacs, but the resulting dose rate and gantry speed at each control point depended on the maximum gantry speed of the treatment unit. For C-Series

linacs (centres A and C) the gantry moved at its maximum gantry speed of 4.8 deg/s and the dose rate was kept around 560 MU/min. For the TrueBeam system (centre B), configured with a maximum gantry speed of 6 deg/s, the dose rate was fixed at 600 MU/min and the gantry speed remained at about 5.1 deg/s. In all cases the leaves moved at a constant speed of 1.8 cm/s or 1.9 cm/s, depending on the treatment unit. The X jaws were set to 6 cm in order to have the asynchronous MLC gaps completely covering the irradiated volume. The Y jaws were set to 8 cm, including the contribution only from the central thinner leaves. Similarly to clinical arcs, the collimator angle was set to 30°, which spatially distributed the TG effect and the impact of the interleaf transmission.

After creating the DICOM plans, they were imported into the TPS for subsequent calculation and delivery. The treatment couch was included in TPS calculations as a support structure for all plans. Having the collimator rotated during the gantry rotation changes the shape of the volume being uniformly irradiated, which is no longer cylindrical. Indeed, the quasi-uniform dose volume is circular in axial planes, but the radius of this circle diminishes as the axial plane moves away from the isocentre. Thus, an approximately uniform dose distribution is produced with a rhomboid shape in coronal and sagittal planes, which also allows for simple dose measurements.

6.2.3. Measurements and TPS configuration

Both film and chamber measurements – once corrected by daily linac output – were compared to calculations from the TPS. Calculated profiles were compared to those obtained with film dosimetry as described in the next subsection. Calculated average doses were also compared to both chamber measurements and average film doses.

6.2.3.1. Film dosimetry

The dose distributions corresponding to static and a-SG tests were measured using a slabbed RW3 phantom placed at a source-to-surface distance of 90 cm. Films were positioned horizontally at 10 cm depth with 10 cm slabs for backscatter. Measurements were also carried out at 2 cm depth for comparison purposes. The number of MUs was selected to deliver a minimum dose of 80 cGy to the film.

For the a-OSG tests measurements were performed with films placed in

the MultiPlug^{TM} insert of ArcCHECK^{TM} (Sun Nuclear Corp., Melbourne, 225 FL). This is a polymethyl methacrylate (PMMA) cylindrical phantom with a diameter of 15 cm that allows measurement with both film and ionisation chamber. Two slabs of low density polyethylene were cut and used to sustain the MultiPlug^{TM} on the treatment couch by its borders. The centre of the MultiPlug^{TM} was placed at the isocentre, with a source-to-surface distance of 92.5 cm and films were placed in a horizontal plane at the isocentre level. To evaluate the feasibility of using other phantoms for this test, calculations and measurements were repeated using the cubic EASY CUBE phantom (Euromechanics, Schwarzenbruck, Germany).

Radiochromic EBT3 films (ISP, Wayne, NJ) were used. For every film, three pieces of $20.4 \times 3\,cm^2$ were cut and exposed to known doses in order to perform a three point re-calibration as described by [15]. Films were scanned using an Epson 10000XL scanner (Seiko EPSON Corp., Nagano, Japan) at least four hours post-exposure. All the pieces from the same film were aligned to the centre of the digitizer bed in portrait orientation and fixed by a 3 mm-thick sheet of glass. Images were acquired using a 150 dpi resolution in RGB mode with 16 bits per channel and with no colour adjustment and were saved in tiff format. An accurate scanning protocol was followed: firstly the scanner was switched on 30 minutes before use; secondly, a warm up of seven open scans was carried out; and finally, 15 images of every film with the same frame were acquired leaving two minutes between consecutive scans. All images from the same film were averaged in order to remove temporal noise and dose maps were obtained from the average images with multichannel dosimetry following the efficient protocol by [15]. This method provides noise reduction without losing accuracy, as described in a recent work by [16] and it is recommended when a high resolution is desired.

Finally, in-plane profiles were extracted from the dose maps and mean doses in the central $2 \times 2cm^2$ region of interest were obtained. Profiles from the static and the a-SG tests were averaged in the cross-plane direction over a region of 1 cm in order to achieve a higher noise reduction by taking advantage of the symmetry of the dose distribution in that direction. To avoid spatial distortion, no filter was applied to images or dose maps; only time averaging (multiple scans) and spatial averaging along the cross-plane direction were considered as de-noising techniques.

6.2.3.2. Ionisation chamber

Dose measurements were carried out using a Farmer-type ionisation chamber positioned at the isocentre along the Y axis, that is, perpendicular to the MLC movement direction with the collimator angle set to 0°. The PTW chamber model 30013 was used, with an active length of 23 mm and an active volume of 0.6 cm^3. This chamber was selected because its active length spanned several leaves, providing an estimate of the average impact of the TG effect.

The static and a-SG tests were measured at 10 cm depth in a (1) water phantom and (2) RW3 plastic phantom for comparison with TPS calculations and film measurements, respectively. Measurements for VMAT (a-OSG test) were performed using the Farmer chamber placed at the centre of the cylindrical PMMA phantom described in the previous section. Chamber readings were corrected for the daily output variations of the linacs and differences between TPS calculations and measurements were calculated as (D_{TPS} - $D_{measured}$)/$D_{measured}$.

6.2.3.3. MLC modelling and configuration in the ECLIPSE TPS

Two user-definable parameters are required during commissioning of the ECLIPSE TPS: the MLC transmission and the dosimetric leaf gap. The TPS uses a single value for transmission that is determined as the ratio of the measured average dose in an open field and the measured average dose for the same field size with the MLC closed. Thus, the TPS considers only the average transmission, without taking into account the higher interleaf transmission, modifications in the energy spectrum of the beam or any variation between leaves of different width.

The dosimetric leaf gap parameter is used by ECLIPSE to model the higher transmission through the rounded leaves of the MLC. To this aim, the actual fluence used for dose calculations is computed considering a shift in the leaf positions. In particular, leaves are pulled back by half the value of the dosimetric leaf gap, so that the gap between a fully closed leaf pair equals the dosimetric leaf gap parameter.

The tongue-and-groove is also modelled in the TPS by modifying the actual fluence. In MLC-defined fields, the lateral sides of some leaves effectively limit the beam and the exposed tongues from those leaves modify the delivered fluence by blocking some additional radiation. This effect is modelled

by extending the leaf projection in the direction perpendicular to the leaf motion by a certain tongue width; thus, the tongue width is subtracted from the delivered fluence [17]. This parameter is not configurable in ECLIPSE and is set to 0.3125 mm, slightly smaller than the real tongue width [18]. The groove also modifies the fluence, but that effect is much smaller and is not modelled in the TPS. As a consequence, the field size in the direction of leaf movements is enlarged by the dosimetric leaf gap, while in the perpendicular direction it is reduced due to the tongue width by 0.625 mm (0.3125 mm for each limiting leaf side).

Configuration of calculation algorithms in ECLIPSE also includes the parameters effective spot size (ESS) in the X and Y directions of the collimator coordinate system. These parameters modify the calculated penumbra by applying a Gaussian smoothing to the energy fluence of primary photons [17]. In consequence, manual tuning of the ESS in the X and Y direction can be used to adjust the output factor for small MLC apertures and the penumbra width [19]. For the AAA algorithm and MLC-shaped beams from Varian treatment units, the recommended ESS values are 1 mm and 0 mm for X and Y directions, respectively. However, the ESS in the Y-direction (the direction of the tongue width) was considered potentially relevant and was investigated in the present study. To this aim, calculations were also carried out with the AAA algorithm setting the ESS in the Y direction to 0.5 mm and 1 mm.

6.3. Results

6.3.1. Static fields

The results obtained for the combination of the two static fields with complementary MLCs are shown in 6.1, where measured and calculated in-plane profiles (along the y axis) are given. Profiles measured with film clearly show the underdosage produced by the TG effect in the interleaf regions. For both MLC models this underdosage is more pronounced in the central part of the field. This can be explained because the central leaves are thinner than the outer leaves, hence increasing the number of dose dips and therefore the overall TG effect. As already described by [3] and [20] as depth increases the dose profile is smoothed, with more rounded and wider dose dips due to electron transport.

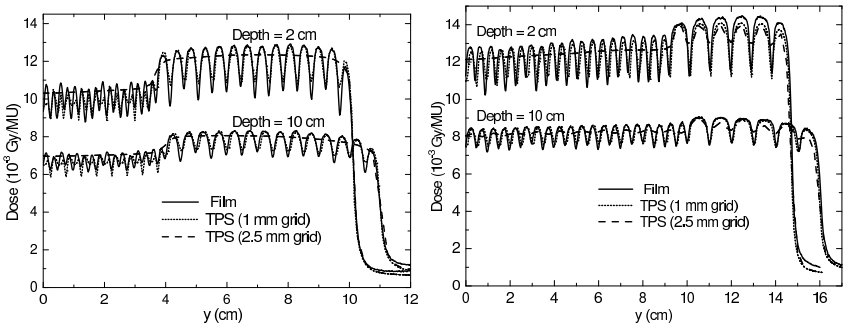

Figure 6.1: Experimental and calculated profiles obtained for the static test with (a) HDMLC and (b) Millennium MLC.

TPS calculations with the 1 mm grid show good agreement with film dosimetry, indicating that the TPS accurately models the TG effect in this situation regardless of the depth. TPS calculations with the 1 mm grid reproduce the dose profile measured with film in detail, although a finer resolution would be necessary to accurately sample the thinner leaves of the HDMLC [21]. On the contrary, TPS calculations with the 2.5 mm grid cannot replicate the variations produced by the TG effect in any of the cases evaluated, because this resolution is excessively low.

Measurements with the Farmer ionisation chamber were also carried out at the centre of the beam and compared to film doses and TPS calculations. To verify that the chamber provided a good estimate of the average dose, measurements were repeated for different chamber positions. Thus, positioning shifts between 1 mm and 5 mm were evaluated for both lateral and longitudinal directions. In all cases results were within $\pm 0.2\,\%$ regardless of the chamber position. Average doses from film were computed by averaging over a $2 \times 2\,\mathrm{cm}^2$ region. Good agreement was found between film dosimetry and the ionisation chamber measurements, with deviations $<1\,\%$, which validates the followed procedure.

To compute the average calculated dose, a cylindrical structure simulating the Farmer chamber was defined in the TPS (diameter = 6 mm, length = 22.5 mm) and the mean dose to the structure was obtained. In general, a good agreement was found between average calculated and measured doses except for the central leaves of the HDMLC. For these leaves, average doses calculated with the 2.5 mm grid were 5.5 % higher than those obtained with the 1 mm grid. In particular, the TPS underestimated the average dose with

respect to measurements by 1.5 % for the 1 mm grid and overestimated it by 4.0 % for the 2.5 mm grid. For the the outer leaves of the HDMLC the difference between average doses calculated with both grids was about 2 % and for all the leaves of the Millennium MLC differences were <1 %.

Since the position of the calculation grid could also have an impact on the calculated doses, TPS calculations were repeated at slightly different positions of the calculation grid. No differences in the calculated dose were found for the 2.5 mm grid. For the 1 mm grid dose differences as high as 5 % were found at some points near steep dose gradients; however, average doses obtained as mean doses to the cylindrical structure were practically not affected by the position of the calculation grid, with deviations <0.2 %.

6.3.2. Sliding window beams

Figure 2 shows the profiles obtained with film dosimetry for the sweeping gaps of 5 mm and 10 mm at 10 cm depth for different TG fractions, together with the profiles calculated by the TPS for both the HDMLC and the Millennium models.

In absence of tongue-and-groove –figures 2(a) and 2(b)– good agreement between measurements and calculations was found. Film dosimetry profiles show a pattern of alternate peak and valley doses due to the higher interleaf transmission, while calculated profiles are flat because the TPS only takes into account the average transmission. This effect is more evident for smaller gaps because the smaller the gap, the lower the Gy/MU and the higher the contribution of MLC transmission. It can also be seen that the measured profile is slightly lower for the outer leaves than for the inner leaves. This difference can be explained by the off-axis reduction of transmission [22] and the lower average transmission of the outer leaves. In this case, no difference was found between the profiles calculated with grids of 1 mm and 2.5 mm.

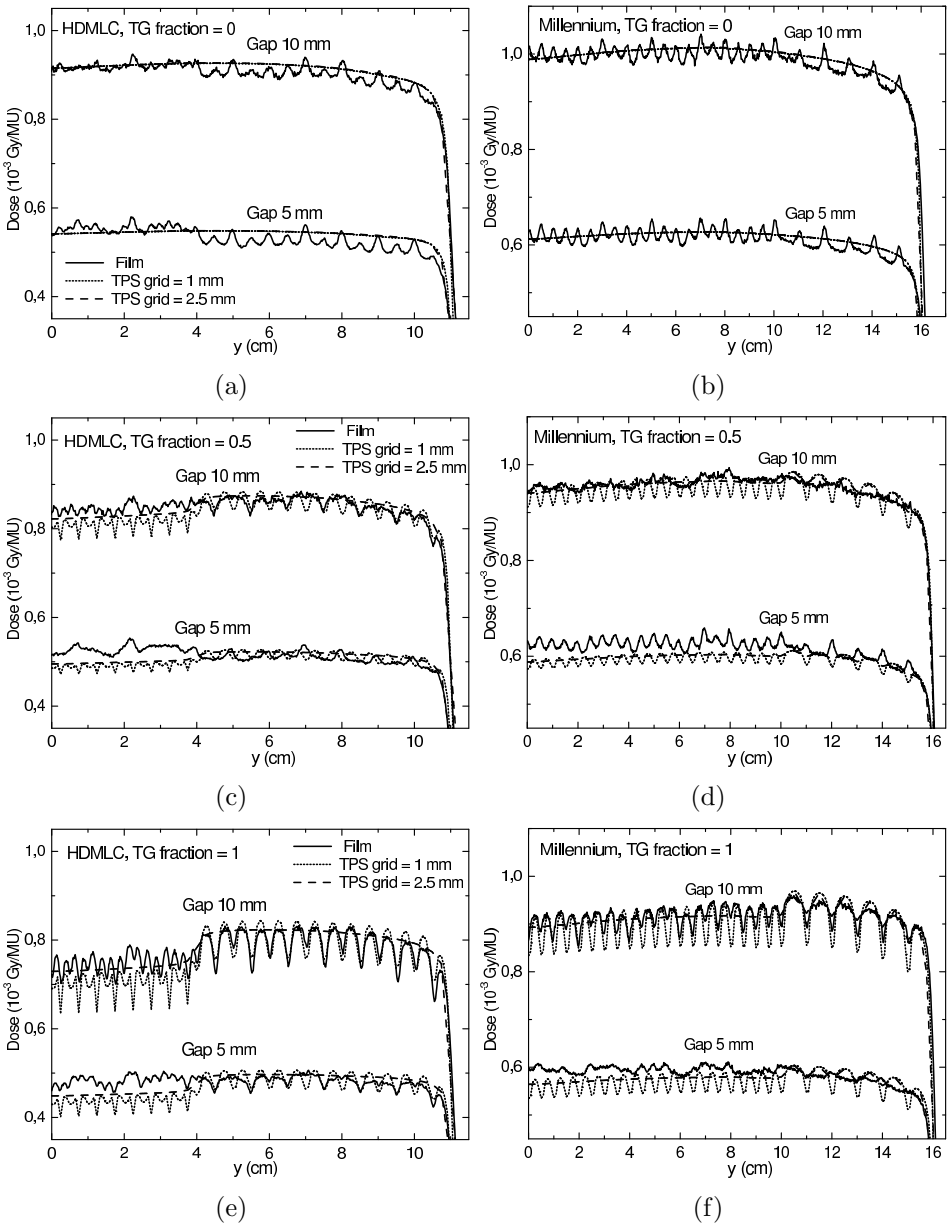

Figure 6.2: Experimental and calculated profiles obtained for the a-SG test for dynamic gaps of 5 mm and 10 mm at 10 cm depth. Results for the HDMLC (a,c,e) and the Millennium MLC (b,d,f) are shown as a function of the TG fraction.

For half the gap with tongue-and-groove (TG fraction = 0.5, see figures 2(c) and 2(d)), average doses were reduced by the TG effect, especially in the central part of the beam, where the leaves are thinner and therefore

the incidence of the TG effect is higher. For small gaps the peak-to-valley variations are low because the TG effect and the interleaf transmission tend to cancel out [10]. Indeed, the TG decreases the dose between leaves, while interleaf transmission has the opposite effect. The TPS underestimates the dose for the inner leaves, especially when the 1 mm calculation grid is used. Interestingly, for the sweeping gap of 5 mm with the Millennium MLC (and also for the outer leaves of the HDMLC) the film profile shows a pattern of peak-to-valley doses opposite to that calculated by the TPS. The reason for this behaviour is that in this case the interleaf transmission actually dominates over the TG effect, but it is not properly accounted for by the TPS.

Figures 2(e) and 2(f) show the profiles for the situation where the full gap suffers from TG effect (TG fraction = 1), that is, when the separation between adjacent leaves equals the size of the gap. In this case both the reduction in the average dose and the peak-to-valley variations are more pronounced due to the higher TG effect. Similarly to TG fraction = 0.5, TPS calculations clearly underestimate the dose in the central part of the beam, remarkably for the 1 mm grid.

Figure 3 shows the results for the sweeping gap of 20 mm at 10 cm depth. As expected, the peak-to-valley dose variations are larger than those found for the gaps of 5 mm and 10 mm, because the larger the gap, the lower the contribution of the MLC transmission and the more evident the TG effect. Having different TG fractions included in the same figure clearly illustrates the average dose reduction introduced by the TG effect. For the HDMLC model this reduction was about 10 % (TG = 0.5) and 23 % (TG = 1), irrespective of the depth. For the Millennium model the average dose reduction was lower, about 5 % for TG = 0.5 and 11 % for TG = 1, because the leaves are twice as wide and therefore the TG effect is approximately halved. The TPS is able to approximately reproduce the dose reduction due to the TG effect. However, it tends to overestimate this dose reduction, especially for the thinner leaves and for the 1 mm calculation grid.

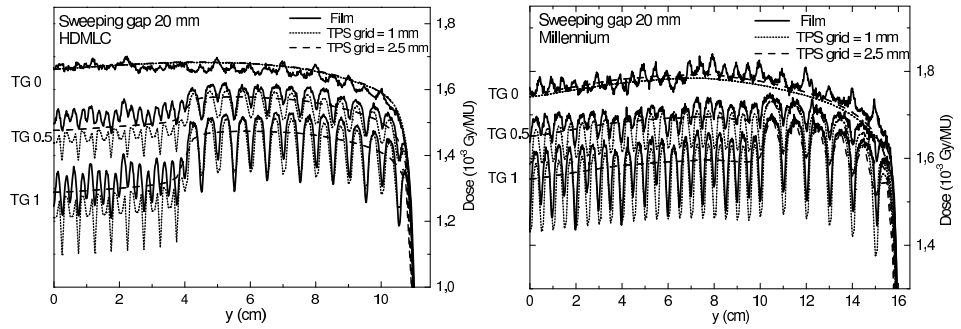

Figure 6.3: Experimental and calculated profiles obtained for the a-SG test with the (a) HDMLC and (b) Millennium MLC. Results for the dynamic gap of 20 mm at a depth of 10 cm are shown for TG fractions of 0, 0.5 and 1.

Film dosimetry measurements and calculations were also performed at a depth of 2 cm. The peak-to-valley variations produced by the TG effect were smoothed with depth due to scatter and electron transport. Curves are not shown, but the behaviour was very similar to the static case illustrated in 6.1. Profiles were also measured and calculated at off-axis distances, but no differences were found. Tests were also carried out for MLC gaps sweeping a shorter distance (from -3 cm to $+3$ cm) and only slight differences were observed, associated to the smaller effect of the MLC transmission.

Finally, measurements were also performed with a Farmer ionisation chamber in order to determine the mean dose in the central part of the beam. The sensitive volume of this chamber should average the peaks and valleys produced by the TG effect and provide a good estimate of the mean dose. This was experimentally verified by repeating measurements after introducing longitudinal shifts in the chamber position (range 1-5 mm with 1 mm step) and variations in the chamber readings were $<0.2\,\%$.

Average calculated doses were, again, obtained as the mean dose in the cylindrical structure simulating the chamber. Figures 4(a) and 4(b) show the measured and calculated average doses for the a-SG test. The MLC gap sizes studied were 5, 10, 20 and 30 mm, and for each gap size several TG fractions were evaluated. As the TG fraction was increased, the average dose was progressively decreased, until full TG was achieved. The maximum TG effect occurred for TG fractions slightly over 1, due to the influence of the rounded leaf ends. TPS calculations approximately reproduced the dose reduction due to the TG effect, but some discrepancies appeared. For TG fraction $= 0$

a very good agreement was found, with differences <0.5 %. This was expected because the dosimetric leaf gap was measured and the TPS was commissioned precisely in these conditions (without the TG effect). However, as the TG fraction increased, TPS calculations progressively underestimated the dose, notably for the 1 mm grid size. This trend was reversed for TG fractions >1, where calculated doses remained constant while measured doses kept slightly decreasing.

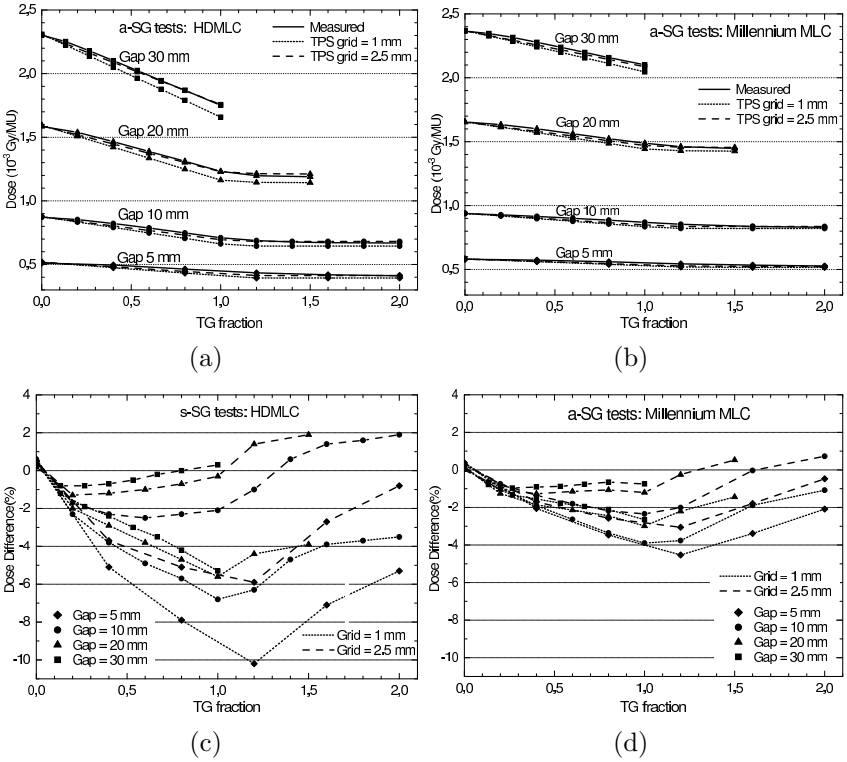

Figure 6.4: Experimental and calculated average doses for the a-SG test for dynamic gaps of 5, 10, 20 and 30 mm. Results for the (a) HDMLC and the (b) Millennium MLC are given as a function of the TG fraction. Difference between calculations and experiments are given for the (c) HDMLC and the (d) Millennium MLC.

Dose differences given in figures 4(c) and 4(d) clearly illustrate the tendency of the TPS to underestimate the average dose. In general, dose differences do not show a linear trend: they progressively increase as the TG fraction augments from zero to one and are gradually reduced for TG fractions greater than one (i.e., when intergitation between leaves from opposed banks occurs). Dose discrepancies for the HDMLC are approximately a factor 2 larger than those found for the Millennium MLC. This can be explained

because the incidence of the TG effect is higher for the HDMLC and limitations in the TPS modelling will also have a greater effect. The MLC gap size and the calculation grid also have a great impact on dose discrepancies. Indeed, deviations for the 1 mm grid are much larger than those obtained for the 2.5 mm grid and the smaller the MLC gap, the larger the dose differences. Remarkably, the most adverse combination was the HDMLC with a 5 mm gap calculated with a 1 mm grid, which produced a dose difference as high as 10 % .

The potential impact of the effective spot size (ESS) parameter in the Y direction was investigated. Increasing the parameter from 0 to 1 mm produced a progressive smoothing of the dose distribution in that direction. Thus, peak-to-valley variations in dose profiles along the Y direction were reduced by up to 50 % when the ESS was increased from 0 to 1 mm. We found that the dose profiles measured with film dosimetry were reproduced much better by the TPS with ESS = 0 mm in the Y direction, which agrees with the manufacturer's recommendation. However, modifying the ESS parameter had no impact on the average doses, with all differences <0.1 %. Therefore, the dose discrepancies shown in figures 4(c) and 4(d) remained unaltered. This was expected, because the spot size has a blurring effect on the primary fluence but should not alter average doses.

6.3.3. VMAT arcs

The a-OSG tests described in section II.B.3 were carried out for the MLC gaps of 10, 20 and 30 mm and for several TG fractions. Figure 5 shows the calculated dose distribution obtained for the HDMLC, 20 mm gap and TG fraction = 1 together with the corresponding dose distribution measured with film. This test produced very homogeneous dose distributions, even in the presence of TG effect. Indeed, film dosimetry showed dose variations around ±2 % and measurements with the ionisation chamber placed in different positions revealed differences in average doses within ±0.4 %. In the presence of the TG effect TPS calculations show a certain granularity in the dose distribution that might be interpreted as calculation artifacts produced by the limited angular resolution or by the finite grid size. However, this is not the case because film dosimetry also reveals the same effect, showing that the granularity is actually produced by the TG effect, which does not completely smear out during the gantry rotation.

It can also be observed in figures 5(a) and 5(c) that the dose distribution

along the gantry rotation axis is slightly less homogeneous than at the rest of the central homogeneous region sketched in figures 5(a) and 5(b). This is because in this axis the projection of the leaf edges coincides at the same points regardless of the gantry angle and the TG effect and interleaf transmission do not smear out during the gantry rotation. For this reason we analysed the profiles along a line shifted 5 mm in the x direction, as indicated in figure 5(c).

Plans were calculated at gantry angle intervals of approximately 2 deg, which is the configuration used in clinical practice. To evaluate the potential effect of limited angular resolution, some calculations were also carried out every 1 deg, but no relevant differences were observed.

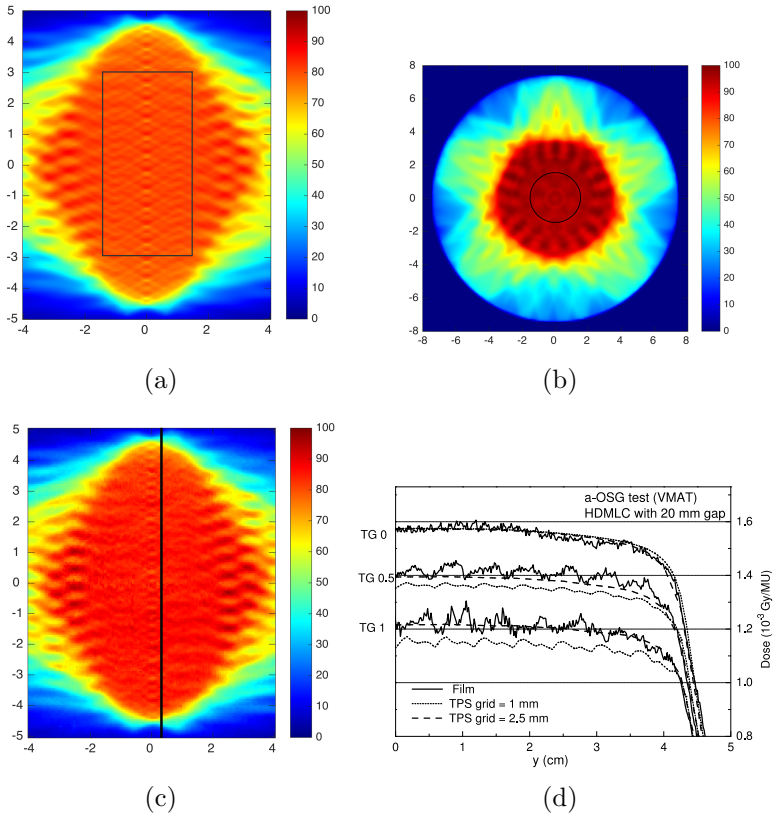

Figure 6.5: Dose distributions for the a-OSG test with the HDMLC and the 20 mm gap. The calculated distribution at the isocentre level for TG fraction = 1 is illustrated in the (a) horizontal plane and (b) axial plane. The distribution measured with film dosimetry is shown in (c). In (d) dose profiles along the straight line depicted in (c) are given for TG fractions 0, 0.5 and 1. The central region of the quasi-uniform dose region is shown in (a) with a rectangle 6 cm high and 3 cm wide and in (b) with a circle of diameter of 3 cm.

Measurements were also performed with the Farmer ionisation chamber placed in the centre of the cylindrical phantom. As shown in 6.6, good agreement was found for the average doses in the absence of TG the effect (TG = 0), while dose discrepancies progressively increased as the TG fraction was raised. Similarly to the results from the sweeping gap tests, discrepancies were larger for the HDMLC, small gaps and the 1 mm grid. For the combination of HDMLC, 10 mm gap (which was the smallest gap evaluated for VMAT) and 1 mm grid, the TPS was found to underestimate the dose by 7.4 %. This discrepancy is compatible with the result of −6.8 % obtained for the same combination with the a-SG test.

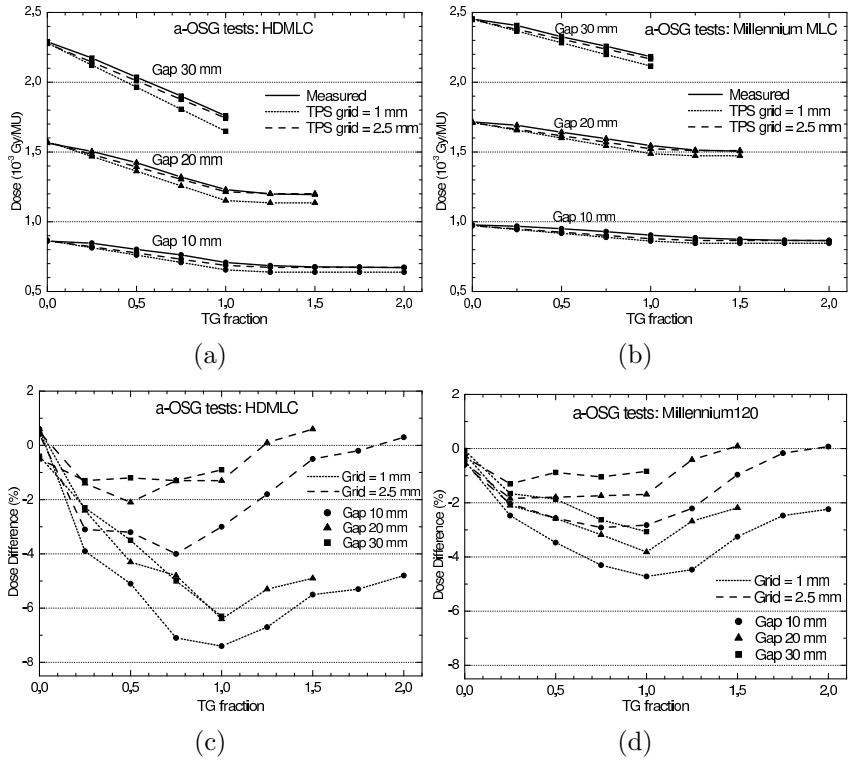

Figure 6.6: Experimental and calculated average doses for the a-OSG test for gaps of 10, 20 and 30 mm. Results for the (a) HDMLC and the (b) Millennium MLC are given as a function of the TG fraction. Difference between calculations and experiments for the HDMLC and the Millennium MLC are given in (c) and (d), respectively.

The cylindrical PMMA phantom was used in order to take advantage of the cylindrical symmetry of the a-OSG test about the gantry rotation axis and achieve a quasi-uniform dose distribution. However, measurements were repeated with the EASY CUBE phantom and the homogeneity of the

dose distribution at the center region remained practically unaltered. As a consequence, other phantoms, not necessarily cylindrical, can be used for the a-OSG tests.

For comparison purposes, VMAT calculations were also carried out with the AcurosXB algorithm implemented in ECLIPSE. After renormalising to the corresponding 10 x 10 cm2 field, discrepancies between the algorithms AcurosXB (for both "dose to water.ªnd "dose to medium") and AAA disappeared, with differences <0.3 %. As a consequence, the dose differences obtained for the AAA algorithm as a function of the TG fraction are also valid for the AcurosXB algorithm.

6.3.4. Other centres

To verify that similar results could be reproduced with other implementations of the ECLIPSE TPS and different beam data the proposed tests were also carried out in additional linacs from other institutions (table 1). Thus, the following systems were evaluated: (a) TrueBeam STx equipped with an HDMLC and ECLIPSE v11.0 and v13.7 and (b) Clinac 2100CD with a Millennium MLC and ECLIPSE v10.0. The results obtained for the a-SG tests are given in figure 6.7. Dose differences corresponding to the a-OSG tests were also similar to those from the a-SG tests and so are not shown.

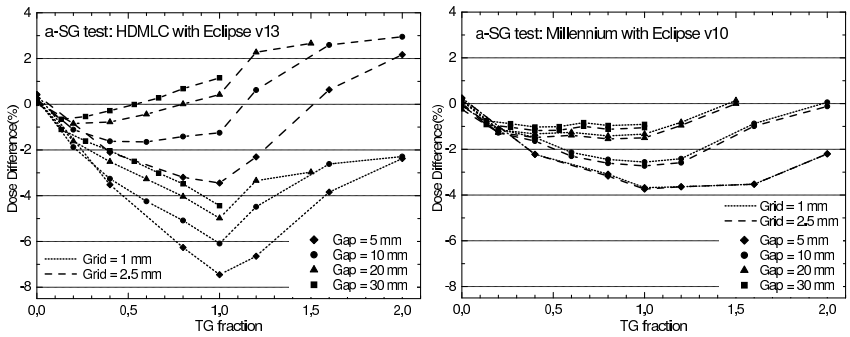

(a) (b)

Figure 6.7: Experimental and calculated average doses for the a-SG test for gaps of 5, 10, 20 and 30 mm. Differences between calculations and experiments corresponding to the a-SG test are given as a function of the TG fraction for (a) HDMLC and Eclipse v13 (centre B) and (b) Millennium MLC and Eclipse v10 (centre C)

Dose differences for the TrueBeam system with an HDMLC and Eclipse

v13.7, illustrated in figure 7(a), were similar to those found for the same MLC and ECLIPSE v13.5. Again, results greatly differed depending on the size of the calculation grid, with much larger discrepancies between calculations and measurements for the 1 mm grid. In this case, differences in average doses as high as −7.5 % and −6.1 % were found for the 5 mm and the 10 mm gaps, respectively. Only data from ECLIPSE v13.7 is shown because version 11.0 produced practically the same results.

The Clinac 2100CD with a Millennium MLC and ECLIPSE v10, on the contrary, behaved differently from the same MLC and ECLIPSE v13 (see figures 7(b) and 4(d)). Indeed, with ECLIPSE v10 only slight differences around 0.2 % were found between the calculation grids of 1 mm and 2.5 mm. Dose discrepancies between calculations and measurements with version 10 were in between those found for the two grid sizes with ECLIPSE v13, with maximum differences of 3.7 % and 2.7 % for the 5 mm and the 10 mm gaps, respectively.

6.4. Discussion

6.4.1. Proposed tests and TPS commissioning

We have demonstrated that, in order to properly calculate the dose patterns produced by the TG effect, TPSs should incorporate modelling of the interleaf transmission. However, since the TG effect from multiple beams (or arcs) tends to smear out, the most relevant quantity is the average dose.

All the proposed tests are suitable for measurements with ionisation chambers or film dosimetry. Film dosimetry provides detailed information about the spatial distribution of dose deposition, which is crucial to properly characterise the TG effect due to its geometric and spatially distributed nature. Additionally, ionisation chambers with a large active volume are recommended for obtaining the average dose delivered by several leaves, which is the most important quantity in clinical treatments. Thus, one of the relevant results of this study is that an ionisation chamber can be used not only for measuring the dosimetric leaf gap and the MLC transmission, but also for evaluating the TPS modelling of the TG effect. Actually, using a chamber with a large sensitive volume (such as a Farmer-type chamber) is even beneficial because it spatially averages small dose inhomogeneities, providing a robust determination of the mean dose.

The tests proposed in this study allow evaluation of the TPS modelling of the tongue-and-groove. Hence, they can be used for the commissioning of TPSs and also for the validation of TPS upgrades, although there is no consensus on the acceptance level that should be used. Recent Practice Guidelines from AAPM [8] recommend that average differences between TPS and measurements with ionisation chambers should not exceed 2 % in low-gradient target regions produced by IMRT treatments. Our results show that these recommendations may not be fulfilled, even in quasi-homogeneous dose distributions, due to limitations in the modelling of the TG effect in the TPS. Thus, agreement within ±2 % would be desirable but, to this aim, improved modelling of the MLC is necessary.

It is worth highlighting that, although we focused on the Varian solution (ECLIPSE TPS and Varian linacs), the tests proposed can be applied to any TPS and linac combination. In particular, in TPSs where the value of the tongue-and-groove width can be configured [23], these tests can also be used to obtain the optimal value for this parameter.

6.4.2. Results

For the static test, as already reported by [5], TPS calculations with the 1 mm grid agreed well with measurements and were capable of reproducing the pattern of dose dips and peaks. This test is independent of the leaf gap setting, but it reflects a situation of static MLC with maximum leaf aperture and maximum TG effect that it is not representative of the fields used in clinical practice.

On the contrary, the a-SG and a-OSG tests evaluate dynamic MLCs and cover a wide range of MLC gap sizes and TG fractions similar to those used in clinical treatments. In the presence of the TG effect both film dosimetry and ionisation chambers, which agreed to within 1 %, exposed some relevant dose differences between calculations and measurements, especially for the inner leaves. The fact that differences between calculations and measurements did not show a linear trend indicates inadequate modelling of the tongue-and-groove rather than only a non-optimal setting of the tongue width within the TPS. Indeed, any change in the tongue width would, in principle, produce a change in the slope of the calculated curves shown in figures 4(a), 4(b), 6(a) and 6(b). This parameter is not user-configurable in ECLIPSE, but such a change would not completely eliminate the discrepancies obtained.

In general, we found that the smaller the MLC gap, the larger the dose difference. A possible explanation is that limitations of the tongue-and-groove modelling in the TPS originate a certain error in the calculated fluence that will have a higher relative impact on small gaps. These differences can provide insight into dosimetric discrepancies related to the use of small MLC gaps in dynamic treatments [24, 25].

It was surprising to find differences of up to 5 % between average doses calculated with different grid sizes with both ECLIPSE v11 and v13, even in the homogeneous dose distributions produced by the a-OSG tests. It is known that changing the grid size may affect the calculated dose, especially for small fields, small MLC apertures and in regions with high dose gradients [26]. However, the mean and the integral dose (i.e., the total energy deposited) should not depend on the grid size [18]. In the absence of the TG effect, calculations for the a-OSG tests with both grid sizes agreed, while discrepancies increased as the TG fraction increased. This clearly indicates a problem in the TPS that could be overlooked without these tests. Investigating the exact cause of these differences is beyond the scope of this study. However, it has been seen that grid alignment can cause sampling errors that could affect the calculated dose [21]. Differences might also be associated to the unified fluence calculation implemented in version 11 of ECLIPSE, which would explain why in ECLIPSE v10 calculations with both grid sizes agreed to within ±20.2 % in all cases (figure 7(b)).

The results for AcurosXB were practically identical to those obtained for the AAA, with average dose differences lower than 0.3 %. Accuracy of ECLIPSE TPS calculations is affected by both the source model –that includes the modelling of the MLC– and the dose deposition algorithm, which is responsible for radiation transport and conversion to absorbed dose. Our results indicate that, although their dose deposition engine is totally different, both algorithms use the same MLC modelling and suffer from the same limitations regarding the TG effect.

Two additional centres carried out the tests and obtained similar results, which would rule out the possibility of problems related to a particular implementation or configuration of the TPS.

6.4.3. Clinical implications and considerations

In the present study we have reported some important discrepancies between calculations and measurements that can clearly yield clinical conse-

quences in certain situations. Although in clinical plans with dynamic MLCs the TG effect is spatially smeared out, the average dose is underestimated by the TPS, as we confirmed with the a-OSG tests. However, the ECLIPSE TPS has been thoroughly validated and it is well established that it offers satisfactory dose calculations for IMRT/VMAT treatments, including SBRT treatments [27, 28]. Recently it has also been shown that ECLIPSE offered acceptable characteristics for stereotactic small fields provided adequate tuning of configuration parameters is performed [19].

The apparent discrepancy between our results and those reported in the literature can be explained in two ways. Firstly, clinical plans involve continuous distributions of MLC gaps and TG fractions; therefore, the dose differences found in the proposed tests will be averaged and might partially cancel each other out. Secondly, configuration parameters in TPSs are often tuned in order to maximise agreement between measurements and calculations in clinical plans, which might mask the problem. Indeed, systematic differences introduced by inadequate MLC modelling in the TPS may be partially compensated by tuning parameters in the TPS, providing better agreement between calculations and measurements for typical clinical plans. For instance, incrementing the dosimetric leaf gap will increase the doses calculated by the TPS and the smaller the MLC gap, the higher the dose increase. Hence, tuning the dosimetric leaf gap can be a rather effective method to compensate for the underestimation of the calculated doses produced by inadequate modelling of the TG effect.

[25] reported the need to tune the dosimetric leaf gap parameter in the ECLIPSE TPS for dynamic treatments involving small MLC gaps, especially for the HDMLC, although the reasons were not identified. Our study supports their results and explains the need for tuning configuration parameters in the TPS. However, these parameters will not be optimal for all plans and compensations might not work in certain cases [12]. In our opinion, improving the MLC modelling will both increase the accuracy of the TPS and reduce the need for tuning configuration parameters.

Our study reveals some limitations in the tongue-and-groove modelling within the ECLIPSE TPS and raises concerns about the accuracy of calculations with the 1 mm grid in certain situations, but it does not invalidate the clinical applicability of the TPS. Some investigators have reported improved accuracy for calculations with ECLIPSE when the finer 1 mm grid is used [26]. Again, this work does not conflict with that, because our study focused on the TG effect, and overall accuracy in clinical plans was not addressed. Nevertheless, the combination involving the HDMLC and the 1 mm grid is

typically used for small target volumes and plans with high complexities, which are also associated to small MLC gaps [24]. Since this was the combination yielding the largest discrepancies, we believe that in these cases the limitations reported in the present study are especially relevant and should be carefully evaluated.

6.5. Conclusions

In this study we have characterised the dosimetric consequences of the tongue-and-groove effect and we have presented comprehensive tests to evaluate the ability of TPSs to accurately model this effect. The tests proposed can be useful for the commissioning of TPSs and for the validation of major upgrades. Relevant differences between calculations and measurements for beams with dynamic MLCs in the presence of the TG effect were found for the ECLIPSE TPS, especially for the HD120 MLC, small gap sizes and the 1 mm calculation grid.

In conclusion, there is a need for better modelling of the MLC by TPSs, and one of the relevant aspects is the tongue-and-groove. In our opinion, this will improve the accuracy of TPS calculations, particularly for highly modulated plans or those with small target volumes, which involve small MLC gaps and are especially challenging to calculate. In addition, improved modelling of the MLC would greatly reduce the need for tuning parameters in the TPS, facilitating a more comprehensive configuration and commissioning of TPSs.

[1] F. Lorenz, A. Nalichowski, F. Rosca, J. Killoran, F. Wenz y P. Zygmanski. «An independent dose calculation algorithm for MLC-based radiotherapy including the spatial dependence of MLC transmission.» En: *Physics in Medicine and Biology* 53.3 (2008), pp. 557-573.

[2] J. S. Li, T. Lin, L. Chen, R. Price y C.-M. Ma. «Uncertainties in IMRT dosimetry.» En: *Medical Physics* 37.May (2010), pp. 2491-2500.

[3] J. Deng, T. Pawlicki, Y. Chen, J. Li, S. B. Jiang y C. M. Ma. «The MLC tongue-and-groove effect on IMRT dose distributions.» En: *Physics in Medicine & Biology* 46.4 (2001), pp. 1039-60.

[4] A. Mans y col. «The NCS code of practice for the quality assurance and control for volumetric modulated arc therapy.» En: *Physics in Medicine and Biology* 61.19 (2016), pp. 7221-7235.

[5] A. Van Esch y col. «Implementing RapidArc into clinical routine: A comprehensive program from machine QA to TPS validation and patient QA». En: *Medical Physics* 38.9 (2011), p. 5146.

[6] IAEA. «Specification and Acceptance Testing of Radiotherapy Treatment Planning Systems. TECDCOC 1540». En: *Iaea Tecdoc* April (2007).

[7] IAEA. «Commissioning of Radiotherapy Treatment Planning Systems : Testing for Typical External Beam Treatment Techniques Commissioning of Radiotherapy Treatment Planning Systems : Testing for Typical External Beam Treatment Techniques. TECDOC 1583». En: *Iaea Tecdoc* January (2008).

[8] J. B. Smilowitz y col. «AAPM Medical Physics Practice Guideline 5.a.: Commissioning and QA of Treatment Planning Dose Calculations - Megavoltage Photon and Electron Beams». En: *Journal of Applied Clinical Medical Physics* 16.5 (2015), pp. 14-34.

[9] M. K. Fix, W. Volken, D. Frei, D. Frauchiger, E. J. Born y P. Manser. «Monte Carlo implementation, validation, and characterization of a 120 leaf MLC.» En: *Medical Physics* 38.10 (2011), pp. 5311-20.

[10] T. LoSasso, C. Chui y C. Ling. «Physical and dosimetric aspects of a multileaf collimation system used in the dynamic mode for implementing intensity modulated radiotherapy.» En: *Medical Physics* 25.10 (1998), pp. 1919-1927.

[11] F. Rosca y P. Zygmanski. «An EPID response calculation algorithm using spatial beam characteristics of primary, head scattered and MLC transmitted radiation.» En: *Medical Physics* 35.6 (2008), pp. 2224-2234.

[12] W. Yao y J. B. Farr. «Determining the optimal dosimetric leaf gap setting for rounded leaf-end multileaf collimator systems by simple test fields». En: *Journal of Applied Clinical Medical Physics* 16.4 (2015), p. 5321.

[13] X. Mei, I. Nygren y J. E. Villarreal-Barajas. «On the use of the MLC dosimetric leaf gap as a quality control tool for accurate dynamic IMRT delivery.» En: *Medical Physics* 38.4 (2011), pp. 2246-2255.

[14] M. S. Bhagwat, Z. Han, S. K. Ng y P. Zygmanski. «An oscillating sweeping gap test for VMAT quality assurance.» En: *Physics in Medicine and Biology* 55.17 (2010), pp. 5029-5044.

[15] D. Lewis, A. Micke, X. Yu y M. F. Chan. «An efficient protocol for radiochromic film dosimetry combining calibration and measurement in a single scan». En: *Medical Physics* 39.10 (2012), pp. 6339-6350.

[16] J. A. Vera Sanchez, C. Ruiz Morales y A. Gonzalez Lopez. «Characterization of noise and digitizer response variability in radiochromic film dosimetry. Impact on treatment verification». En: *Physica Medica* 32.9 (2016), pp. 1167-1174.

[17] Varian Medical Systems. «Eclipse Photon and Electron Reference Guide». En: April (2014), pp. 263-348.

[18] T. Torsti, L. Korhonen y V. Medical. «Using Varian Photon Beam Source Model for Dose Calculation of Small Fields». En: (2013).

[19] A. Fogliata, F. Lobefalo, G. Reggiori, A. Stravato, S. Tomatis, M. Scorsetti y L. Cozzi. «Evaluation of the dose calculation accuracy for small fields defined by jaw or MLC for AAA and Acuros XB algorithms». En: *Medical Physics* 43.10 (2016), pp. 5685-5694.

[20] H. J. Kim, S. Kim, Y. K. Park, J. I. Kim, J. M. Park y S. J. Ye. «Multileaf collimator tongue-and-groove effect on depth and off-axis doses: A comparison of treatment planning data with measurements and Monte Carlo calculations». En: *Medical Dosimetry* 40.4 (2015), pp. 271-278.

[21] J. Yang, G. Tang, P. Zhang, M. Hunt, S. B. Lim, T. LoSasso y G. Mageras. «Dose calculation for hypofractionated volumetric-modulated arc therapy: Approximating continuous arc delivery and tongue-and-groove modeling». En: *Journal of Applied Clinical Medical Physics* 17.2 (2016), pp. 3-13.

[22] F. Lorenz, A. Nalichowski, F. Rosca, J. Kung, F. Wenz y P. Zygmanski. «Spatial dependence of MLC transmission in IMRT delivery.» En: *Physics in Medicine and Biology* 52.19 (2007), pp. 5985-99.

[23] S. Chen, B. Y. Yi, X. Yang, H. Xu, K. L. Prado y W. D. D'Souza. «Optimizing the MLC model parameters for IMRT in the RayStation treatment planning system». En: *Journal of Applied Clinical Medical Physics* 16.5 (2015), pp. 322-332.

[24] L. S. Fog, J. F. B. Rasmussen, M. Aznar, F. Kjær-Kristoffersen, I. R. Vogelius, S. A. Engelholm y J. P. Bangsgaard. «A closer look at RapidArc® radiosurgery plans using very small fields.» En: *Physics in Medicine and Biology* 56.6 (2011), pp. 1853-1863.

[25] K. N. Kielar, E. Mok, A. Hsu, L. Wang y G. Luxton. «Verification of dosimetric accuracy on the TrueBeam STx: rounded leaf effect of the high definition MLC.» En: *Medical Physics* 39.10 (2012), pp. 6360-71.

[26] C. L. Ong, J. P. Cuijpers, S. Senan, B. J. Slotman y W. F. A. R. Verbakel. «Impact of the calculation resolution of AAA for small fields and RapidArc treatment plans.» En: *Medical Physics* 38.8 (2011), pp. 4471-9.

[27] I. M. Gagne, W. Ansbacher, S. Zavgorodni, C. Popescu y W. a. Beckham. «A Monte Carlo evaluation of RapidArc dose calculations for oropharynx radiotherapy.» En: *Physics in Medicine and Biology* 53.24 (2008), pp. 7167-7185.

[28] A. Fogliata, G. Nicolini, A. Clivio, E. Vanetti y L. Cozzi. «Accuracy of Acuros XB and AAA dose calculation for small fields with reference to RapidArc® stereotactic treatments Accuracy of Acuros XB and AAA dose calculation for small fields with reference to RapidArc V R stereotactic treatments». En: *Medical Physics* 38.38 (2011), pp. 31714-3666.

Capítulo 7

Conclusiones y desarrollos futuros

En dosimetría con película radiocrómica, existe una relación entre las lecturas de los diferentes canales de color, mientras que el ruido de los diferentes canales se correlaciona débilmente. Esta relación entre las lecturas se puede aproximar mediante una línea recta en rangos de dosis pequeños y permite simplificar las ecuaciones de los algoritmos multicanal. Sin embargo, cuando aumenta el rango de dosis, esta relación se vuelve más complicada. Por otro lado, el artefacto lateral del escáner aumenta la incertidumbre de esta relación entre canales.

La determinación final de la incertidumbre de las estimaciones de dosis con algoritmos multicanal mediante la ley de propagación de las incertidumbres es compleja debido a las propias ecuaciones de los algoritmos multicanal y a las relaciones estadísticas entre las respuestas de los diferentes canales. Sin embargo, este cálculo se puede llevar a cabo con técnicas Monte-Carlo y un modelo multietapa, que describe los pasos seguidos en la dosimetría con película radiocrómica. Esta metodología nos permite estudiar la incertidumbre en cada una de las etapas del proceso y la influencia del modelo del escáner empleado en la incertidumbre final de la dosimetría. Además, este enfoque de cálculo de incertidumbres puede aplicarse a algoritmos mono y multicanal.

Los modelos de escáneres EPSON 10000XL y EPSON V800 evaluados en esta tesis se comportan de igual forma con respecto al ruido. Para todas las resoluciones evaluadas y todos los canales de color, el ruido de patrón fijo se incrementa al aumentar el valor de píxel, mientras que el ruido aleatorio es

bastante constante e independiente del valor de píxel. Los algoritmos multicanal mitigan parcialmente el ruido de patrón fijo, pero no así el aleatorio. La mayor diferencia entre ambos escáneres se encuentra en la componente de ruido aleatorio, que es casi el doble para el modelo 10000XL. Así pues, el escáner V800 presenta menos ruido a altas dosis y altas resoluciones cuando se emplean algoritmos multicanal.

El ruido aleatorio presente en las imágenes de películas radiocrómicas puede mitigarse promediando varias imágenes, siempre que se empleen algoritmos de re-calibración, como el protocolo de Lewis y col., para compensar las variaciones en las lecturas. De esta forma, la eliminación del ruido conduce a mejores resultados en las verificaciones de tratamientos y permite aumentar la resolución espacial de trabajo.

En cuanto al efecto *tongue and groove*, se han presentado nuevas pruebas para su medida y se ha puesto de relevancia las discrepancias entre los cálculos de los sistemas de planificación y las medidas realizadas con cámara de ionización y película radiocrómica. Para eliminar estas discrepancias, se debe de mejorar el modelado de los colimadores multilámina en los sistemas de planificación.

Los próximos desarrollos de las líneas de investigación seguidas en esta tesis son la aplicación de las técnicas Monte-Carlo para el cálculo de la incertidumbre de los algoritmos empleados en la compensación de las variabilidades del proceso de lectura de la película radiocrómica, el estudio del efecto de diferentes algoritmos de eliminación de ruido, empleados en imagen digital, en la dosimetría con película radiocrómica y la presentación de un modelo alternativo para el efecto *tongue and groove*.

Informe

Esta tesis doctoral se presenta como compendio de las siguientes publicaciones con sus índices de calidad correspondientes:

- Vera Sánchez, J.A., Ruiz Morales, C. and González López, A.
  Monte Carlo uncertainty analysis of dose estimates in radiochromic film dosimetry with single-channel and multichannel algorithms
  Physica Medica 2018 March;47: 23-33 doi: 10.1016/j.ejmp.2018.02.006
  Factor de impacto: 1.990
  Posición: 63 de 127
  Categoría: RADIOLOGY, NUCLEAR MEDICINE & MEDICAL IMAGING

- González-López, A., Vera-Sánchez, J.A. and Ruiz-Morales, C.
  Technical Note: Statistical dependences between channels in radiochromic film readings. Implications in multichannel dosimetry
  Medical Physics 2016 May;43(5):2194. doi: 10.1118/1.4945273
  Factor de impacto: 2.617
  Posición: 37 de 127
  Categoría: RADIOLOGY, NUCLEAR MEDICINE & MEDICAL IMAGING

- González-López, A., Vera-Sánchez, J.A. and Ruiz-Morales, C.
  The incidence of the different sources of noise on the uncertainty in radiochromic film dosimetry using single channel and multichannel methods
  Physics in Medicine and Biology 2017 Nov 1;62(22):N525-N536. doi: 10.1088/1361-6560/aa8f74
  Factor de impacto: 2.742
  Posición: 34 de 127
  Categoría: RADIOLOGY, NUCLEAR MEDICINE & MEDICAL IMAGING
  Posición: 24 de 77
  Categoría: ENGINEERING, BIOMEDICAL

- Vera Sánchez, J.A., Ruiz Morales, C. and González López, A.
  Characterization of noise and digitizer response variability in radiochromic film dosimetry. Impact on treatment verification
  Physica Medica 2016 Sep;32(9):1167-74. doi: 10.1016/j.ejmp.2016.08.019
  Factor de impacto: 1.990
  Posición: 63 de 127
  Categoría: RADIOLOGY, NUCLEAR MEDICINE & MEDICAL IMAGING

- Hernández, V., Vera-Sánchez, J.A., Vieillevigne, L. and Saez, J.
  Commissioning of the tongue-and-groove modelling in treatment planning systems: From static fields to VMAT treatments
  Physics in Medicine and Biology 2017 Aug 1;62(16):6688-6707. doi: 10.1088/1361-6560/aa7b1a
  Factor de impacto: 2.742
  Posición: 34 de 127
  Categoría: RADIOLOGY, NUCLEAR MEDICINE & MEDICAL IMAGING
  Posición: 24 de 77
  Categoría: ENGINEERING, BIOMEDICAL